UNIVERSITY OF CALIFORNIA
RIVERSIDE

The Nature and Evolution of Infrared Galaxies in Clusters

A Dissertation submitted in partial satisfaction
of the requirements for the degree of

Doctor of Philosophy

in

Physics

by

Alireza Farahmandi

March 2014

Dissertation Committee:

Dr. Gillian Wilson, Chairperson
Dr. Bahram Mobasher
Dr. Gabriela Canalizo

The Dissertation of Alireza Farahmandi is approved:

Committee Chairperson

University of California, Riverside

Acknowledgments

I would like to thank to my PhD advisor, Professor Gillian Wilson, for supporting me during these past five years. She brought me to the SpARCS collaboration team that she leads. It was an honor to both work with and learn from her and other professional astronomers.

I would also like to thank Dr. Ricardo Demarco for his advice and inspiration. He helped me with Spectroscopy during my first two years at UCR and inspired my work in this field.

I thank Dr. Alessandro Rettura for his comments on my drafts, Dr. Adam Muzzin for his advice. I also thank all the astronomers in SpARCS collaboration team for motivating me and my work in this project.

I would also like to thank Professors Bahram Mobasher and Gabriela Canalizo for their help throughout my graduate school journey, from their Astronomy courses at UCR that taught me the fundamentals of Astronomy to their help on my qualifying exams and dissertation defense.

I thank all the people in the Department of Physics and Astronomy at UCR. Thank you for admitting me to this graduate program and helping me to both work with and learn from you. Also, I thank UCR Graduate Division for awarding me the prestigious five-year Graduate Division Fellowship that supported me as I completed my degree.

To my wife, Neda, who has patiently stayed by my side and supported me over the past five years of my graduate studies in the USA.

ABSTRACT OF THE DISSERTATION

The Nature and Evolution of Infrared Galaxies in Clusters

by

Alireza Farahmandi

Doctor of Philosophy, Graduate Program in Physics
University of California, Riverside, March 2014
Dr. Gillian Wilson, Chairperson

In chapter 1, I present a spectroscopic and photometric study of 105 *Spitzer*-MIPS 24 μm detected galaxies in the fields of candidate clusters from the SpARCS survey. I spectroscopically both confirm nine clusters of galaxies at $0.07 < z < 0.49$ and investigate the nature of the cluster members and field galaxies to compare their optical and infrared star formation activities. Spectroscopic classifications reveal different populations of galaxies in clusters and in the field. Most 24 μm sources are star forming galaxies which are mostly dusty starbursts. I conclude that specific star formation rates of star forming galaxies in clusters are not dependent upon clustercentric radius, but, rather, dependent upon stellar mass.

In chapter 2, I present the results of an infrared study of 250 galaxy clusters at 0.2 $< z < 1$ from the SpARCS survey. My sample spans a cluster mass range 10^{14-15} $M_{\odot}$ with an average about $2{\times}10^{14}$ $M_{\odot}$ over the redshift. Assuming a star forming galaxy template, I statistically count the number of infrared luminous galaxies in clusters

above a fixed inferred infrared luminosity of $6{\times}10^{11}$ $L_{\odot}$ per unit cluster mass and find it increases with redshift. Fitting a simple power law, I measure an evolution of $(1+z)^{5.2\pm0.5}$ within R_{200} and $(1+z)^{9.6\pm1.6}$ within R = 2Mpc from the cluster center over the redshift range of this sample. By accounting for the evolution of infrared galaxies in the field, I show that this observed evolution in clusters is due to new infalling field galaxies. Also, I estimate the total star formation rate per unit cluster mass (ΣSFR/$M_{cluster}$) and find a similar evolution of $(1+z)^{5.6\pm0.5}$ within R_{200} and $(1+z)^{8.6\pm1.5}$ within R = 2Mpc from the cluster center. The surface density of the infrared luminous galaxies seems to decrease as the distance from cluster center increases. Finally, I show that the accretion rate of infalling infrared galaxies from the field into clusters increases at higher redshifts.

In chapter 3, I investigate the position of MORPHS spectral types of galaxies at $z < 0.5$ on an IRAC color-color diagram. My sample includes 57 members from a galaxy cluster (SpARCS J104101+581741) at $z = 0.0726$ and 26 members from three other clusters at $z = 0.288$, 0.353 and 0.487 along with 24 galaxies in the field. I find that the IRAC color-color diagram isolates QSOs, poststarbursts, and passive galaxies very well but it is unable to distinguish between pure star forming and AGN galaxies because of the complexity of PAH emission lines in their spectra. At lower redshifts, I observe an evolutionary sequence of star forming galaxies from passive to starburst galaxies.

Contents

List of Figures **x**

List of Tables **xvii**

1 The Nature of *Spitzer*-MIPS 24μm Selected Galaxies in Clusters and in the Field at z <0.5 **1**

1.1 Introduction 1
1.2 Data Set and Cluster Selection 3
1.3 Data Reduction 5
1.3.1 Spectroscopy 5
1.3.2 *Spitzer* MIPS 24 μm data and Photometry 8
1.4 Data Analysis 9
1.4.1 Cluster Membership 9
1.4.2 Spectral Classifications 44
1.4.2.1 BPT Diagrams 44
1.4.2.2 MORPHS Classification 54
1.4.3 SFR(Hα) : Optical Hα Star Formation Rate 62
1.4.4 SFR(IR): IR Star Formation Rate 63
1.4.5 Stellar Mass Estimation 64
1.4.6 Spectroscopic Completeness 67
1.5 Results 69
1.5.1 Spectroscopic Confirmation of Nine Red-Sequence Selected Galaxy Clusters at $z < 0.5$ from SpARCS Survey 69
1.5.2 Spectral types of 24 μm detected galaxies in Clusters and the Field 69
1.5.3 Stacked Spectra 72
1.5.4 Star Formation Rate and Stellar Mass of 24 μm galaxies in Clusters and the Field at $z <\sim 0.5$ 75
1.5.5 The Specific Star Formation Rates (SSFR) of 24 μm Star forming Galaxies at Fixed Environment and Fixed Stellar Mass . . . 82

1.6 Discussion 85
1.6.1 AGN Fraction in Clusters and in the Field 85
1.6.2 Star Formation History 86
1.6.3 Passive Bright 24μm Galaxies 86
1.6.4 Poststarburst Galaxies in Clusters 88
1.6.5 *Spitzer* MIPS 24 μm and Spectral Classifications 89

2 The Evolution of Dusty Star Formation in Galaxy Clusters to z=1 in the SpARCS Survey 95
2.1 Introduction 95
2.2 Data 96
2.3 Analysis 100
2.4 Results 102
2.4.1 Number counts of IR galaxies in Galaxy Clusters 102
2.4.2 Comparison with the Evolution in the Field 118
2.4.3 The Evolution of total SFR per unit Cluster Mass 123
2.4.4 Radial Distribution of IR Luminous Galaxies 127

3 *Spitzer* IRAC Color-Color Diagrams: Classification of Spectroscopic Galaxies in Clusters at $z <$ 0.5 132
3.1 Galaxy Cluster SpARCS J104101+581741 132
3.2 *Spitzer* IRAC Color-Color Diagram 146
3.3 *Spitzer* IRAC Color-Color Diagram for Cluster SpARCS J104101+581741 at $z = 0.0726$ 147
3.4 *Spitzer* IRAC Color-Color Diagram for Galaxies in Clusters and in the Field at $z < 0.5$ 150
3.5 Conclusion 160

List of Figures

1.1 Members of Galaxy Cluster FLS J171059+593416 at $z = 0.125$ (See table 1.3) that were observed using the COSMIC spectrograph on the 200″ Hale Telescope at the Palomar Observatory. All the spectra are plotted in the rest-frame of the galaxies. Note that we present only the spectra we observed and the other used spectra from the literature are not presented in this figure. 12
1.2 Rest-frame spectra of the members of Clusters FLS J172408+591904 and FLS J172449+592122 at $z = 0.247$ and 0.254 (See table 1.4). . . 13
1.3 Rest-frame spectra of the members of Cluster FLS J171505+585941 at $z = 0.253$ (See table 1.5). 14
1.4 Rest-frame spectra of the members of Cluster FLS J171431+595752 at $z = 0.222$ (See table 1.6). 14
1.5 Rest-frame spectra of the members of Cluster SpARCS J104101+581741 at $z = 0.072$ (See table 1.7). 15
1.6 Rest-frame spectra of the members of Cluster SpARCS J104209+575350 at $z = 0.487$ (See table 1.8). 16
1.7 Rest-frame spectra of the members of Cluster SpARCS J022258-040715 at $z = 0.288$ (See table 1.9). 17
1.8 Rest-frame spectra of the members of Cluster SpARCS J021528-044041 at $z = 0.353$ (See table 1.10). 18
1.9 R - [3.6] vs. [3.6] color-magnitude diagram for FLS J171059+593416. The boxes are confirmed cluster members and circles are confirmed foreground/background field galaxies. Blue color is for 24 μm detected galaxies and Red color is for galaxies without 24 μm detections. Note that we plot those galaxies that have both R and [3.6] magnitudes in the catalog (table 1.3). Small background grey circles are identified photometric sources in the field of the cluster from SpARCS survey. 31
1.10 As for Figure 1.9, but for FLS J172408+591904 and FLS J172449+592122 32
1.11 As for Figure 1.9, but for FLS J171505+585941 33

1.12 As for Figure 1.9, but for FLS J171431+595752 34
1.13 z' - [3.6] vs. [3.6] color-magnitude diagram for SpARCS J104101+581741. The boxes are confirmed cluster members and circles are confirmed foreground/background field galaxies. Blue color is for 24 μm detected galaxies and Red color is for galaxies without 24 μm detections. Note that we plot those galaxies that have both R and [3.6] magnitudes in the catalog (table 1.7). Small background grey circles are identified photometric sources in the field of the cluster from SpARCS survey. . 35
1.14 As for Figure 1.13, but for SpARCS J104209+575350. 36
1.15 As for Figure 1.13, but for SpARCS J022258-040715. 37
1.16 As for Figure 1.13, but for SpARCS J021528-044041. 38
1.17 FLS J171059+593416. The boxes are confirmed cluster members and circles are foreground/background field galaxies. Blue color is for 24 μm detected galaxies and Red color is for galaxies without 24 μm detections. FOV is 5.8′ (0.8 Mpc). Note that this figure presents only the galaxies in this FOV. 39
1.18 As for Figure 1.17, but for FLS J172408+591904 and FLS J172449+592122. FOV is 12.5′ (2.9 Mpc). This system is two separate clusters, which are likely about to merge (See table 1.4 and its comments for more information). The cores are demonstrated by white circles (Left circle : FLS J172408+591904 and Right circle : FLS J172449+592122). . . 40
1.19 As for Figure 1.17, but for FLS J171505+585941. FOV is 8.4′ (2 Mpc). 41
1.20 As for Figure 1.17, but for FLS J171431+595752. FOV is 18.7′ (4 Mpc). 41
1.21 As for Figure 1.17, but for SpARCS J104101+581741. FOV is 20′ (1.6 Mpc). 42
1.22 As for Figure 1.17, but for SpARCS J104209+575350. FOV is 11′ (4 Mpc). 42
1.23 As for Figure 1.17, but for SpARCS J022258-040715. FOV is 10.5′ (2.7 Mpc) 43
1.24 As for Figure 1.17, but for SpARCS J021528-044041. FOV is 9.7′ (3 Mpc) 43
1.25 BPT diagrams for 24 μm cluster galaxies. Line ratio measurements are presented in table 1.13 and the summary of this classification is presented in table 1.15. Left diagram : The blue line is the theoretical maximum starburst limit from Kewley et al. (2001) and red line is the empirical limit from Kauffmann et al. (2003). Right diagram : The theoretical red line is from Kewley et al. (2001) and the blue line is from Kewley et al. (2006). 46
1.26 As for figure 1.25, but for 24 μm field galaxies. (See table 1.14 and table 1.15) 46
1.27 Stellar mass comparison. M_a is our estimated mass and M_k is the estimated mass from Kauffmann et al. (2003b). 66

1.28 Relative-mass-change distribution. Horizontal axis of this plot is the vertical axis of previous figure. 66
1.29 Spectroscopic completeness of cluster galaxies as a function of relative projected distance from the cluster center. 68
1.30 Positional abundance of spectral types in clusters. 71
1.31 Normalized and completeness corrected stacked spectra of 24 μm star forming galaxies in clusters (green) and in the field (black) at $0.1 < z < 0.3$ (See table 1.20 and table 1.21). Each stacked spectrum is produced from the spectra of 22 galaxies. Stacked cluster and field spectra are very similar to each other. (See Section 1.4.6 and 1.5.3) 74
1.32 IR SFR versus Stellar Mass for 24 μm star forming galaxies. The green boxes are cluster galaxies and the black boxes are field galaxies. The cross in lower-right presents the maximum uncertainties in our estimations. 76
1.33 Specific SFR(IR) versus Stellar Mass for 24 μm star forming galaxies. The green boxes are cluster galaxies and the black boxes are field galaxies. The solid line is the empirical relation from Salim et al. (2007) for comparison. The cross in lower-left presents the maximum uncertainties in the estimations. 77
1.34 Observed SFR(Hα) versus redshift of active star forming galaxies. Observed SFR(Hα) was not corrected for extinction. AGNs, Post-starburst and Passive galaxies were excluded. Cluster galaxies are shown by green triangles and Field galaxies by black boxes. Background circles are data from Marleau et al. (2007) for comparison (See Section 1.5.4). 78
1.35 L_{IR} versus redshift of active star forming galaxies. AGNs, Post-starburst and Passive galaxies were excluded. Cluster galaxies are shown by green triangles and Field galaxies by black boxes. Background circles are data from Kartaltepe et al. (2010) for comparison (See Section 1.5.4). 80
1.36 IR SFR versus Observed Hα SFR of those active star forming galaxies that both SFRs were measurable. Observed SFR(Hα) was not corrected for extinction. AGNs, Post-starburst and Passive galaxies were excluded. Cluster galaxies are shown by green diamonds and field galaxies by black boxes. Background grey circles are data from Marleau et al. (2007) for comparison. Solid line shows no extinction (IR SFR = observed Hα SFR). 81
1.37 Logarithm of the mean SSFR of star forming galaxies in clusters as a function of clustercentric radius for galaxies with different stellar masses. The SSFR is nearly independent of environment at all stellar masses. The error bars represent the standard error in mean SSFR. . 83

1.38 Logarithm of the mean SSFR of star forming galaxies in clusters as a function of stellar mass for galaxies in different environments. The SSFR is correlated with stellar mass in all environments. The error bars represent the standard error in mean SSFR. 84
1.39 SDSS optical images of the bright passive 24 μm galaxies in clusters. Each galaxy is labled with ID, 24 μm flux and spectral type. 87

2.1 Estimated cluster mass versus redshift of our sample. 98
2.2 Filled symbols: differential completeness from simulations for EN1, EN2, and XMM-LSS fields. The curves for the other three fields were obtained by shifting the EN1 curve. Open squares: differential reliability defined as the fraction of SWIRE sources found in the deeper GTO data in CDFS. This plot is from Shupe et al. (2008). 99
2.3 The expected observed 24 μm flux of a template galaxy with L_{IR} = $6{\times}10^{11}L_{\odot}$ computed from the combined models of Chary & Elbaz (2001) and Dale & Helou (2002). Our 24 μm source catalog is deep enough to reach at this luminosity at $z = 1$ with 80% completeness (350 μJy). 101
2.4 The total number of galaxies with $L_{IR} > 6{\times}10^{11}L_{\odot}$ in excess of the average background counts, within the fixed radii (0.5, 1.0, 1.5 and 2.0 Mpc) of the cluster centers in EN1 field. The solid lines represent the standard deviation of the average background counts ($\pm\sigma$). Since the number of random apertures is 1250 < n < 2750 and the random error of the background average is calculated from $\sigma/\sqrt{n}$, error bars are small and can not be displayed on this diagram. 104
2.5 Same as figure 2.4 but for CDFS field. 105
2.6 Same as figure 2.4 but for EN2 field. 106
2.7 Same as figure 2.4 but for ES1 field. 107
2.8 Same as figure 2.4 but for Lockman field. 108
2.9 The mean number of galaxies with $L_{IR} > 6{\times}10^{11}L_{\odot}$ in excess of the average background counts, within the fixed radii (0.5, 1.0, 1.5 and 2.0 Mpc) of the cluster center. We averaged figure 2.4 to 2.8 in four redshift bins and the uncertainties correspond to the standard errors in the mean. 109
2.10 The total number of galaxies with $L_{IR} > 6{\times}10^{11}L_{\odot}$ in excess of the average background counts, within R_{200} of the cluster center and divided by total mass of the cluster in EN1 field. The continuous solid lines represent the standard deviation of the average background counts divided by total mass for each cluster ($\pm\sigma/M_{200}$). For each cluster, $\pm\sigma/M_{200}$ is on the solid lines. 110
2.11 same as figure 2.10 but for CDFS field. 111
2.12 same as figure 2.10 but for EN2 field. 112

2.13 same as figure 2.10 but for Lockman field. 113
2.14 same as figure 2.10 but for ES1 field. 114
2.15 same as figure 2.4 but for all the fields within R_{200} of the cluster centers. 115
2.16 The number of galaxies with $L_{IR} > 6{\times}10^{11}L_{\odot}$ in excess of the average background counts, within 2 Mpc of the cluster center, normalized by cluster halo mass M_{200} and averaged in four redshift bins. Y error bars correspond to the standard errors in the mean and X error bars only present the redshift ranges of the bins. The dashed line represents the best power-law fit in the form of $N_{>}$/M $\propto (1+z)^n$ with n = 9.6 ± 1.6 . 116
2.17 Same as figure 2.16 but within R_{200} of the cluster center. The black dashed line represents the best power-law fit in the form of $N_{>}$/M $\propto$ $(1+z)^n$ with n = 5.2 ± 0.5, the green dotted line is the best fit of Webb et al. (2013) with n = 5.1 and normalized at z = 0.4 to our fit. Note Y error bars correspond to the standard errors in the mean and X error bars only present the redshift ranges of the bins. 117
2.18 Solid line : The expected observed 24 μm flux of a template galaxy with $L_{IR} = 6{\times}10^{11}L_{\odot}$ computed from the combined models of Chary & Elbaz (2001) and Dale & Helou (2002). Our 24 μm source catalog is deep enough to reach at this luminosity at $z = 1$ with 80% completeness (350 μJy) . Dashed line : Parametrized flux depth of $L_{IR} = 6{\times}10^{11}L_{\odot}$ at $z = 1$ which follows the evolution of $L^{\star}_{IR}$ of the field at $z < 1$. This parametrized flux depth is only used in Section 2.4.2. 120
2.19 Similar to figure 2.16, but with considering the evolution of $L^{\star}_{IR}$ in the field. We count the number of IR luminous galaxies above the parametrized flux depth in figure 2.18 and within R = 2 Mpc of the cluster center. The dotted line represents the best power-law fit in the form of $N_{>}$/M $\propto (1+z)^n$ with n = 0.16 ± 0.28 . Note that X error bars only present the redshift ranges of the bins and Y error bars correspond to the standard errors in the mean. 121
2.20 Same as figure 2.19 but within R_{200} of the cluster center. The dashed line represents the best power-law fit in the form of $N_{>}$/M $\propto (1+z)^n$ with n = -0.6 ± 1.0 . Note that X error bars only present the redshift ranges of the bins and Y error bars correspond to the standard errors in the mean. 122
2.21 Averaged integrated total star formation rate per unit cluster mass ΣSFR/M_{200}, within R = 2 Mpc from cluster center in four redshift bins. The solid line is the best power-law fit in the form of ΣSFR/M_{200} $\propto (1+z)^n$ with n = 8.6 ± 1.5 . Note that X error bars only present the redshift ranges of the bins and Y error bars correspond to the standard errors in the mean. 124

2.22 Same as figure 2.21 but within R_{200} from cluster center. The solid line is our best power-law fit in the form of $\Sigma\text{SFR}/M_{200} \propto (1+z)^n$ with n = 5.6 ± 0.5 . The green dashed line is Webb et al. (2013) result with n = 5.4 and since it is very close its scaled fit to our data we just use the actual result here. The red dashed line is from Popesso et al. (2012) and the red line is its scaled fit to our data. Note that X error bars only present the redshift ranges of the bins and Y error bars correspond to the standard errors in the mean. 125
2.23 The surface density of the IR luminous galaxies in cluster-centric annuli. Y error bars correspond to the standard errors in the mean. . . 128

3.1 The color-magnitude diagram for SpARCS J104101+581741. The boxes are the MIPS 24 μm detected galaxies and circles are the undetected galaxies. Passive galaxies are in red, active star forming galaxies are in blue, post-starbursts are in yellow and AGNs are in black. 140
3.2 The histogram of spectroscopic redshifts in SpARCS J104101+581741. The redshift bins were optimized by Scott's normal rule and the best gaussian fit is shown by red solid line. 141
3.3 The velocity of each member relative to the mean cluster velocity as a function of clustercentric distance 142
3.4 The position of cluster members in SpARCS J104101+581741. The BCG is at the center and green solid lines represent 1, 2 and 3 Mpc distance from the center. The boxes are the MIPS 24 μm detected galaxies and circles are the undetected galaxies. Passive galaxies are in red, active star forming galaxies are in blue, post-starbursts are in yellow and AGNs are in black. 1 Mpc at cluster's redshift is about 12 arc minutes. 143
3.5 The BCG of SpARCS J104101+581741 at $z = 0.0726$ is the center of this cluster. This image from SDSS DR10 present all photometric detected objects around this galaxy. 144
3.6 The BCG of SpARCS J104101+581741 in SDSS r, i *and* g bands. . . 145
3.7 *Spitzer* IRAC Color-Color Diagram for Cluster SpARCS J104101+581741 at $z = 0.0726$. The boxes are the MIPS 24 μm detected galaxies and circles are the undetected galaxies. Passive galaxies are in red, active star forming galaxies are in blue, post-starbursts are in yellow and AGNs are in black. According to Sajina et al. (2005), the upper-left section corresponds to low redshift ($z < 0.3$) PAH dominated galaxies, the upper-right is AGN section (continuum dominated), lower-right the section for stellar and PAH dominated galaxies at high redshifts ($z > 1.6$) and lower-left is the section for stellar and PAH dominated galaxies at low redshifts. 149

3.8 Same as figure 7 but for active star forming galaxies. Starbursts (*e(b)*) are in green and Quiescent (normal) star forming galaxies (*e(c)*) are in orange. Note that in MORPHS classification normal star forming galaxies are labeled as quiescent star forming galaxies (Dressler et al., 1999) (See Section 1.4.2.2 and Table 1.16). 151
3.9 A zoom-in of the lower-left region of Figure 7. 152
3.10 *Spitzer* IRAC Color-Color Diagram for cluster members. 158
3.11 Same as figure 3.10 but for field galaxies. 159
3.12 The positions of the MORPHS spectral types on IRAC color-color diagram at $z < 0.5$. The green region is the sequence of star forming galaxies at very low redshifts. 161

List of Tables

1.1 Confirmed Clusters of Galaxies and Their Properties 6
1.2 Masks and Exposure Times 7
1.3 Photometric, Redshift and Spectral Type Catalog for Cluster FLS J171059+593416 19
1.4 As for Table 3, but for FLS J172408+591904 and FLS J172449+592122 21
1.5 As for Table 3, but for FLS J171505+585941 23
1.6 As for Table 3, but for FLS J171431+595752 24
1.7 As for Table 3, but for SpARCS J104101+581741 26
1.8 As for Table 3, but for SpARCS J104209+575350 27
1.9 As for Table 3, but for SpARCS J022258-040715 28
1.10 As for Table 3, but for SpARCS J021528-044041 29
1.11 As for Table 3, but for other Field Galaxies 30
1.12 Line Strength Index Definitions 47
1.13 Spectroscopic Catalog of 24 μm Cluster Galaxies for BPT Classification 48
1.14 As for table 1.13, but for 24 μm Field Galaxies 50
1.15 Summary of BPT Classification of the 24 μm Galaxies in Clusters and in the Field 53
1.16 Adopted MORPHS Spectral Classification 55
1.17 Spectroscopic Catalog of 24 μm Cluster Galaxies for MORPHS Classification 57
1.18 As for Table 1.17, but for 24 μm Field Galaxies 59
1.19 Summary of MORPHS Classification of the 24 μm Galaxies in Clusters and in the Field 61
1.20 Stacked Spectra of 24 μm Star forming Galaxies - BPT Classification 73
1.21 Stacked Spectra of 24 μm Star forming Galaxies - MORPHS Classification 74

3.1 SpARCS J104101+581741 properties 134
3.2 Photometric, Redshift and Spectral Type Catalog for Cluster SpARCS J104101+581741 135

3.3 Photometric, Redshift and Spectral Type Catalog for the members of SpARCS J022258-040715, SpARCS J021528-044041 and SpARCS J104209+575350 153
3.4 Photometric, Redshift and Spectral Type Catalog for the field galaxies. 156

Chapter 1

The Nature of *Spitzer*-MIPS 24μm Selected Galaxies in Clusters and in the Field at z <0.5

1.1 Introduction

The well known discovery by Butcher & Oemler (1978), which revealed the rapid evolution of star formation activity of galaxies in rich clusters within the last five billion years ($z < 0.5$), has changed our view of galaxy evolution. Another discovery by Dressler & Gunn (1983) showed that most of the star forming galaxies in clusters are starbursts, based on their optical spectra. Over three decades of observational work after these two pioneer discoveries, the nature of the processes in this recent evolution of galaxies in clusters is still not clearly understood. (Oemler et al., 2009)

In order to understand the mechanisms and characterize the evolution of these galaxies, Star Formation Rate (SFR) is one of the key parameters that needs to be measured. The global star formation history in the field shows that SFR density based on the rest-frame UV and optical studies has decreased by a factor of about 10 between $z \sim 1$ and $z = 0$ (Bouwens et al., 2008; Reddy et al., 2008; Watson et al., 2009), and has a precipitous decline so that our epoch becomes the beginning of the end of star formation in galaxies (Dressler et al., 2009a). The rest-frame UV and optical tracers suffer from the effects of dust extinction but IR re-emission of dust can be used as a reliable star formation tracer to penetrate the dusty universe and reveal the strong activities buried under dust which were previously hidden. *Spitzer* MIPS $24\mu m$ data provide a great opportunity to account for the amount of dust-obscured star formation, which still has uncertainties.

Star formation activities in environments (Clusters and Groups) are generally less than in the field (Vulcani et al., 2010). The star formation rates have been studied in multiple cluster surveys such as CNOC (Balogh et al., 1998), MORPHS (Dressler et al., 1999), *Spitzer*/MIPS GTO team (Bai et al., 2007), EDisCS (Finn et al., 2010) and SMIRCS (Saintonge et al., 2008). Among the projects that study clusters at $z < 0.4$ with *Spitzer* MIPS $24\mu m$ data, the SMIRCS project has the highest number of clusters, with only four, including the Coma cluster. In this paper, based on spectroscopy of $24\mu m$ detected galaxies, we present the spectroscopic confirmation of nine clusters at $0.07 < z < 0.49$, investigate the nature of the cluster members and field galaxies, and compare their dusty star formation activities.

This paper is organized as follows: We describe our Data Sets and Cluster Selection in Section 1.2 and Data Reduction in Section 1.3. We then describe Data Analysis of the galaxies in Section 1.4. Results are presented in Section 1.5 and Discussion in Section 1.6.

We adopt a ΛCDM cosmology, assuming $\Omega_m = 0.3$, $\Omega_\Lambda = 0.7$, and $H_0 = 70$ km s^{-1} Mpc^{-1}.

1.2 Data Set and Cluster Selection

Galaxy clusters were identified in the Spitzer First Look survey (FLS) and SpARCS survey, using an algorithm described in detail in Muzzin et al. (2008, 2012) and Lacy et al. (2005). For cluster detection in both the FLS and SpARCS surveys, we used an infrared adaptation of the cluster red-sequence (CRS) technique (Gladders & Yee , 2000, 2005). This algorithm maps the density of galaxies in a survey within narrow color slices, giving greater weight to brighter galaxies, and flagging the highest overdensities as candidate clusters. The one important difference between FLS and SpARCS survey, is that in FLS a R-[3.6] color is used to detect clusters but in SpARCS a z'-[3.6] color is used. The deeper IRAC data in SWIRE (4×30s frames), compared to the FLS (5×12s frames), combined with the z'-[3.6] color choice, allow SpARCS to detect clusters to higher redshift than was possible with the FLS data set.

In Spitzer FLS survey and SpARCS survey fields we found a statistically significant excess of 24 μm counts in the neighborhood of candidate galaxy clusters. The 24 μm excess could not be caused by chance foreground/background interlopers and it may be related to the dust-obscured starburst galaxies in the clusters.

We acquired observing time to do multi-object spectroscopy of red-sequence galaxies in the field of nine candidate clusters at $0.1 < z_{ph} < 0.6$. These galaxies were selected brighter than R = 21.5 in FLS and $z' = 20$ in SpARCS. The goal was to first obtain spectroscopic redshifts and establish that they are indeed at the cluster redshift. Our second goal was to classify the 24 μm sources by galaxy type (post-starburst, early-type, late-type, ULIRG or AGN) and understand the mechanism by which spiral galaxies evolve into the elliptical/S0 systems that dominate the cluster population at current epoch.

Multi-object spectroscopy of red-sequence galaxies was performed in the fields of five candidate clusters in FLS, two candidate clusters in XMM-LSS field of SpARCS, and two candidate clusters in Lockman field of SpARCS on 26, 28, 29, 30 May 2006, 17, 18, 19, 20 Nov 2006, and 15, 16, 17 June 2007, using the COSMIC Spectrograph on the 200″ Hale Telescope at the Palomar Observatory. Conditions were good on all nights and seeing ranged between 0.9″ - 1.3″. The observations were made with the 300 l/mm grating blazed at 5500Å with 1″ wide slits giving a spectral resolution of 8Å (~ 450 km s^{-1}). With this grating setting the spectra cover the wavelength range 3600 - 8900Å which for most of the cluster galaxies permits the measurement of all major spectral features between [O II] 3727Å through [S II] 6731Å .

COSMIC has a field-of-view (FOV) of $11'' \times 4''$ usable for spectroscopy. Three or two masks per cluster were observed. In the case of three masks, one centered on the cluster and two offset $2.5'$ north and south of the cluster center, respectively. The area covered by spectroscopy around the cluster center is slightly larger than the estimated area of R_{200} for the clusters and permits spectroscopic confirmation of virialized cluster galaxies, as well as galaxies that are likely to be infalling into the cluster. Slits were placed preferentially on galaxies detected at 24 μm; however, a few slits were reserved for red-sequence cluster galaxies so that the redshift of the clusters could also be confirmed. Including the 5 - 7 stars required for mask alignment, 18 - 25 slits were positioned on each mask.

The list of the confirmed clusters and their masks in this chapter are presented in table 1.1 and table 1.2 .

1.3 Data Reduction

1.3.1 Spectroscopy

To reduce the Palomar data, we used the adapted custom software by Ricardo Demarco (Demarco et al., 2010) to reduce Keck-LRIS data. Overscan and bias corrections were applied to the calibration (bias, flats and lamp arcs) and to the science

Table 1.1. Confirmed Clusters of Galaxies and Their Properties

Cluster	ID	R.A. (J2000)	Dec. (J2000)	z_{cl}	N_{mem}	N_{24}	σ_v (km s^{-1})	R_{200}	M_{200}
FLS J171059+593416	F1	17:10:59.80	59:34:16.40	0.125±0.001	7	3	696 ± 284	1.6 ± 0.7	$5.4_{-4.3}{}^{+9.7}$
FLS J172408+591904	F2-1	17:24:07.82	59:19:04.30	0.247±0.001	6	4	612 ± 274	1.3 ± 0.6	$3.5_{-3}{}^{+7}$
FLS J172449+592122	F2-2	17:24:49.00	59:21:22.90	0.254±0.001	7	7	788 ± 322	1.7 ± 0.7	$7.4_{-5.9}{}^{+13.3}$
FLS J171505+585941	F3	17:15:05.20	58:59:41.40	0.253±0.001	5	2	364 ± 182	0.8 ± 0.4	$0.73_{-0.64}{}^{+2.44}$
FLS J171431+595752	F5	17:14:31.10	59:57:52.20	0.222±0.002	8	8	1238 ± 468	2.7 ± 1.0	$29_{-22}{}^{+47}$
SpARCS J104101+581741	L1	10:41:01.03	58:17:41.90	0.072±0.001	9	8	538 ± 220	1.3 ± 0.5	$2.6_{-2.0}{}^{+4.6}$
SpARCS J104209+575350	L2	10:42:09.60	57:53:50.86	0.487±0.002	6	2	1107 ± 495	2.1 ± 0.9	$18_{-15}{}^{+36}$
SpARCS J022258-040715	X1	02:22:58.58	-04:07:15.10	0.288±0.001	9	5	396 ± 140	0.8 ± 0.3	$0.92_{-0.67}{}^{+1.36}$
SpARCS J021528-044041	X2	02:15:28.22	-04:40:41.23	0.353±0.001	11	5	847 ± 268	1.7 ± 0.6	$8.7_{-5.9}{}^{+11.1}$

Note. — . N_{mem} is the total number of spectroscopic members and N_{24} is the total numbers of spectroscopic members which were identified as 24 μm sources. z_{cl} and σ_v are the mean cluster redshift and rest-frame cluster velocity dispersion. z_{cl}, σ_v, R_{200} (in units of Mpc) and M_{200} (in units of $\times 10^{14}$ $M_\odot$) are calculated using spectroscopics cluster members only.

Table 1.2. Masks and Exposure Times

Cluster	Field	Mask #	Observing Date	Exposure (s)	N_{exp}	Total (s)
FLS J171059+593416	FLS	1	05-29-2006	900	4	3600
		2	05-30-2006	900	4	3600
		3	06-15-2007	900	4	3600
FLS J172449+592122	FLS	1	05-30-2006	1200	7	8400
		2	05-30-2006	1200	7	8400
		3	06-15-2007	1200	6	7200
		4	06-17-2007	1200	4	4800
FLS J171505+585941	FLS	1	05-29-2006	1200	6	7200
		2	05-29-2006	1200	7	8400
		3	06-15-2007	1200	4	4800
FLS J171431+595752	FLS	1	06-16-2007	1200	5	6000
		2	06-16-2007	1200	5	6000
		3	06-16-2007	1200	5	6000
SpARCS J104101+581741	Lockman	1	11-17-2006	1800	4	7200
		2	11-18-2006	1800	4	7200
SpARCS J104209+575350	Lockman	1	11-19-2006	1800	5	9000
		2	11-20-2006	1800	5	9000
SpARCS J022258-040715	XMM-LSS	1	11-20-2006	1800	5	9000
		2	11-20-2006	1800	5	9000
SpARCS J021528-044041	XMM-LSS	1	11-19-2006	1800	5	9000
		2	11-19-2006	1800	5	9000

Note. — Masks, Observing dates, Exposure times, Number of exposure times and Total exposure times of the Masks.

(clusters and standard stars) frames using IRAF *imcombine, zerocombine, ccdproc.* After these corrections were applied, the data were then corrected for geometric distortions across the dispersion axis, and then separated into individual slitlets and reduced using standard *long-slit* techniques. Each individual slitlet was processed using an algorithm similar to that implemented in *bogus* (Developed by D. Stern, A.J. Bunker and S.A. Stanford). The flatfield slitlets were normalized and applied to the corresponding science slitlets. The individual two-dimensional spectra were then background-subtracted to produce a final two-dimensional spectrum. The one-dimensional spectrum of the source (or sources) in each slitlet was then extracted using standard IRAF tasks (Demarco et al., 2010).

Wavelength calibration for the May 2006 data was performed using bright sky lines and the Nov 2006 and June 2007 data were performed using comparison spectra of a FeAr arc lamp. Finally, a relative flux calibration was performed, using a sensitivity function spanning the range 3600-8900 Å , which was obtained from long-slit observations of the standard star Feige F110.

1.3.2 *Spitzer* MIPS 24 μm data and Photometry

We used *Spitzer* MIPS 24 μm reduced mosaics of Extragalactic FLS (First Look Survey) (Fadda et al., 2006) and XMM-LSS and Lockman fields of SWIRE (The *Spitzer* Wide-area Infrared Extragalactic Survey), which are publicly available at Data Archive of *Spitzer* Science Center. We extracted the 24 μm sources using SExtractor

(Bertin & Arnouts , 1996). The pixel size of FLS and SWIRE fields are 1.2707″ and 1.2″, respectively, and for MIPS FWHM, which is 5.9″. We measured flux in circular apertures of radius 12.71″ and 11.4″ (10 pixel and 9.5 pixel), respectively. For aperture correction we applied the corresponding parameters from MIPS Instrument Handbook and Fadda et al. (2006). The measured flux density in MJy/Str converted to Jy/arcsec^2 and then to Jy.

1.4 Data Analysis

1.4.1 Cluster Membership

A redshift solution was sought for each object by cross-correlating (Tonry & Davis , 1979) each of the spectra with 11 observed galaxy templates using the task *XCSAO* in the IRAF RVSAO package (Kurtz et al., 1992). If a redshift could be obtained for a spectrum, it was assigned a quality flag, "Q", with one of two possible values: 1 (= Low-confidence) or 2 (= High-confidence). High-confidence redshifts are unambiguously determined by two or more clear features in the continuum or in absorption, or by obvious emission lines such as Hα, [O III], Hβ, [O II], ... Low-confidence redshifts are determined based on ambiguous identification of a few spectral features, often in low signal-to-noise (S/ N) spectra.

To determine cluster membership, we compared the high-confidence redshifts of the galaxies in each candidate cluster. For these redshifts, if they are very close to each other (less than 3σ), then we assign them as members of the cluster. Also, we searched many publicly available catalogs in the fields of these clusters to find new members with confirmed spectroscopic redshifts. Based on this, we could spectroscopically confirm nine clusters with enough members (n ≥ 5) ($z = 0.125$, 0.247, 0.254, 0.253, 0.222 in FLS , $z = 0.288$, 0.353 in SWIRE-XMM and $z = 0.072$, 0.487 in SWIRE-Lockman). There are 68 cluster galaxies in total at $0.07 < z < 0.49$ and of these only 44 members are 24 μm sources. The list of confirmed galaxy clusters is presented in table 1.1. Spectra of the identified cluster galaxies are shown in Figure 1.1 through Figure 1.8 and the catalogs of the cluster members are presented in table 1.3 through table 1.11. Color-Magnitude diagrams are presented in Figure 1.9 through Figure 1.16 and three-color composite images of the clusters are presented in Figure 1.17 through Figure 1.24.

We calculated the line-of-sight rest-frame velocity dispersion, σ_v, directly from the vector of spectroscopic redshift measurements, $\overrightarrow{z}$, as

$$\sigma_v = \frac{\sigma_z(\overrightarrow{z}) \times c}{1 + z_{cl}} \tag{1.1}$$

where c is the speed of light, and $\sigma_z(\overrightarrow{z})$ is the estimated dispersion of the measured redshifts with respect to the center of the distribution, z_{cl} .

In the spherical collapse model $R_{200}(z)$, the radius at which the mean interior density is 200 times the critical density, ρ_{cr}, can be calculated from line-of-sight rest-frame velocity dispersion as:

$$R_{200} = \frac{\sqrt{3}\sigma_v}{10H(z)} \tag{1.2}$$

where H(z) $= H_0\sqrt{\Omega_m(1+z)^3+\Omega_k(1+z)^2+\Omega_\Lambda}$, is the Hubble parameter at redshift z. Note that Ω_m is the matter density today, Ω_k is the spatial curvature density today and Ω_Λ is the cosmological constant.

Also $M_{200}(z)$, the mass contained within $R_{200}(z)$, was calculated from:

$$M_{200} = \frac{3{\sigma_v}^2 R_{200}}{G} \tag{1.3}$$

The calculated results for these nine confirmed clusters are presented in table 1.1.

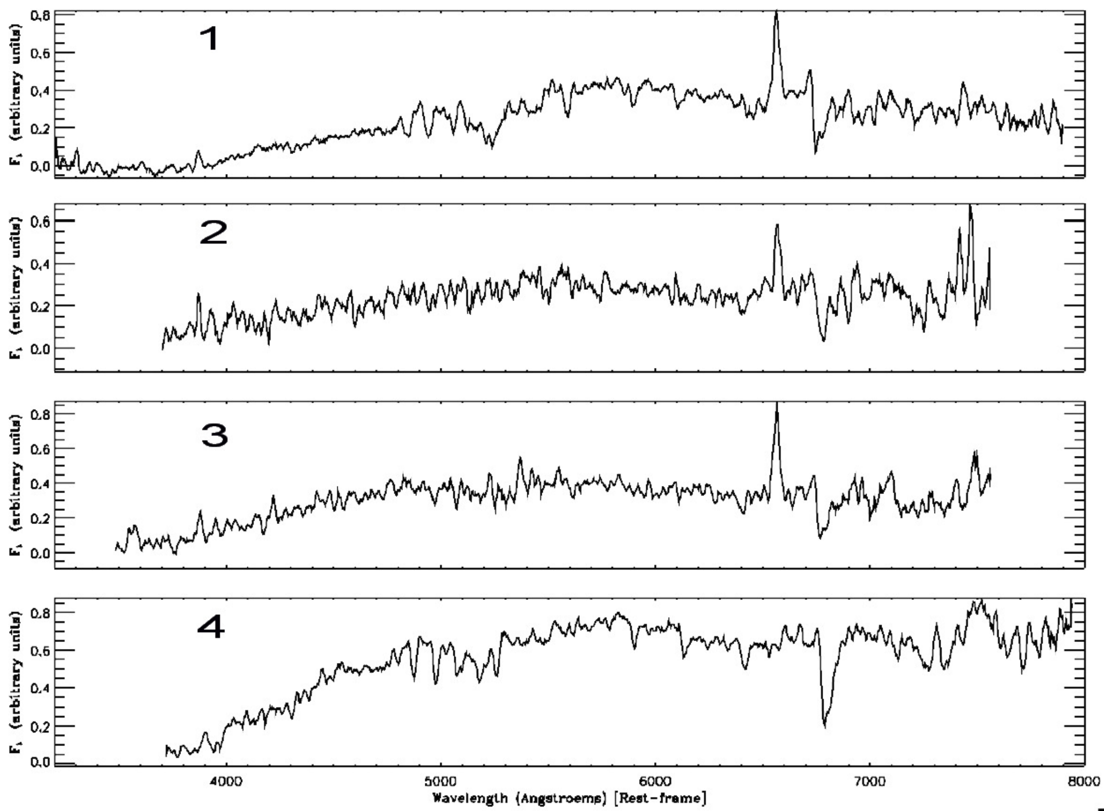

Figure 1.1 Members of Galaxy Cluster FLS J171059+593416 at $z = 0.125$ (See table 1.3) that were observed using the COSMIC spectrograph on the 200″ Hale Telescope at the Palomar Observatory. All the spectra are plotted in the rest-frame of the galaxies. Note that we present only the spectra we observed and the other used spectra from the literature are not presented in this figure.

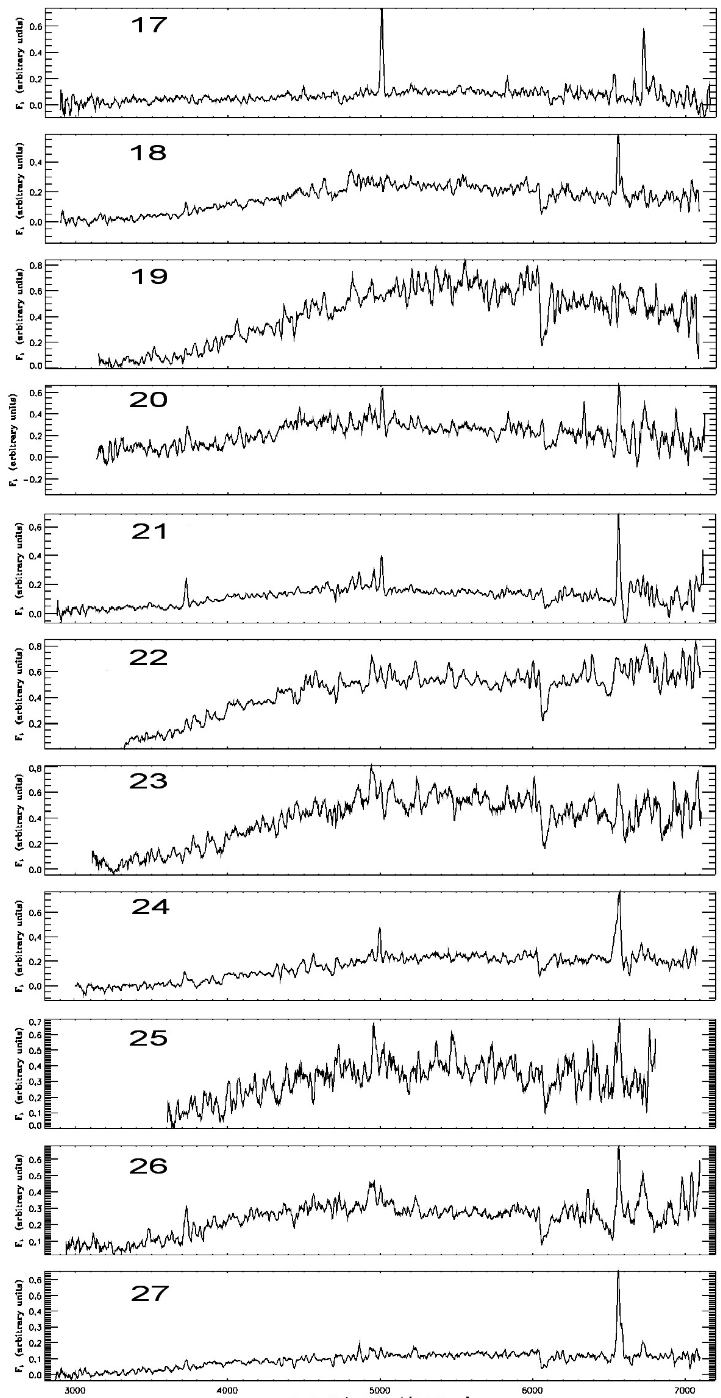

Figure 1.2 Rest-frame spectra of the members of Clusters FLS J172408+591904 and FLS J172449+592122 at $z = 0.247$ and 0.254 (See table 1.4).

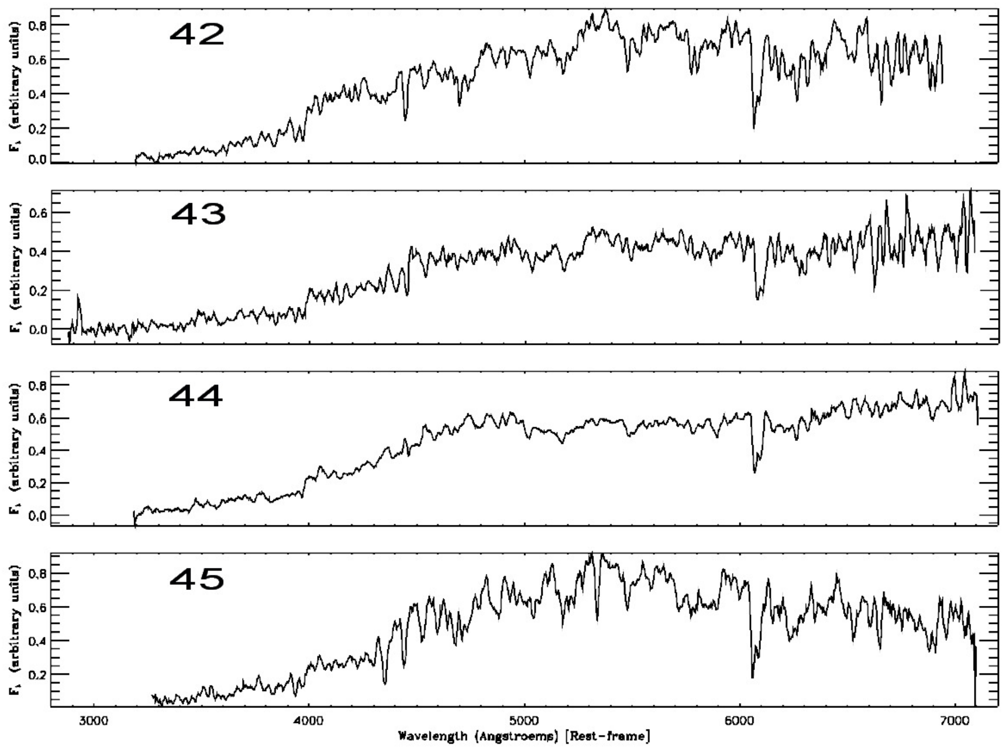

Figure 1.3 Rest-frame spectra of the members of Cluster FLS J171505+585941 at z = 0.253 (See table 1.5).

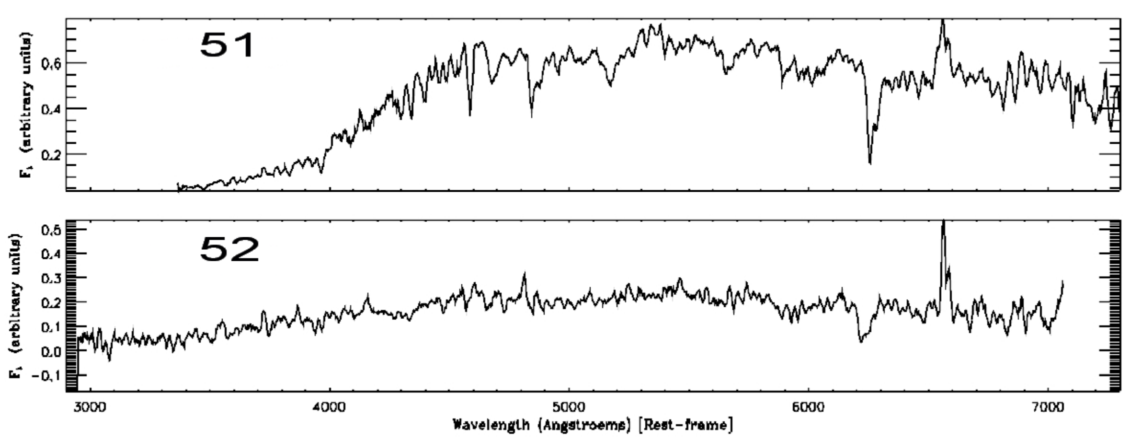

Figure 1.4 Rest-frame spectra of the members of Cluster FLS J171431+595752 at z = 0.222 (See table 1.6).

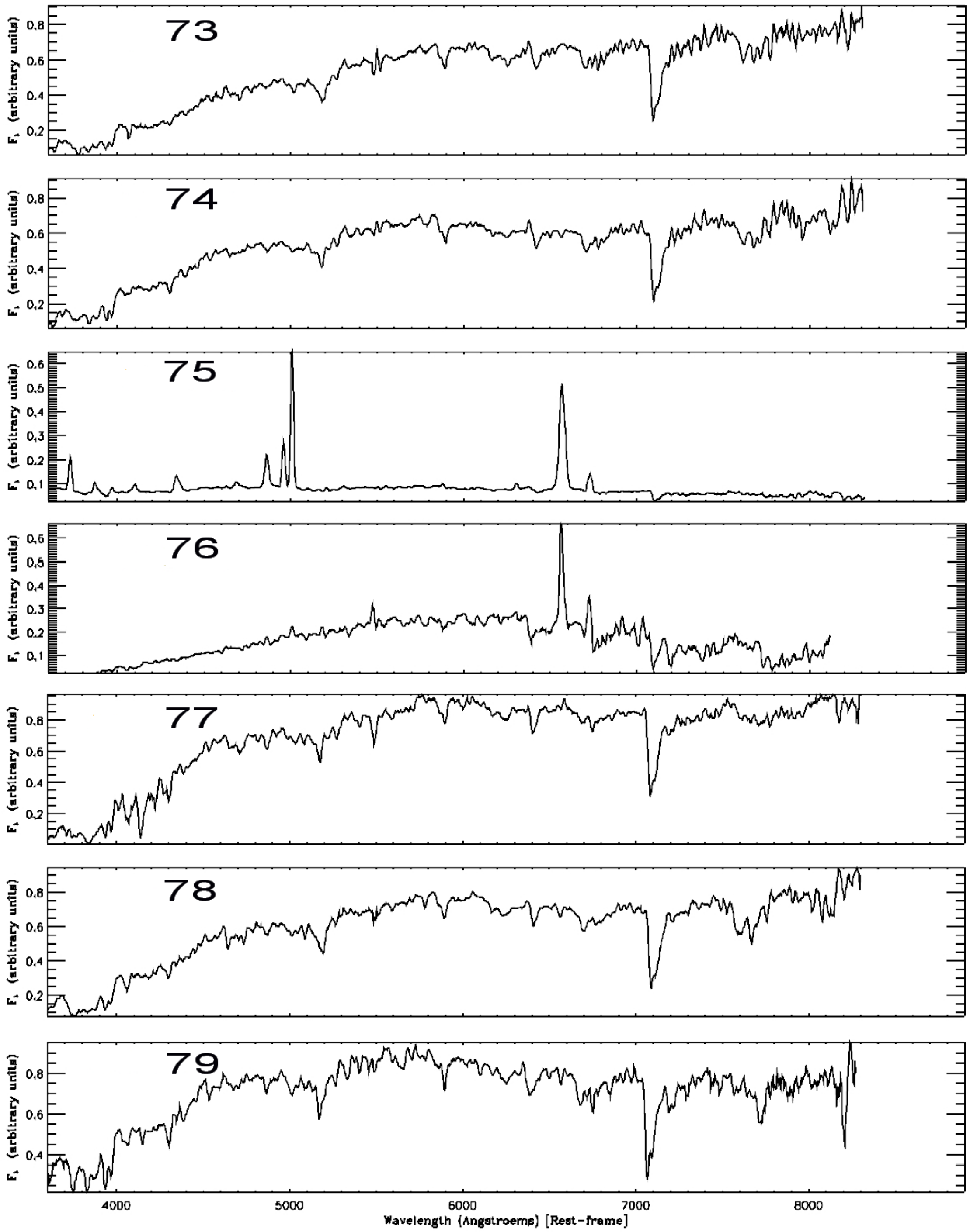

Figure 1.5 Rest-frame spectra of the members of Cluster SpARCS J104101+581741 at $z = 0.072$ (See table 1.7).

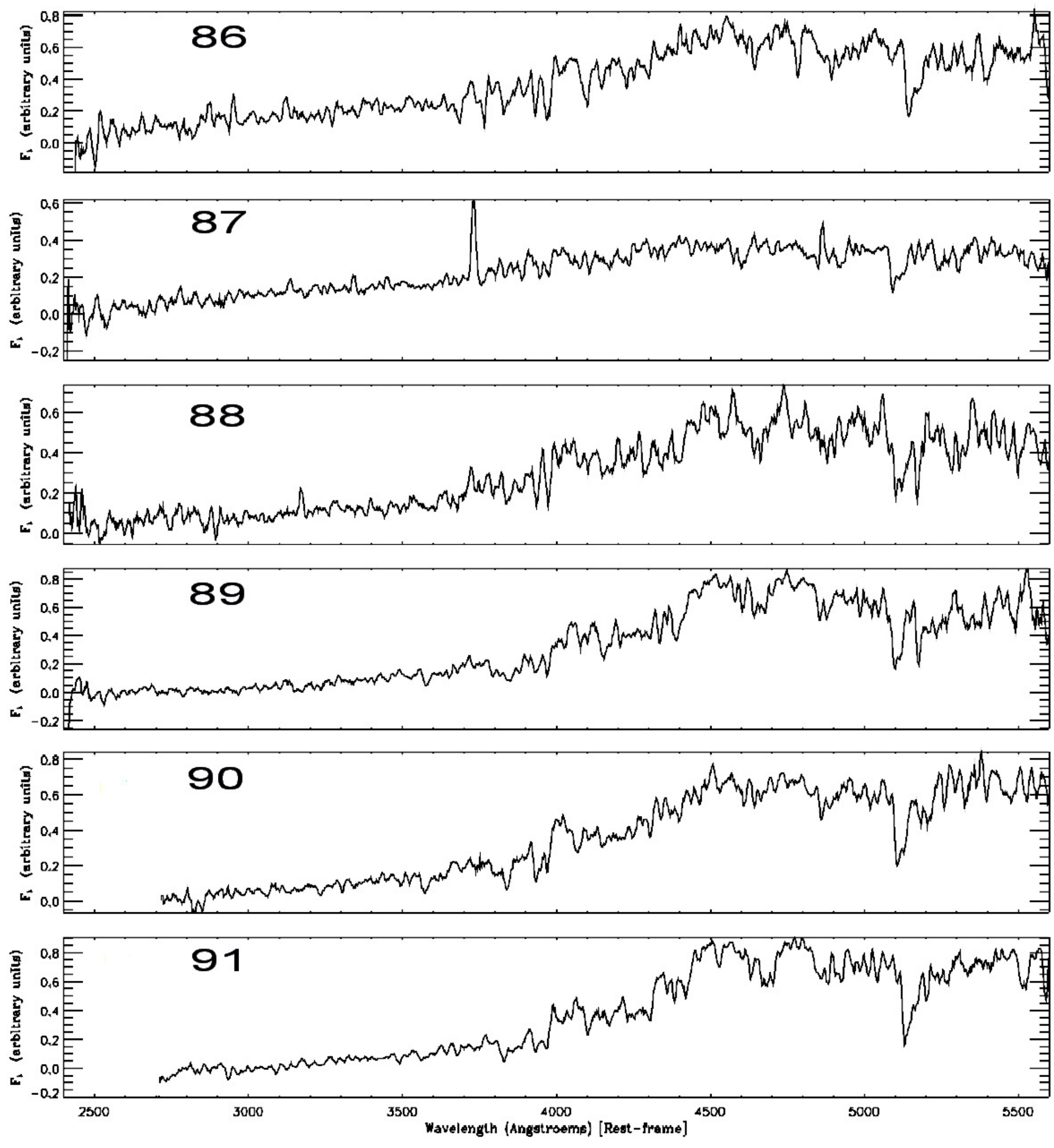

Figure 1.6 Rest-frame spectra of the members of Cluster SpARCS J104209+575350 at $z = 0.487$ (See table 1.8).

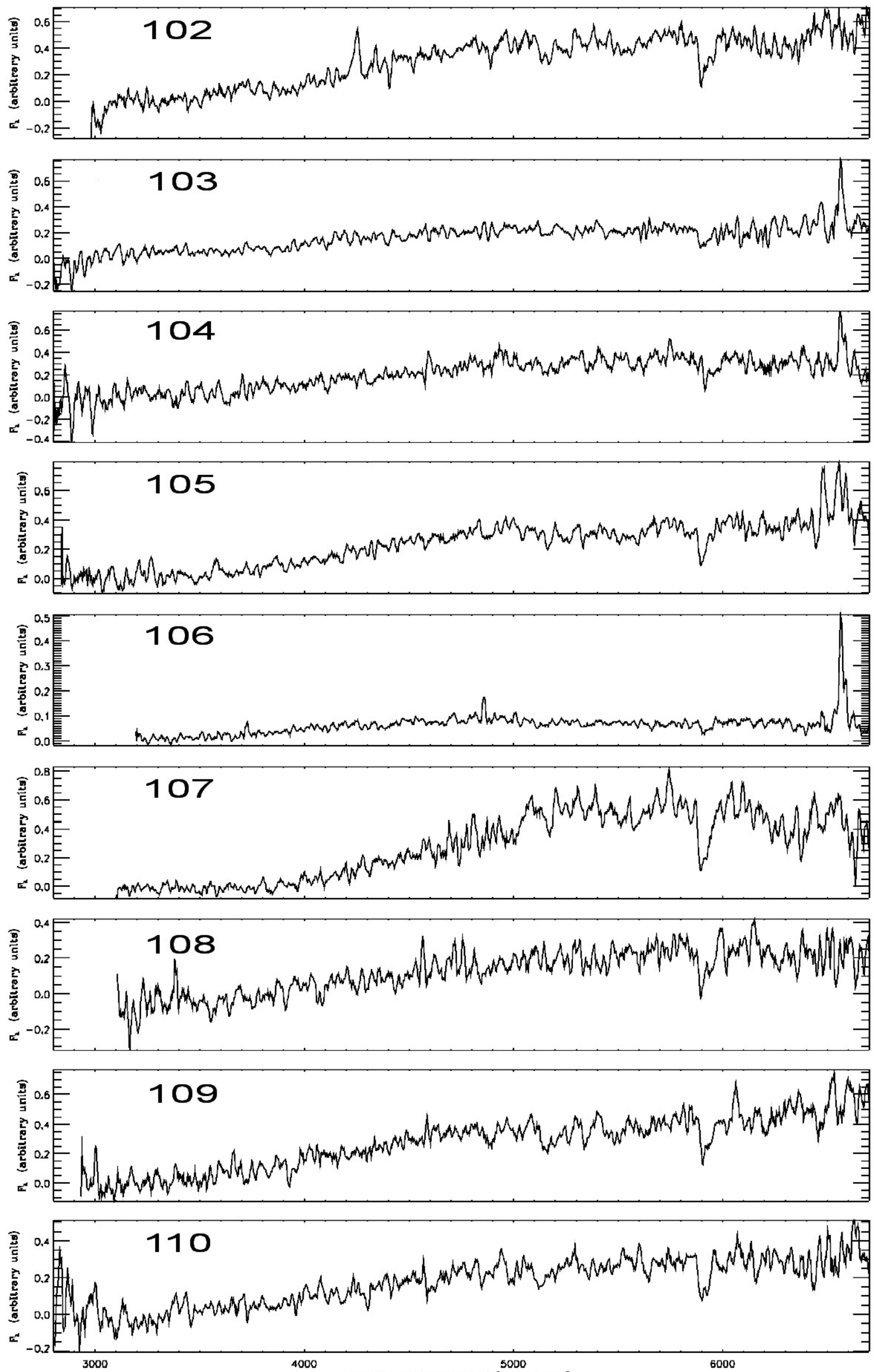

Figure 1.7 Rest-frame spectra of the members of Cluster SpARCS J022258-040715 at $z = 0.288$ (See table 1.9).

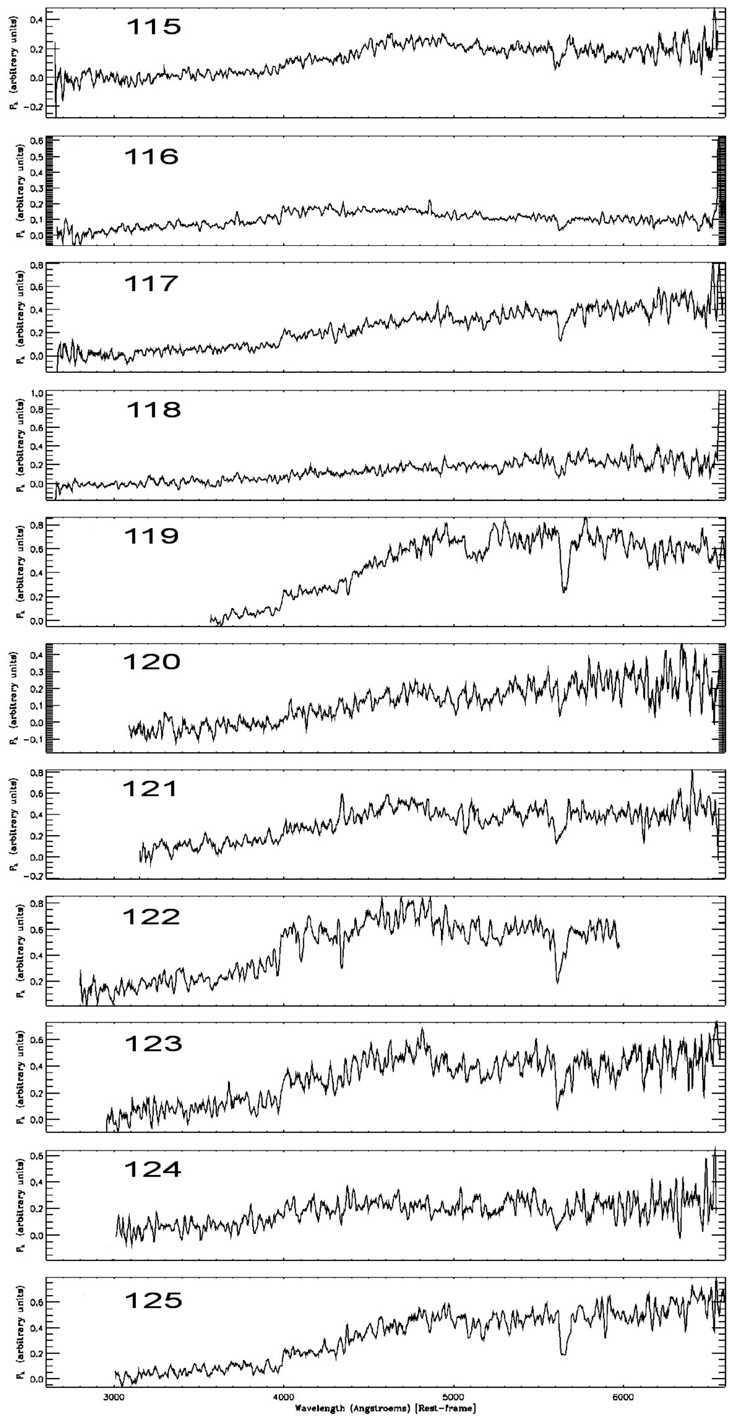

Figure 1.8 Rest-frame spectra of the members of Cluster SpARCS J021528-044041 at $z = 0.353$ (See table 1.10).

Table 1.3. Photometric, Redshift and Spectral Type Catalog for Cluster FLS J171059+593416

ID	Galaxy	R.A.	Dec.	z	R	[3.6]	F_{24}	BPT	MORPHS	Template
					Cluster Members					
1	FLS 3-1-9	257.8326	59.59872	0.1269	18.624	15.107 ± 0.029	1336	-	-	Active
2	FLS 3-2-12	257.7427	59.57616	0.1242	20.889	16.532 ± 0.066	638	-	-	Active
3	FLS 3-1-15-1	257.7396	59.57548	0.1234	19.779	16.869 ± 0.079	-	-	e(c)	-
4	FLS 3-2-10	257.7616	59.57774	0.1203	18.179	15.130 ± 0.036	-	-	-	S0
5	MMT 4549[a]	257.7705	59.53909	0.12679[a]	17.810	14.500 ± 0.030	189	-	-	SF[a]
6	77199[b]	257.7479	59.57323	0.12769	19.709 ± 0.164	-	-	-	-	-
7	80086[b]	257.6126	59.62269	0.12625	20.414 ± 0.354	-	-	-	-	-
					Field					
8	FLS 3-2-7	257.7939	59.55098	0.1399	19.534	99	345	-	e(a)	-
9	FLS 3-3-11	257.7252	59.59555	0.1398	19.739	17.024 ± 0.067	191	SF_1 - SF_2	e(b)	-
10	FLS 3-3-10	257.7172	59.58618	0.1402	18.099	14.791 ± 0.033	1984	Composite - SF_2	e(c)	-
11	FLS 3-1-1	257.9215	59.60484	0.2554	19.788	16.815 ± 0.077	638	Composite - Seyfert	e(a)	-
12	FLS 3-1-10	257.8240	59.56430	0.1757	19.254	16.146 ± 0.045	1029	Composite - SF_2	e(c)	-
13	FLS 3-1-16	257.7236	59.58711	0.2819	20.389	17.331 ± 0.100	825	AGN - Seyfert	e(b)	-
14	FLS 3-1-18	257.7015	59.57085	0.4450	20.809	17.330 ± 0.098	404	-	e(b)	-
15	FLS 3-1-20	257.6430	59.62735	0.4734	20.640	99	458	-	e(b)	-
16	FLS 3-3-12	257.7428	59.60126	0.3862	19.739	16.304 ± 0.049	638	-	e(c)	-

Note. — . Coordinates are in J2000 epoch. Column 5 is the redshift. Column 6, 7 and 8 are the magnitude in R band (Vega), the total magnitude in the 3.6 μm band (Vega) and 24 μm flux in μJy. Column 9 and 10 are the spectral types based on BPT and MORPHS classifications. Column 11 is the spectral type based on the template used for seeking the redshift or the label from the references. In column 9, SF_1 is the identified Star forming galaxy based on [O III]/Hβ versus [N II]/Hα diagram and SF_2 is the identified Star forming galaxy based on [O III]/Hβ versus [S II]/Hα diagram.

[a]Star forming galaxy, Data from Papovich et al. (2006).

[b]All data for this galaxy are from Adelman-McCarthy et al. (2009). This Galaxy was not included in star formation rate analysis.

Table 1.4. As for Table 1.3, but for FLS J172408+591904 and FLS J172449+592122

ID	Galaxy	R.A.	Dec.	z	R	[3.6]	F_{24}	BPT	MORPHS	Template
					FLS J172408+591904					
17	FLS 13-1-1	261.2079	59.33123	0.2424	21.347	17.428 ± 0.079	320	AGN - LINER	e(a)	-
20	FLS 13-1-22	260.9406	59.36170	0.2485	20.111	15.883 ± 0.049	1601	-	e(a)	-
21	FLS 13-1-23	260.9247	59.33210	0.2495	19.823	17.148 ± 0.095	276	SF_1	e(b)	-
25	FLS 17-2-16	261.1508	59.32713	0.2487	20.697	16.805 ± 0.080	311	-	k+a	-
28	FLS 17-1-5-2[a]	261.2990	59.3900	0.2464	-	-	-	-	-	Starburst
29	FLS 17-1-18[a]	261.0490	59.3590	0.2476	-	-	-	-	-	Active
					FLS J172449+592122					
18	FLS 13-1-11	261.0672	59.32601	0.2550	20.068	17.031 ± 0.079	604	-	e(a)	-
19	FLS 13-1-16	261.0105	59.36457	0.2553	19.328	15.804 ± 0.048	351	-	e(a)	-
22	FLS 17-1-17	261.0637	59.41079	0.2530	19.278	15.403 ± 0.041	1020	-	e(c)	-
23	FLS 17-1-16	261.0812	59.40048	0.2522	19.758	16.281 ± 0.048	610	Composite - SF_2	e(a)	-
24	FLS 17-2-14	261.1677	59.34908	0.2560	19.656	16.162 ± 0.049	421	-	e(c)	-
26	FLS 17-2-18	261.1229	59.34532	0.2538	20.347	17.360 ± 0.105	378	SF_1 - SF_2	e(a)	-
27	FLS 17-2-19	261.1097	59.31786	0.2540	20.497	16.607 ± 0.069	1138	Composite - SF_2	e(a)	-
					Field					
30	FLS 13-1-15	261.0217	59.31707	0.2351	20.178	17.314 ± 0.090	163	SF_1 - SF_2	e(a)	-
31	FLS 17-2-9	261.2346	59.36420	0.2702	19.837	16.096 ± 0.049	274	-	-	Active
32	FLS 17-1-5-1	261.2774	59.39133	0.2808	20.599	16.746 ± 0.073	615	AGN - Seyfert	-	-
33	FLS 17-1-14	261.1411	59.40927	0.2339	20.387	15.917 ± 0.049	885	SF_1 - SF_2	e(c)	-
34	FLS 17-3-6	261.0860	59.38788	0.2787	20.578	16.838 ± 0.061	535	SF_1 - SF_2	e(a)	-
35	FLS 17-1-13	261.1515	59.38137	0.1474	19.056	15.442 ± 0.042	913	-	e(a)	-

Table 1.4—Continued

ID	Galaxy	R.A.	Dec.	z	R	[3.6]	F_{24}	BPT	MORPHS	Template
36	FLS 17-1-19	261.0257	59.3980	0.1848	19.828	17.042 ± 0.092	300	-	-	Active
37	FLS 17-2-25	261.0263	59.31465	0.3390	20.258	16.394 ± 0.054	376	-	e(c)	-
38	FLS 17-3-1	261.0292	59.37160	0.0796	18.568	15.672 ± 0.038	730	-	k+a	-
39	FLS 17-3-12	261.1863	59.34052	0.1860	20.257	99	372	SF_1 - SF_2	e(b)	-
40	FLS 17-3-20	261.3212	59.33223	0.3205	19.896	17.187 ± 0.070	913	AGN	e(c)	-
41	FLS 13-1-26-1	260.8743	59.33390	0.1164	19.293	15.629 ± 0.041	681	-	e(b)	-

Note. — . This system is two separate clusters, which are likely about to merge.

[a]Photometric data are not available

Table 1.5. As for Table 1.3, but for FLS J171505+585941

ID	Galaxy	R.A.	Dec.	z	R	[3.6]	F_{24}	BPT	MORPHS	Template
					Cluster Members					
42	FLS 16-3-13	258.7822	58.98791	0.2532	18.295	14.577 ± 0.024	1309	-	k	-
43	FLS 16-1-16	258.7448	58.99221	0.2503	19.425	15.919 ± 0.054	-	-	-	Ell
44	FLS 16-2-12	258.7718	58.99484	0.2520	18.335	14.759 ± 0.027	-	-	-	Ell
45	FLS 16-3-13	258.7519	58.99911	0.2540	19.365	15.796 ± 0.047	-	-	-	Ell
46	MMT 4157[a]	258.6750	59.00408	0.25387[a]	19.317	15.601 ± 0.042	524	-	-	SF[a]
					Field					
47	FLS 16-1-20	258.6852	58.98988	0.2111	20.038	16.253 ± 0.044	3556	Composite - Seyfert	-	-
48	FLS 16-2-21	258.6180	58.94561	0.3837	20.349	16.670 ± 0.071	144	-	e(a)	-
49	FLS 16-2-22	258.5983	58.97321	0.2904	19.359	15.604 ± 0.045	575	-	e(a)	-
50	FLS 16-3-14	258.7973	58.96305	0.1150	19.326	15.060 ± 0.027	2155	-	e(a)	-

[a]Star forming galaxy, Data from Papovich et al. (2006).

Table 1.6. As for Table 1.3, but for FLS J171431+595752

ID	Galaxy	R.A.	Dec.	z	R	[3.6]	F_{24}	BPT	MORPHS	Template
					Cluster Members					
51	FLS 18-2-15	258.6508	59.95020	0.2152	18.758	15.238 ± 0.038	1040	-	e(c)	-
52	FLS 18-3-3	258.4747	58.91577	0.2221	20.205	16.812 ± 0.061	312	-	e(c)	-
53	MMT 5123[a]	258.6581	60.07997	0.21562[a]	19.694	19.983 ± 0.066	467	SF_1 - SF_2	e(b)	-
54	MMT 5887[a]	258.3849	59.91540	0.22206[a]	20.045	17.202 ± 0.097	671	SF_1 - SF_2	e(a)	-
55	MMT 5950[a]	258.6259	59.83126	0.22210[a]	20.421	17.015 ± 0.069	467	-	-	star froming
56	MMT 5921[a]	258.6042	59.79118	0.22225[a]	19.619	16.106 ± 0.053	1853	-	k+a	-
57	MMT 5159[a]	258.8627	60.00244	0.22679[a]	20.829	16.614 ± 0.069	356	-	e(a)	-
58	MMT 5223[a]	258.7690	59.86913	0.23025[a]	19.507	16.403 ± 0.061	1013	SF_1 - SF_2	e(a)	Starburst[a]
					Field					
59	FLS 18-1-7	258.5673	59.97124	0.2881	20.608	17.178 ± 0.068	166	-	e(a)	-
60	FLS 18-1-17-1	258.6826	59.95018	0.4263	19.818	15.435 ± 0.041	759	-	k	-
61	FLS 18-2-13	258.6246	59.89004	0.3817	20.046	16.908 ± 0.079	385	-	e(a)	-
62	FLS 18-2-17	258.6796	59.94032	0.3569	20.858	17.770 ± 0.125	-	-	e(a)	-
63	FLS 18-3-1	258.4420	59.97748	0.4580	19.949	15.583 ± 0.032	2229	-	e(a)	-
64	FLS 18-3-4	258.4823	59.93023	0.1280	19.547	15.190 ± 0.035	916	-	e(a)	-
65	FLS 18-3-12	258.6217	59.95785	0.1894	18.618	15.111 ± 0.033	2817	-	e(c)	-
66	FLS 18-3-15	258.6560	59.94671	0.1958	19.148	15.556 ± 0.042	11726	SF_1 - SF_2	e(n)	QSO
67	FLS 18-2-22-2	258.7703	59.94345	0.1838	21.909	17.273 ± 0.080	282	-	-	Active
68	FLS 18-2-19	258.7196	59.93686	0.2645	21.478	17.450 ± 0.105	196	AGN - LINER	-	-
69	FLS 18-1-12	258.6257	59.96982	0.2716	19.298	15.817 ± 0.034	611	-	-	Sb
70	FLS 18-1-20	258.7404	59.96468	0.2719	18.698	15.061 ± 0.027	2594	-	-	Sa

Table 1.6—Continued

ID	Galaxy	R.A.	Dec.	z	R	[3.6]	F_{24}	BPT	MORPHS	Template
71	FLS 18-1-9	258.5986	59.98917	0.2474	19.748	16.260 ± 0.042	-	-	-	Ell
72	FLS 18-1-11	258.6143	59.94530	0.24665	18.467	14.883 ± 0.032	-	-	-	Ell

[a]Data from Papovich et al. (2006).

Table 1.7. As for Table 1.3, but for SpARCS J104101+581741

ID	Galaxy	R.A.	Dec.	z	z'	[3.6]	F_{24}	BPT	MORPHS	Template
					Cluster Members					
73	Lock 3-1-1	160.41621	58.31722	0.0716	15.611 ± 0.001	13.342 ± 0.105	2412	-	k	-
74	Lock 3-1-15	160.23210	58.30442	0.0710	15.965 ± 0.001	13.973 ± 0.105	230	-	-	Passive
75	Lock 3-1-14	160.24507	58.28425	0.0699	16.569 ± 0.001	13.990 ± 0.105	10286	AGN - SF_2	e(n)	QSO
76	Lock 3-1-19	160.16212	58.33630	0.0718	17.769 ± 0.002	15.529 ± 0.105	995	SF_1 - Seyfert	-	-
77	Lock 3-2-14	160.20708	58.25690	0.0733	15.936 ± 0.001	13.863 ± 0.105	689	-	k	-
78	Lock 3-1-13	160.25443	58.29493	0.0726	15.384 ± 0.002	13.387 ± 0.105	571	-	-	Ell
79	Lock 3-1-20	160.15352	58.29995	0.0759	16.327 ± 0.001	14.377 ± 0.105	- -	-	-	Ell
80	746934	160.10091	58.15513	0.070[a]	19.259 ± 0.005	17.003 ± 0.115	5623	-	-	Starburst[a]
81	852277	159.74420	58.37610	0.069[a]	- - -	19.969 ± 0.363	19641	-	-	Starburst[a]
					Field					
82	Lock 3-1-6	160.35872	58.28945	0.2307	17.469 ± 0.001	15.106 ± 0.105	3479	AGN - Seyfert	e(c)	-
83	Lock 3-1-9	160.29755	58.27360	0.2302	18.987 ± 0.007	16.675 ± 0.105	816	AGN - Seyfert	e(a)	-
84	Lock 3-1-21	160.13600	58.27993	0.1321	16.574 ± 0.002	14.448 ± 0.105	2270	SF_1 - SF_2	e(n)	QSO
85	Lock 3-1-22	160.12114	58.32009	0.3076	18.418 ± 0.003	15.953 ± 0.105	869	-	-	Active

Note. — . For SpARCS clusters column 5 is the magnitude in z' band (Vega).

[a]Data from Sargsyan & Weedman (2009). The redshift was not considered for the cluster's redshift analysis.

Table 1.8. As for Table 1.3, but for SpARCS J104209+575350

ID	Galaxy	R.A.	Dec.	z	z'	[3.6]	F_{24}	BPT	MORPHS	Template
					Cluster Members					
86	Lock 34-2-18	160.42569	57.86704	0.4784	19.113 ± 0.007	16.291 ± 0.106	343	-	a+k	-
87	Lock 34-2-21	160.38460	57.84986	0.4924	19.375 ± 0.009	16.765 ± 0.106	824	-	e(c)	-
88	Lock 34-1-10	160.55428	57.91573	0.4893	19.074 ± 0.006	16.325 ± 0.106	- -	-	-	Ell
89	Lock 34-1-11	160.54018	57.89741	0.4905	18.188 ± 0.003	15.257 ± 0.105	- -	-	-	Ell
90	Lock 34-2-9-1	160.58777	57.89862	0.4893	19.106 ± 0.006	16.165 ± 0.105	- -	-	-	Ell
91	Lock 34-2-11	160.55391	57.89756	0.4820	18.689 ± 0.005	15.885 ± 0.105	- -	-	-	Sa
					Field					
92	Lock 34-1-2	160.69905	57.89442	2.22	19.755 - 0.014	16.642 - 0.106	730	-	e(n)	AGN type 1
93	Lock 34-1-3-1	160.66032	57.92509	2.98	19.605 ± 0.010	17.344 ± 0.108	191	-	e(n)	AGN type 1
94	Lock 34-1-12	160.52074	57.95263	0.1990	18.355 ± 0.003	16.228 ± 0.105	471	SF_1 - SF_2	-	Active
95	Lock 34-1-21	160.42108	57.93959	0.1524	18.240 ± 0.003	16.197 ± 0.105	240	SF_1 - SF_2	e(c)	-
96	Lock 34-1-22	160.40965	57.89880	0.2864	18.915 ± 0.005	16.896 ± 0.107	263	Composite - SF_2	e(a)	-
97	Lock 34-1-23	160.38048	57.91756	0.4268	19.375 ± 0.009	16.765 ± 0.106	195	-	e(a)	-
98	Lock 34-2-2	160.69498	57.86621	0.1819	18.721 ± 0.005	17.036 ± 0.106	348	Composite Seyfert	-	-
99	Lock 34-2-4	160.66849	57.84680	0.3341	18.081 ± 0.003	15.525 ± 0.105	961	-	k	-
100	Lock 34-2-5	160.65347	57.85717	0.0735	17.736 ± 0.002	16.157 ± 0.105	339	AGN Seyfert	e(a)	-
101	Lock 34-2-9-2	160.58771	57.89868	0.3196	- - -	- - -	149	-	e(b)	-

Table 1.9. As for Table 1.3, but for SpARCS J022258-040715

ID	Galaxy	R.A.	Dec.	z	z'	[3.6]	F_{24}	BPT	MORPHS	Template
					Cluster Members					
102	XMM 4-1-2	35.82792	-4.07131	0.2891	18.197 ± 0.003	15.197 ± 0.105	419	-	e(c)	-
103	XMM 4-1-7	35.79328	-4.10123	0.2894	18.758 ± 0.004	16.151 ± 0.106	700	SF_1	e(a)	-
104	XMM 4-1-11	35.75901	-4.09267	0.2847	18.610 ± 0.003	16.485 ± 0.106	315	-	-	Passive
105	XMM 4-1-18	35.70670	-4.07833	0.2888	17.674 ± 0.002	15.015 ± 0.105	1129	-	e(c)	-
106	XMM 4-2-7	35.77528	-4.10599	0.2863	18.999 ± 0.005	16.819 ± 0.106	529	SF_1 - SF_2	e(b)	-
107	XMM 4-1-14	35.73452	-4.10968	0.2896	17.855 ± 0.002	15.530 ± 0.105	- -	-	-	Ell
108	XMM 4-1-15	35.73036	-4.11694	0.2888	19.044 ± 0.006	16.752 ± 0.106	- -	-	-	Ell
109	XMM 4-2-11	35.75026	-4.11926	0.2864	18.546 ± 0.003	16.375 ± 0.106	- -	-	-	Ell
110	XMM 4-2-13	35.73729	-4.13154	0.2880	18.643 ± 0.004	16.368 ± 0.105	- -	-	-	Ell
					Field					
111	XMM 4-1-10	35.76422	-4.07842	0.9189	17.516 ± 0.001	16.032 ± 0.105	- -	-	k	-
112	XMM 4-1-20	35.68272	-4.10897	0.1013	17.369 ± 0.001	15.070 ± 0.105	1324	Composite - SF_2	-	Active
113	XMM 4-2-2	35.82383	-4.13609	0.1491	18.291 ± 0.003	16.072 ± 0.105	247	Composite Seyfert	e(a)	-
114	XMM 4-2-8	35.76865	-4.16036	0.2710	17.837 ± 0.002	15.653 ± 0.105	- -	-	-	Sa

Table 1.10. As for Table 1.3, but for SpARCS J021528-044041

ID	Galaxy	R.A.	Dec.	z	$z\,'$	[3.6]	F_{24}	BPT	MORPHS	Template
					Cluster Members					
115	XMM 13-1-14	33.87399	-4.67971	0.3572	18.039 ± 0.002	15.555 ± 0.105	- -	-	k+a	-
116	XMM 13-2-15	33.85736	-4.70205	0.3514	19.445 ± 0.006	17.168 ± 0.107	216	SF_1	e(a)	-
117	XMM 13-1-8	33.90405	-4.67940	0.3510	18.266 ± 0.002	15.752 ± 0.105	161	-	-	Ell
118	XMM 13-1-12	33.88244	-4.66522	0.3556	18.726 ± 0.005	15.806 ± 0.105	711	-	-	Sa
119	XMM 13-1-15	33.86757	-4.67812	0.3462	17.204 ± 0.002	14.642 ± 0.105	- -	-	-	Ell (BCG)
120	XMM 13-1-16	33.86019	-4.67546	0.3508	19.194 ± 0.005	16.723 ± 0.106	- -	-	-	Sa
121	XMM 13-2-1	33.97503	-4.67478	0.3565	18.760 ± 0.005	16.210 ± 0.105	- -	-	-	Sa
122	XMM 13-2-7	33.92888	-4.72418	0.3554	18.341 ± 0.002	15.784 ± 0.105	981	-	-	Sa
123	XMM 13-2-8	33.92080	-4.71598	0.3544	19.169 ± 0.005	16.681 ± 0.106	- -	-	-	Ell
124	XMM 13-2-11	33.88952	-4.68907	0.3588	19.327 ± 0.006	16.792 ± 0.106	477	-	-	Sb
125	XMM 13-2-13-1	33.87223	-4.68195	0.3495	17.920 ± 0.004	15.421 ± 0.105	- -	-	-	Ell
					Field					
126	XMM 13-1-22	33.81547	-4.63557	0.0413	16.927 ± 0.001	15.328 ± 0.105	11725	SF_1 - SF_2	e(n)	QSO
127	XMM 13-2-17	33.83600	-4.71398	0.2902	18.568 ± 0.003	16.246 ± 0.107	472	-	e(c)	-
128	XMM 13-2-19	33.81490	-4.67687	0.1371	19.165 ± 0.006	17.431 ± 0.112	215	-	-	Active
129	XMM 13-1-10	33.89537	-4.65351	0.3409	18.543 ± 0.004	16.135 ± 0.105	- -	-	-	Ell

Table 1.11. As for Table 1.3, but for other Field Galaxies

ID	Galaxy	R.A.	Dec.	z	z'	[3.6]	F_{24}	BPT	MORPHS	Template
130	XMM 1-1-4	34.74628	-3.81911	0.1279	17.945 ± 0.002	15.836 ± 0.106	1182	SF_1 -SF_2	e(c)	-
131	XMM 1-2-5	34.73731	-3.84519	0.2249	18.908 ± 0.004	16.630 ± 0.106	3143	-	-	Active
132	XMM 27-1-8	35.47009	-3.74885	0.5951	17.895 ± 0.002	15.759 ± 0.106	714	-	k	-
133	XMM 27-2-8	35.47078	-3.80965	0.4259	18.567 ± 0.003	15.764 ± 0.106	251	-	e(c)	-
134	XMM 27-2-10-2	35.44691	-3.78219	0.1990	18.621 ± 0.003	15.881 ± 0.106	225	-	e(b)	-
					R					
135	FLS 5-3-1	259.33070	59.26381	0.1836	20.442	16.028 ± 0.049	406	SF_1 - SF_2	e(b)	-

Note. — . For the galaxies in SpARCS fields column 5 is the magnitude in z' band (Vega) and for the galaxies in First Look Survey field column 5 is the magnitude in R band (Vega). The field galaxies in this table were identified in the fields of some of our targeted candidate clusters that we were unable to confirm them as a cluster due to lack of confirmed members.

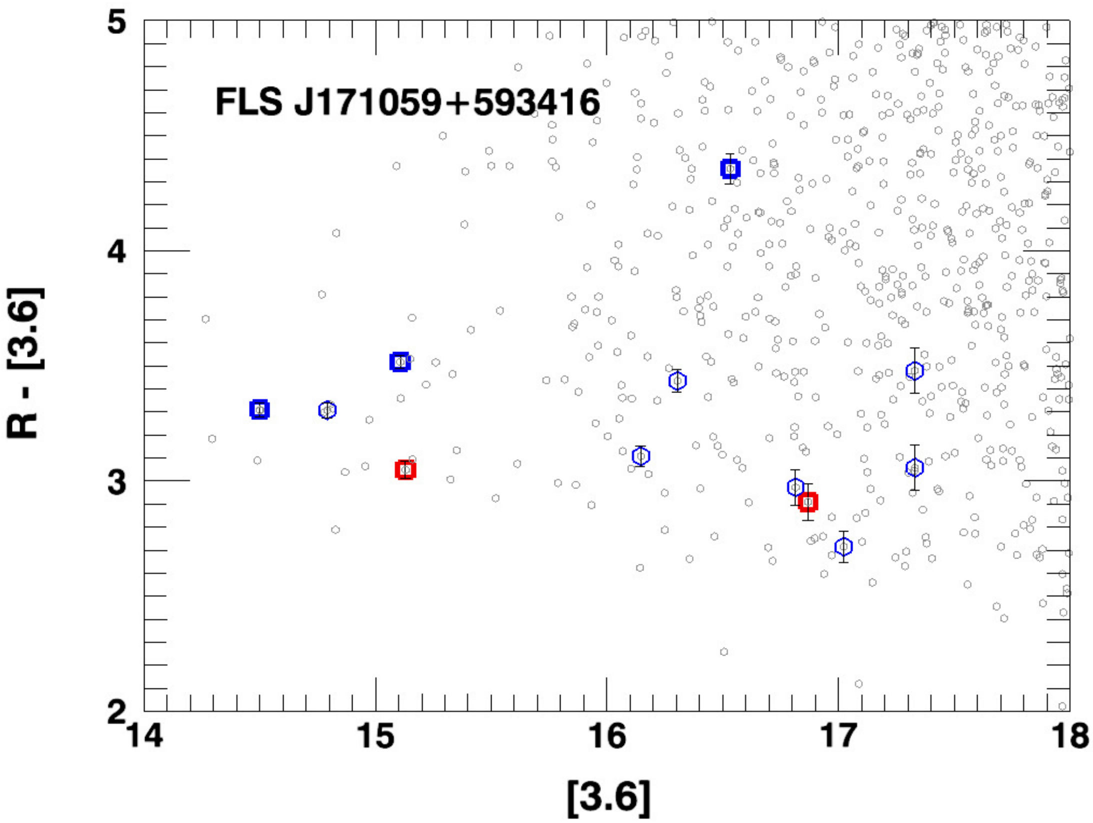

Figure 1.9 R - [3.6] vs. [3.6] color-magnitude diagram for FLS J171059+593416. The boxes are confirmed cluster members and circles are confirmed foreground/background field galaxies. Blue color is for 24 μm detected galaxies and Red color is for galaxies without 24 μm detections. Note that we plot those galaxies that have both R and [3.6] magnitudes in the catalog (table 1.3). Small background grey circles are identified photometric sources in the field of the cluster from SpARCS survey.

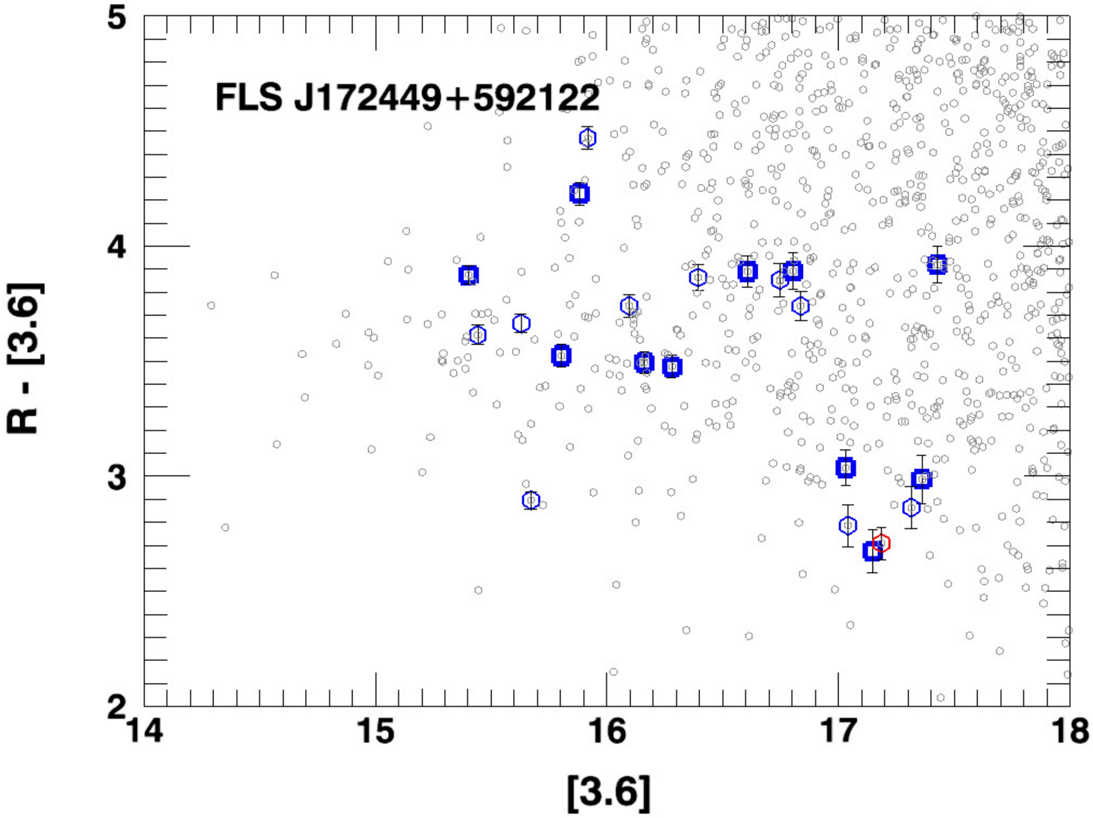

Figure 1.10 As for Figure 1.9, but for FLS J172408+591904 and FLS J172449+592122

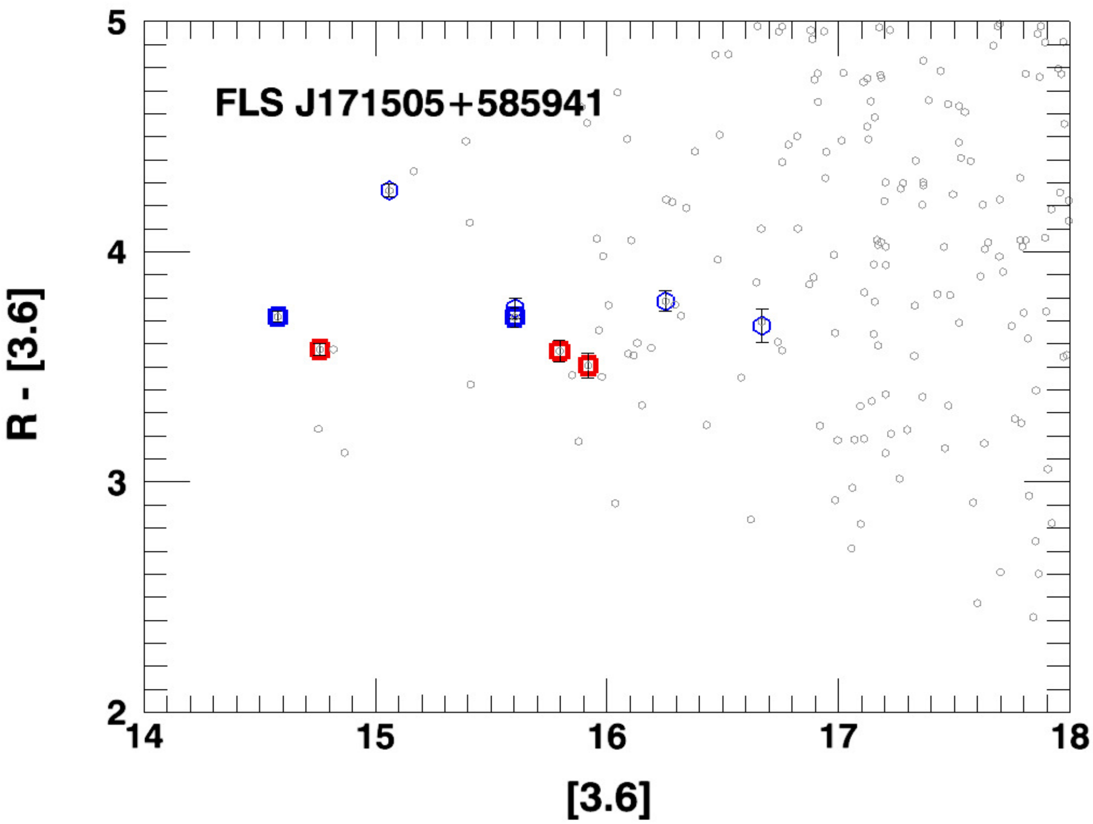

Figure 1.11 As for Figure 1.9, but for FLS J171505+585941

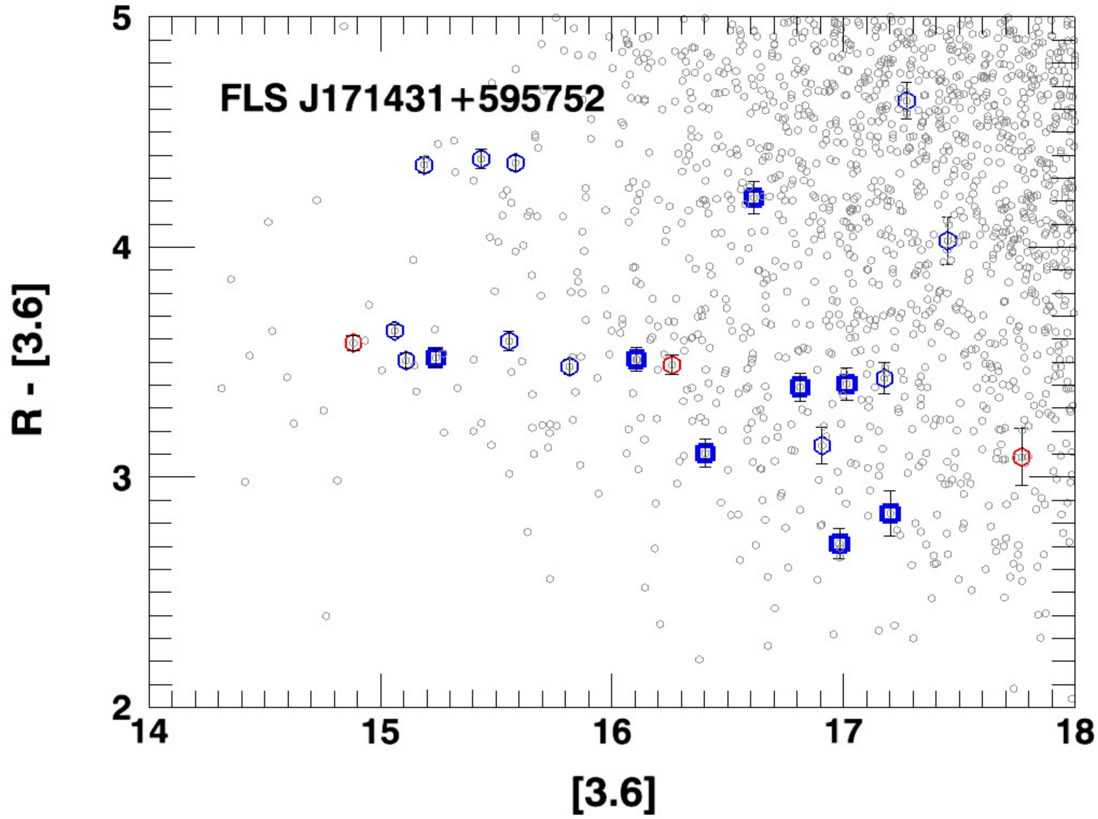

Figure 1.12 As for Figure 1.9, but for FLS J171431+595752

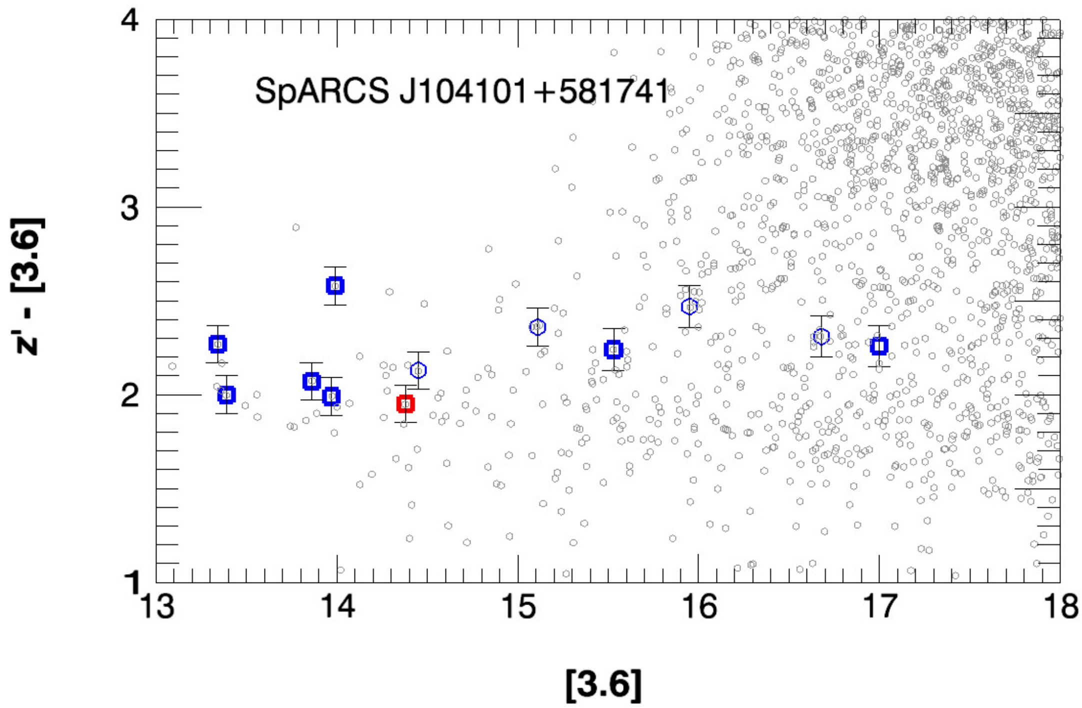

Figure 1.13 z' - [3.6] vs. [3.6] color-magnitude diagram for SpARCS J104101+581741. The boxes are confirmed cluster members and circles are confirmed foreground/background field galaxies. Blue color is for 24 μm detected galaxies and Red color is for galaxies without 24 μm detections. Note that we plot those galaxies that have both R and [3.6] magnitudes in the catalog (table 1.7). Small background grey circles are identified photometric sources in the field of the cluster from SpARCS survey.

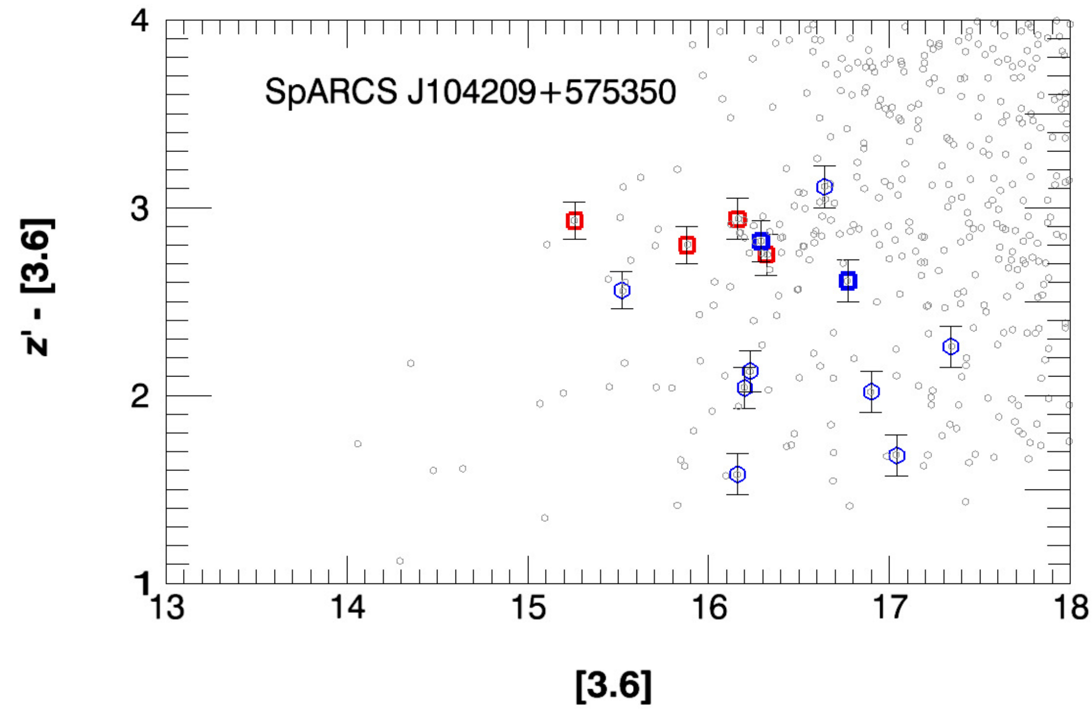

Figure 1.14 As for Figure 1.13, but for SpARCS J104209+575350.

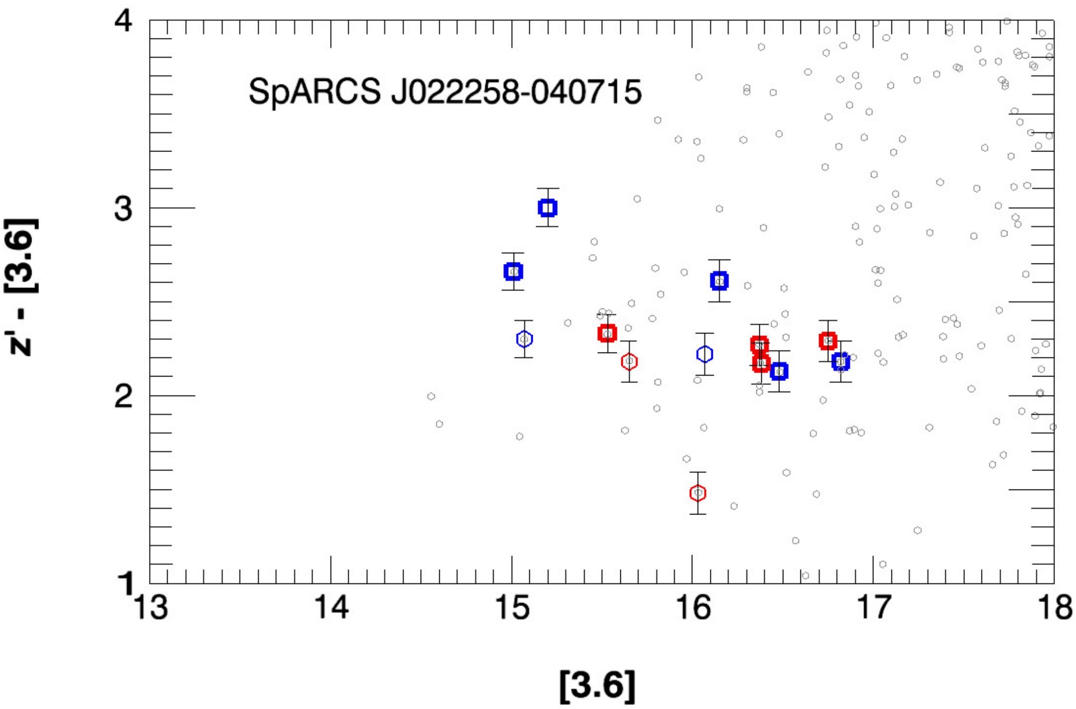

Figure 1.15 As for Figure 1.13, but for SpARCS J022258-040715.

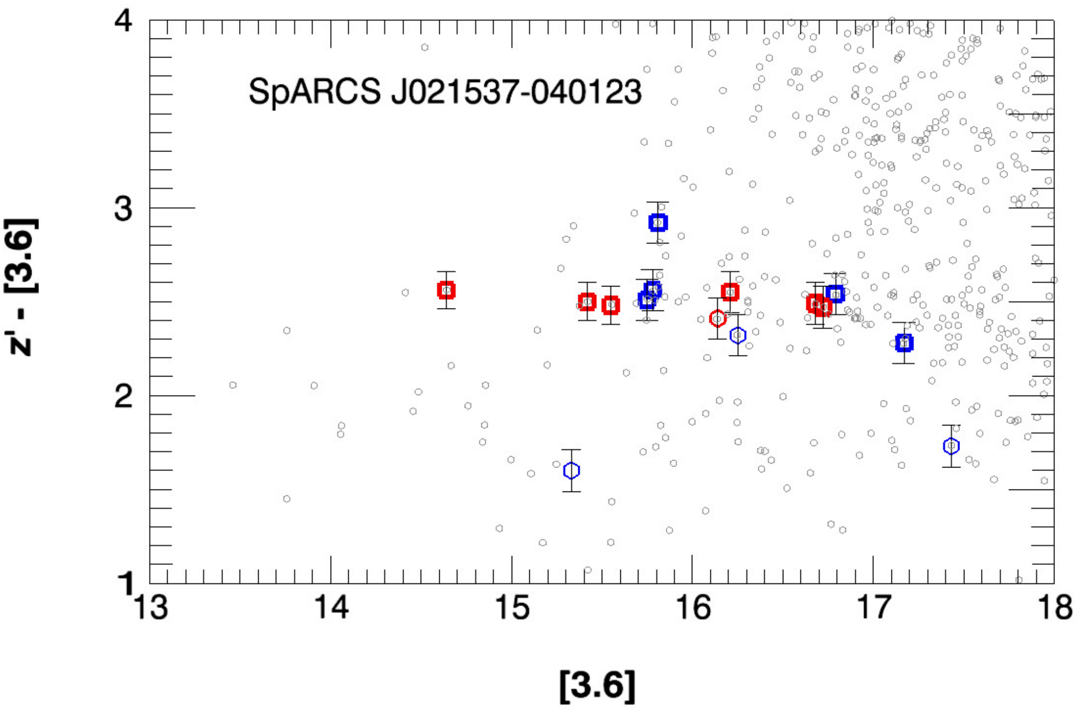

Figure 1.16 As for Figure 1.13, but for SpARCS J021528-044041.

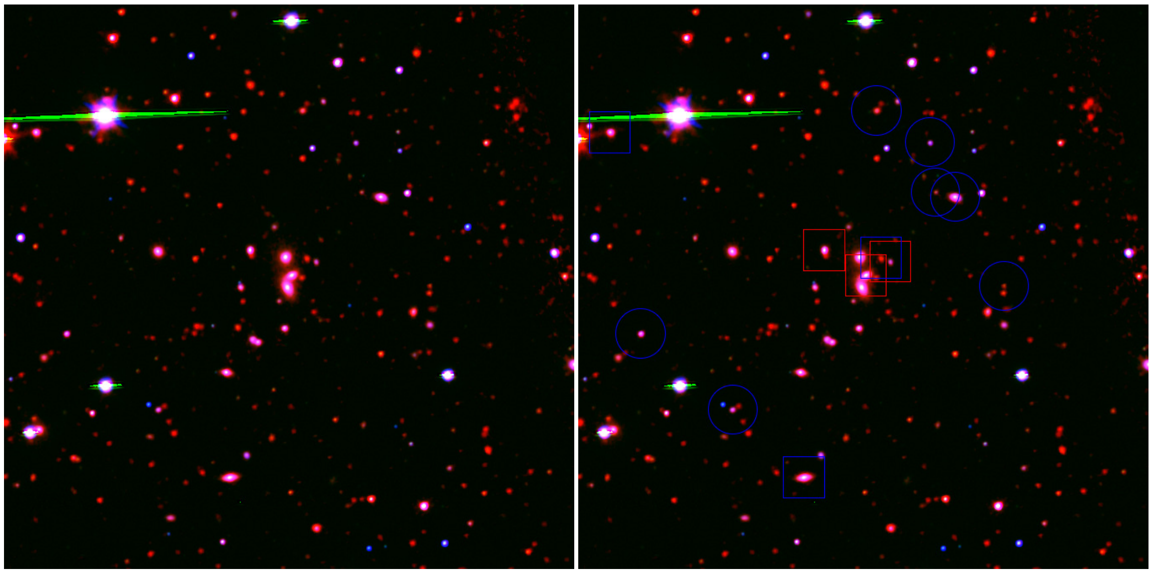

Figure 1.17 FLS J171059+593416. The boxes are confirmed cluster members and circles are foreground/background field galaxies. Blue color is for 24 μm detected galaxies and Red color is for galaxies without 24 μm detections. FOV is 5.8′ (0.8 Mpc). Note that this figure presents only the galaxies in this FOV.

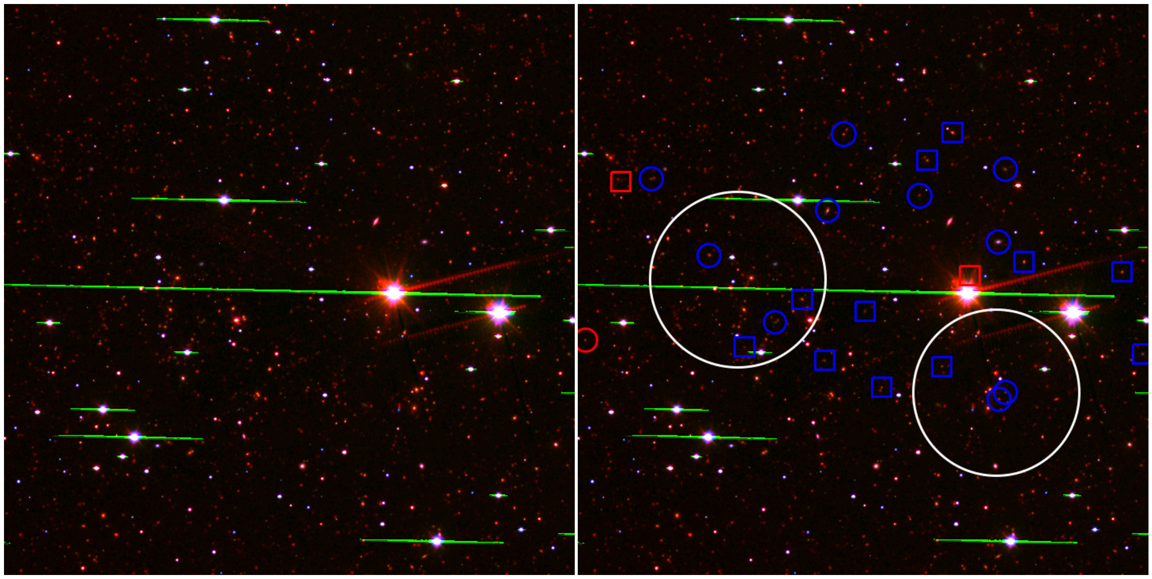

Figure 1.18 As for Figure 1.17, but for FLS J172408+591904 and FLS J172449+592122. FOV is 12.5′ (2.9 Mpc). This system is two separate clusters, which are likely about to merge (See table 1.4 and its comments for more information). The cores are demonstrated by white circles (Left circle : FLS J172408+591904 and Right circle : FLS J172449+592122).

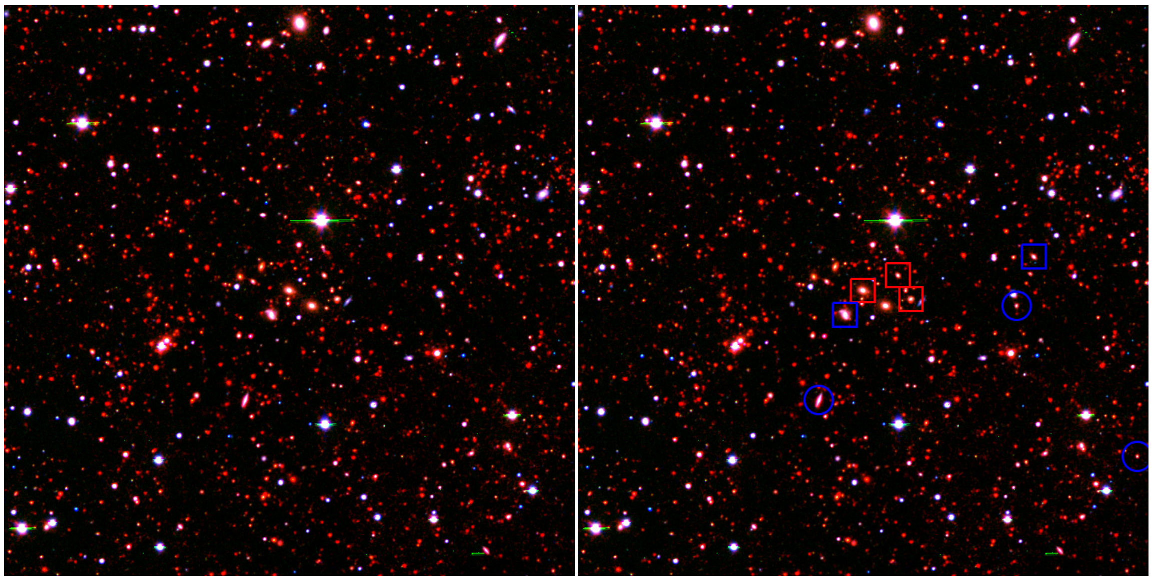

Figure 1.19 As for Figure 1.17, but for FLS J171505+585941. FOV is 8.4′ (2 Mpc).

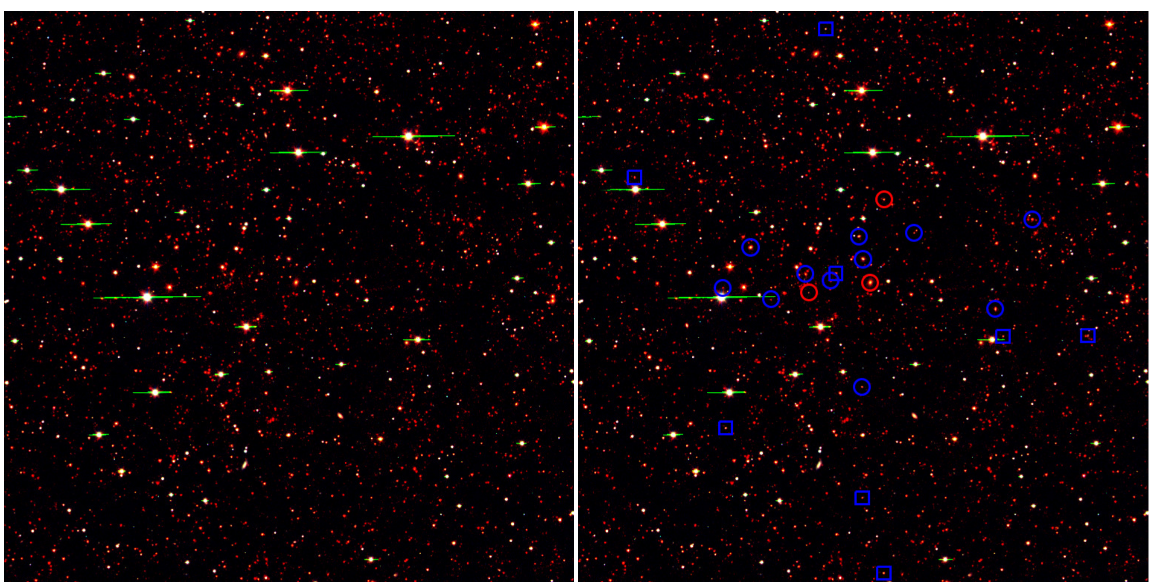

Figure 1.20 As for Figure 1.17, but for FLS J171431+595752. FOV is 18.7′ (4 Mpc).

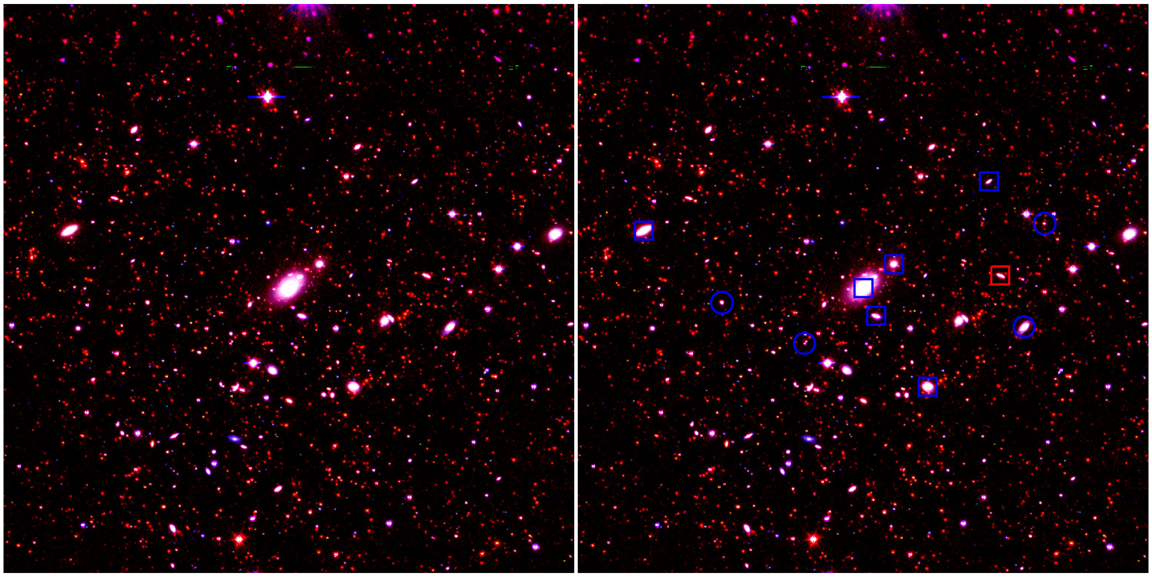

Figure 1.21 As for Figure 1.17, but for SpARCS J104101+581741. FOV is 20′ (1.6 Mpc).

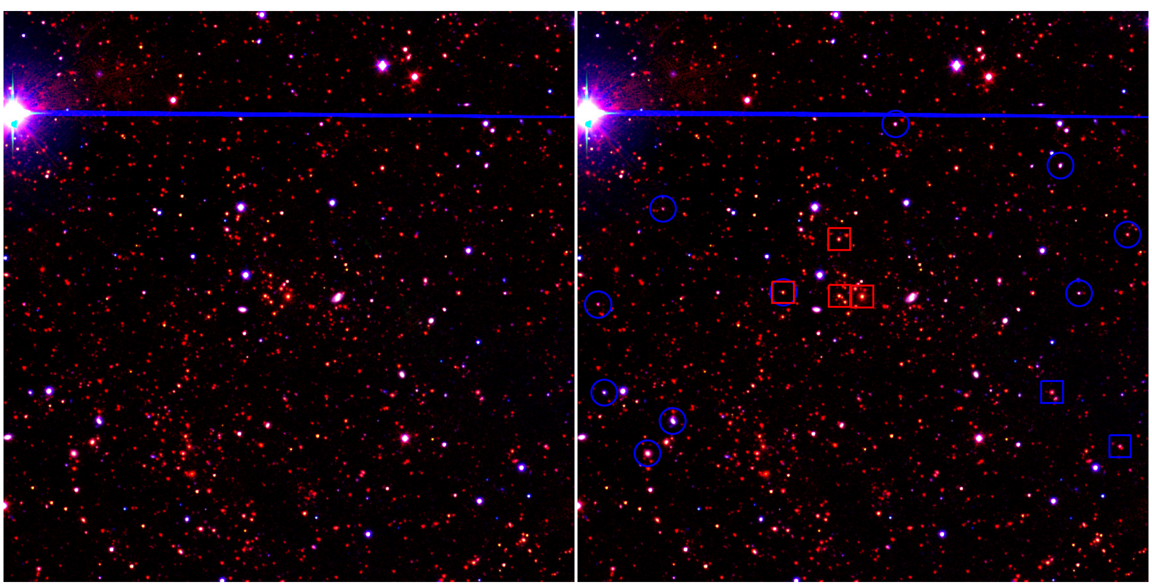

Figure 1.22 As for Figure 1.17, but for SpARCS J104209+575350. FOV is 11′ (4 Mpc).

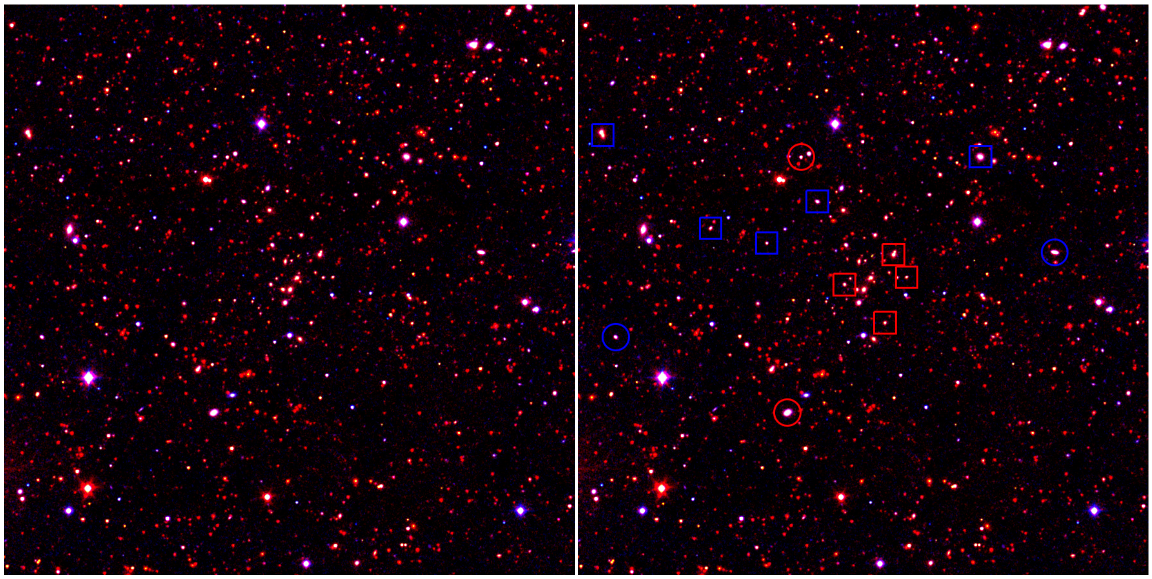

Figure 1.23 As for Figure 1.17, but for SpARCS J022258-040715. FOV is 10.5′ (2.7 Mpc)

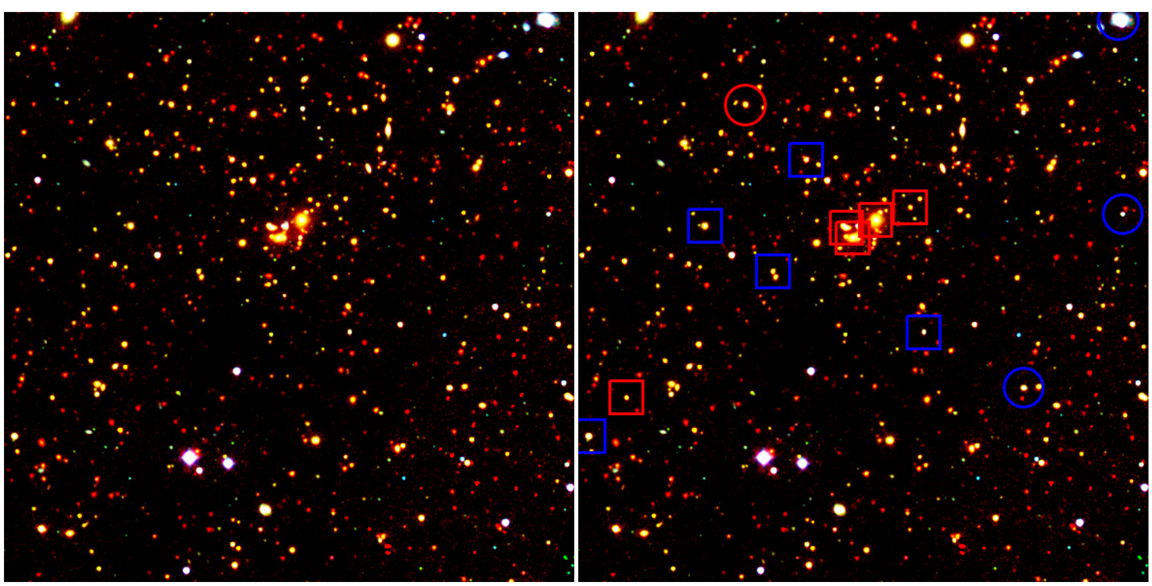

Figure 1.24 As for Figure 1.17, but for SpARCS J021528-044041. FOV is 9.7′ (3 Mpc)

1.4.2 Spectral Classifications

1.4.2.1 BPT Diagrams

We used the spectroscopy of the 24 μm detected galaxies to classify them based on their spectral types. Our first classification was based on the scheme of Baldwin et al. (1981), who classified the dominant energy source in emission line galaxies using three diagnostic diagrams. These diagrams are based on the four optical line ratios [O III]/Hβ, [N II]/Hα, [S II]/Hα, and [O I]/Hα. Since that time, these diagrams have been used commonly and called Baldwin-Phillips-Terlevich (BPT) diagrams.

Kewley et al. (2001) created a theoretical maximum starburst line by a combination of stellar synthesis and photoionization models on the BPT diagrams to distinguish between AGN, LINERS and Star forming galaxies. The maximal starburst lines are defined as:

$$\log([OIII]/H\beta) = 0.61/[\log([NII]/H\alpha) - 0.05] + 1.3 \tag{1.4}$$

$$\log([OIII]/H\beta) = 0.72/[\log([SII]/H\alpha) - 0.32] + 1.3 \tag{1.5}$$

Kauffmann et al. (2003) modified this scheme and included an empirical line to show that some galaxies have spectra with both star forming and AGN components. They called these galaxies "composite" and defined the empirical line as below:

$$\log([OIII]/H\beta) = 0.61/[\log([NII]/H\alpha) - 0.47] + 1.19 \tag{1.6}$$

Based on this classification, we can classify galaxies into AGN, composite and Star forming galaxies as below :

AGN: Galaxies which lie above the maximal starburst lines.

Composite: Galaxies which lie below the maximal starburst line and lie above the empirical line in [N II]/Hα versus [O III]/Hβ diagram.

Star Forming: Galaxies which lie below the empirical line in [N II]/Hα versus [O III]/Hβ diagram and below the maximal starburst line in [S II]/Hα versus [O III]/Hβ diagram.

Also Kewley et al. (2006) showed that AGNs in [S II]/Hα versus [O III]/Hβ diagram can be divided into Seyferts and LINERs by defining this line:

$$\log([OIII]/H\beta) = 1.89 \log([SII]/H\alpha) + 0.76 \tag{1.7}$$

AGNs above this line are likely Seyferts and those below this line are likely LINERs.

We assume each pair of lines in the line ratios are close enough to use equivalent widths (EWs) instead of fluxes in these relations. We plot in Figure 1.25 and Figure 1.26, all 24 μm detected galaxies for which those indexes can be measured. These plots are restricted to those galaxies that have all the required lines at $z < \sim 0.32$ (6 out of 9 clusters), because we no longer have [S II] 6717,6732 lines in our optical spectroscopy after this redshift.

For measuring equivalent width, we used an *IDL* code by Ricardo Demarco based on the method of Worthey & Ottaviani (1997). In this method, the equivalent width is measured by centering a bandpass on the feature and using red and blue sidebands as the continuum reference. A linear fit to the average flux in the blue and red

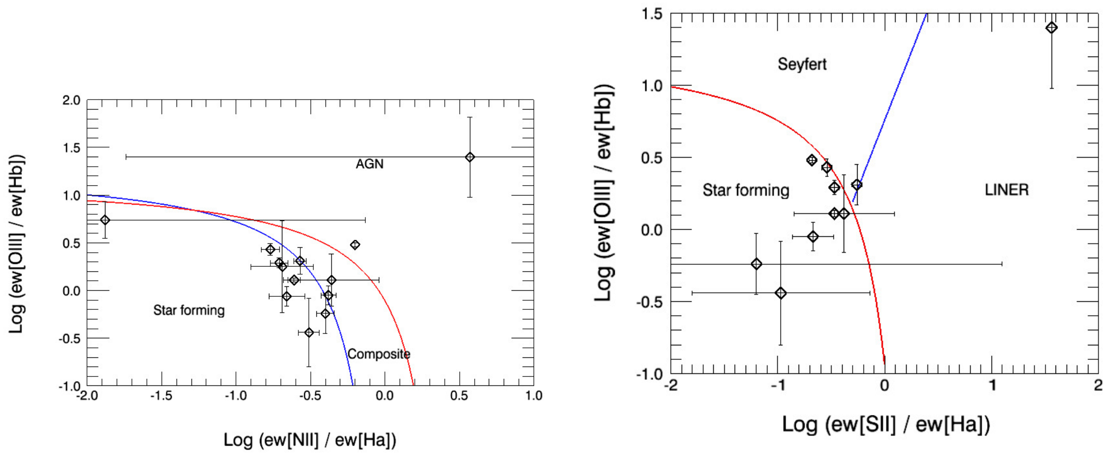

Figure 1.25 BPT diagrams for 24 μm cluster galaxies. Line ratio measurements are presented in table 1.13 and the summary of this classification is presented in table 1.15. Left diagram : The blue line is the theoretical maximum starburst limit from Kewley et al. (2001) and red line is the empirical limit from Kauffmann et al. (2003). Right diagram : The theoretical red line is from Kewley et al. (2001) and the blue line is from Kewley et al. (2006).

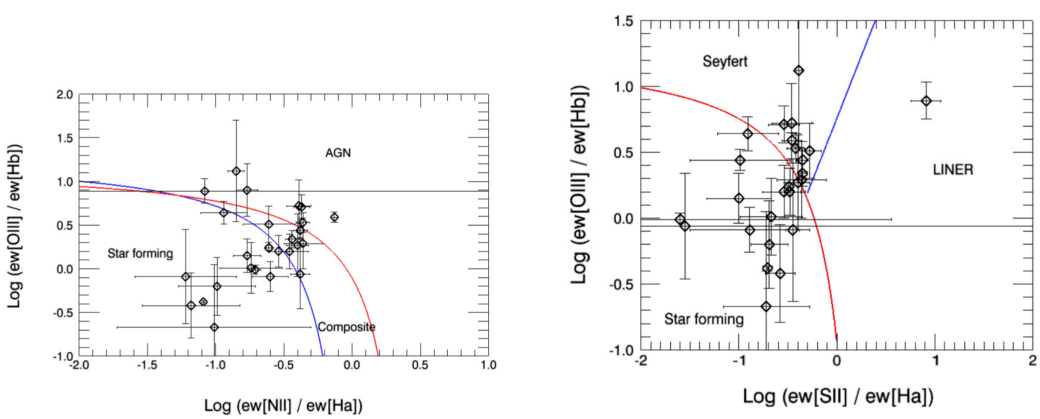

Figure 1.26 As for figure 1.25, but for 24 μm field galaxies. (See table 1.14 and table 1.15)

Table 1.12. Line Strength Index Definitions

Index	Bandpass ($\AA$)	Blue Sideband ($\AA$)	Red Sideband ($\AA$)	Reference
O III	4998.2-5018.2	4978.2-4998.2	5018.2-5038.2	Yan et al. (2006)
N II	6575.3-6595.3	6483.0-6513.0	6623.0-6653.0	Yan et al. (2006)
Hα	6554.6-6574.6	6483.0-6513.0	6623.0-6653.0	Yan et al. (2006)
Hβ	4847.9-4876.6	4799.0-4839.0	3738.3-3758.3	Tran et al. (2003), Fisher et al. (1998)
S II	6704.0-6740.0	6623.0-6653.0	6744.0-6775.0	Defined in this paper.
O II	3716.3-3738.3	3696.3-3716.3	3738.3-3758.3	Tran et al. (2003), Fisher et al. (1998)
Hδ	4083.5-4122.3	4017.0-4057.0	4153.0-4193.0	Tran et al. (2003), Fisher et al. (1998)

Note. — The definition of indexes used in this work.

sidebands is used to determine the continuum in the line. This code computes the error in equivalent width from estimated noise in median flux. We used line strength index definition of O III, N II and Hα from Yan et al. (2006), Hβ from Fisher et al. (1998) and Tran et al. (2003) and we defined S II based on the proposed method. The definition of these indexes are in table 1.12. We could measure line ratios for 13 of all 24 μm cluster galaxies and 27 of all 24 μm field galaxies for [O III]/Hβ versus [N II]/Hα diagram. Also, [O III]/Hβ versus [S II]/Hα diagram has ten 24 μm cluster galaxies and twenty six 24 μm field galaxies. All EW measurements are presented in table 1.13 and table 1.14. A list of all galaxies flagged by BPT diagrams are presented in table 1.3 through table 1.11 and also a summary of our BPT classification is presented in table 1.15.

Table 1.13. Spectroscopic Catalog of 24 μm Cluster Galaxies for BPT Classification

ID[a]	EW(O III) ($\AA$)	EW(Hβ) ($\AA$)	EW(N II) ($\AA$)	EW(Hα) ($\AA$)	EW(S II) ($\AA$)	Log[O III/Hβ] [b]	Log[N II/Hα] [b]	Log[S II/Hα] [b]
17	-129.66 ± 4.41	-5.20 ± 5.06	-12.10 ± 16.67	-3.24 ± 16.67	-116.79 ± 10.78	1.40 ± 0.42	0.57 ± 2.31	1.56 ± 0.04
21	-30.32 ± 2.12	-5.50 ± 2.43	-1.10 ± 4.44	-83.74 ± 4.44	-	0.74 ± 0.19	-1.88 ± 1.75	-
23	-4.75 ± 1.41	-3.69 ± 2.02	-5.65 ± 3.78	-13.05 ± 3.78	-5.49 ± 4.55	0.11 ± 0.27	-0.36 ± 0.32	-0.38 ± 0.47
26	-2.69 ± 1.91	-7.42 ± 3.22	-21.59 ± 3.22	-70.52 ± 3.22	-7.52 ± 10.95	-0.44 ± 0.36	-0.51 ± 0.07	-0.97 ± 0.83
27	-13.79 ± 1.56	-15.40 ± 3.00	-47.59 ± 5.02	-115.21 ± 5.02	-24.51 ± 5.06	-0.05 ± 0.10	-0.38 ± 0.05	-0.67 ± 0.19
53	-15.49 ± 0.40	-7.98 ± 0.81	-13.96 ± 1.95	-71.85 ± 1.95	-24.08 ± 1.97	0.29 ± 0.05	-0.71 ± 0.06	-0.47 ± 0.04
54	-15.81 ± 0.50	-5.91 ± 0.82	-8.18 ± 1.09	-48.33 ± 1.09	-14.04 ± 1.71	0.43 ± 0.06	-0.77 ± 0.06	-0.54 ± 0.05
58	-14.04 ± 0.25	-10.97 ± 0.41	-19.47 ± 1.69	-78.45 ± 1.69	-26.48 ± 1.62	0.11 ± 0.02	-0.61 ± 0.04	-0.47 ± 0.03
75	-94.86 ± 4.68	-31.49 ± 0.67	-68.83 ± 0.39	-108.52 ± 0.39	-22.62 ± 1.33	0.48 ± 0.02	-0.20 ± 0.00	-0.68 ± 0.03
76	-6.24 ± 0.51	-3.03 ± 0.96	-10.89 ± 1.04	-40.51 ± 1.04	-22.07 ± 2.59	0.31 ± 0.14	-0.57 ± 0.04	-0.26 ± 0.05
103	-5.56 ± 2.09	-3.14 ± 3.23	-8.12 ± 3.90	-39.47 ± 3.90	-	0.25 ± 0.48	-0.69 ± 0.21	-
106	-6.78 ± 2.12	-11.79 ± 4.19	-54.74 ± 7.02	-137.54 ± 7.02	-8.58 ± 7.76	-0.24 ± 0.21	-0.40 ± 0.06	-1.20 ± 2.30
116	-11.20 ± 1.72	-12.92 ± 2.12	-20.67 ± 5.64	-94.59 ± 5.64	-	-0.06 ± 0.10	-0.66 ± 0.12	-

Table 1.13—Continued

ID[a]	Class 1 [c]	Class 2 [d]
17	AGN	LINER
21	Star forming	-
23	Composite	Star forming
26	Star forming	Star forming
27	Composite	Star forming
53	Star forming	Star forming
54	Star forming	Star forming
58	Star forming	Star forming
75	AGN	Star forming
76	Star forming	Seyfert
103	Star forming	-
106	Star forming	Star forming
116	Star forming	-

[a]As for Tables 1.3 through 1.11.

[b]Equivalent width line ratios

[c]Based on [O III]/Hβ versus [N II]/Hα BPT diagram, we classified the galaxies into AGN, Composite and Star forming.

[d]Based on [O III]/Hβ versus [S II]/Hα BPT diagram, we classified the galaxies into Star forming, Seyfert and LINER

Note. — . This Catalog is just for the identified 24 μm Cluster Galaxies in the sample. For the galaxies with IDs 21, 103 and 116 we were unable to measure EW(S II) so they are not classified as Spectral type 2.

Table 1.14. As for table 1.13, but for 24 μm Field Galaxies

ID[a]	EW(O III) (Å)	EW(Hβ) (Å)	EW(N II) (Å)	EW(Hα) (Å)	EW(S II) (Å)	Log[O III/Hβ]	Log[N II/Hα]	Log[S II/Hα]
9	-40.92 ± 1.74	-9.32 ± 2.74	-10.06 ± 3.83	-88.17 ± 3.83	-10.90 ± 6.96	0.64 ± 0.13	-0.94 ± 0.17	-0.91 ± 0.31
10	-1.50 ± 0.71	-1.73 ± 1.38	-7.43 ± 1.11	-17.94 ± 1.11	-0.51 ± 1.19	-0.06 ± 0.40	-0.38 ± 0.07	-1.55 ± 13.81
11	-22.44 ± 2.40	-8.21 ± 1.39	-22.44 ± 2.40	-53.64 ± 2.40	-24.22 ± 2.17	0.44 ± 0.09	-0.38 ± 0.05	-0.35 ± 0.06
12	-28.52 ± 1.97	-10.33 ± 1.75	-28.52 ± 1.97	-68.82 ± 1.97	-6.98 ± 1.90	0.44 ± 0.08	-0.38 ± 0.03	-0.99 ± 0.51
13	-59.42 ± 7.92	-11.67 ± 3.39	-59.42 ± 7.92	-139.64 ± 7.92	-40.04 ± 8.20	0.71 ± 0.14	-0.37 ± 0.06	-0.54 ± 0.16
30	-3.39 ± 1.38	-3.35 ± 1.75	-7.23 ± 3.78	-39.54 ± 3.78	-8.44 ± 5.38	0.01 ± 0.29	-0.74 ± 0.23	-0.67 ± 0.32
32	-24.99 ± 4.95	-4.72 ± 3.12	-24.99 ± 4.95	-60.91 ± 4.95	-21.31 ± 7.85	0.72 ± 0.30	-0.39 ± 0.09	-0.46 ± 0.20
33	-11.81 ± 3.54	-14.69 ± 3.56	-11.81 ± 3.54	-46.60 ± 3.54	-5.94 ± 4.49	-0.09 ± 0.17	-0.60 ± 0.13	-0.89 ± 0.61
34	-4.79 ± 3.96	-12.73 ± 3.10	-4.79 ± 3.96	-72.81 ± 3.96	-19.09 ± 6.43	-0.42 ± 0.37	-1.18 ± 0.36	-0.58 ± 0.15
39	-13.09 ± 2.98	-9.19 ± 3.35	-13.09 ± 2.98	-77.33 ± 2.98	-7.80 ± 3.03	0.15 ± 0.19	-0.77 ± 0.10	-1.00 ± 0.33
40	-17.59 ± 3.03	-2.19 ± 1.48	-17.59 ± 3.03	-103.46 ± 3.03	-	0.90 ± 0.30	-0.77 ± 0.08	-
47	-8.95 ± 2.60	-4.57 ± 2.73	-8.95 ± 2.60	-20.74 ± 2.60	-9.02 ± 4.45	0.29 ± 0.29	-0.36 ± 0.14	-0.36 ± 0.25
66	-44.12 ± 0.59	-25.53 ± 1.60	-43.20 ± 1.80	-175.60 ± 1.80	-56.46 ± 1.46	0.24 ± 0.03	-0.61 ± 0.02	-0.49 ± 0.02
68	-78.66 ± 3.06	-10.22 ± 3.28	-0.29 ± 8.32	-3.47 ± 8.32	-28.09 ± 10.02	0.89 ± 0.14	-1.08 ± 12.50	0.91 ± 0.15
82	-14.48 ± 1.64	-4.28 ± 0.97	-14.48 ± 1.64	-33.17 ± 1.64	-12.49 ± 1.82	0.53 ± 0.11	-0.36 ± 0.05	-0.42 ± 0.09
83	-62.92 ± 3.10	-16.15 ± 1.99	-62.92 ± 3.10	-85.82 ± 3.10	-30.00 ± 2.70	0.59 ± 0.06	-0.13 ± 0.03	-0.46 ± 0.10
84	-89.62 ± 7.20	-92.13 ± 8.12	-89.62 ± 7.20	-459.61 ± 7.20	-11.43 ± 5.52	-0.01 ± 0.05	-0.71 ± 0.04	-1.60 ± 2.16
94	-13.95 ± 2.28	-8.87 ± 3.46	-13.95 ± 2.28	-48.86 ± 2.28	-16.06 ± 3.35	0.20 ± 0.18	-0.54 ± 0.07	-0.48 ± 0.11
95	-2.12 ± 1.79	-2.58 ± 2.34	-2.12 ± 1.79	-35.35 ± 1.79	-12.57 ± 1.86	-0.09 ± 0.54	-1.22 ± 0.37	-0.45 ± 0.07
96	-19.74 ± 6.00	-12.41 ± 4.11	-19.74 ± 6.00	-56.71 ± 6.00	-16.48 ± 3.96	0.20 ± 0.20	-0.46 ± 0.14	-0.54 ± 0.22
98	-29.63 ± 12.61	-9.20 ± 2.29	-29.63 ± 12.61	-120.07 ± 12.61	-62.65 ± 16.50	0.51 ± 0.21	-0.61 ± 0.19	-0.28 ± 0.12
100	-4.38 ± 0.59	-0.33 ± 0.44	-4.38 ± 0.59	-30.78 ± 0.59	-12.41 ± 0.77	1.12 ± 0.58	-0.85 ± 0.06	-0.39 ± 0.03

Table 1.14—Continued

ID[a]	EW(O III) (Å)	EW(Hβ) (Å)	EW(N II) (Å)	EW(Hα) (Å)	EW(S II) (Å)	Log[O III/Hβ]	Log[N II/Hα]	Log[S II/Hα]
112	-7.93 ± 1.37	-4.24 ± 3.40	-7.93 ± 1.37	-19.92 ± 1.37	-7.96 ± 1.84	0.27 ± 0.36	-0.40 ± 0.08	-0.40 ± 0.12
113	-23.70 ± 2.39	-10.72 ± 2.21	-23.70 ± 2.39	-65.40 ± 2.39	-29.02 ± 2.66	0.34 ± 0.10	-0.44 ± 0.05	-0.35 ± 0.05
126	-29.05 ± 0.57	-69.74 ± 3.08	-29.05 ± 0.57	-359.27 ± 0.57	-70.52 ± 1.09	-0.38 ± 0.02	-1.09 ± 0.01	-0.71 ± 0.01
130	-4.66 ± 2.99	-7.45 ± 3.00	-4.66 ± 2.99	-45.82 ± 2.99	-9.40 ± 3.93	-0.20 ± 0.33	-0.99 ± 0.28	-0.69 ± 0.19
135	-3.14 ± 5.08	-14.80 ± 5.72	-3.14 ± 5.08	-32.50 ± 5.08	-6.16 ± 5.70	-0.67 ± 0.72	-1.01 ± 0.71	-0.72 ± 0.44

ID[a]	Class 1 [b]	Class 2 [c]
9	Star forming	Star forming
10	Composite	Star forming
11	Composite	Seyfert
12	Composite	Star forming
13	AGN	Seyfert
30	Star forming	Star forming
32	AGN	Seyfert
33	Star forming	Star forming
34	Star forming	Star forming
39	Star forming	Star forming
40	AGN	-
47	Composite	Seyfert
66	Star forming	Star forming
68	AGN	LINER
82	AGN	Seyfert
83	AGN	Seyfert

Table 1.14—Continued

ID[a]	Class 1 [b]	Class 2 [c]
84	Star forming	Star forming
94	Star forming	Star forming
95	Star forming	Star forming
96	Composite	Star forming
98	Composite	Seyfert
100	AGN	Seyfert
112	Composite	Star forming
113	Composite	Seyfert
126	Star forming	Star forming
130	Star forming	Star forming
135	Star forming	Star forming

[a]As for Table 1.3 through 1.11.

[b]Based on [O III]/Hβ versus [N II]/Hα BPT diagram, we classified the galaxies into AGN, Composite and Star forming.

[c]Based on [O III]/Hβ versus [S II]/Hα BPT diagram, we classified the galaxies into Star forming, Seyfert and LINER

Note. — . This Catalog is just for the identified 24 μm Field Galaxies in the sample. For the galaxy with IDs 40, we were unable to measure EW(S II), so it is not classified as Spectral type 2.

Table 1.15. Summary of BPT Classification of the 24 μm Galaxies in Clusters and in the Field

Environment	N_{total}	N_{24}	N_{class1}	N_{class2}	Class 1			Class 2		
					Star forming	Composite	AGN	Star forming	Seyfert	Liner
Clusters	68	44	13	10	9	2	2	8	1	1
Field	67	61	27	26	12	8	7	16	9	1

Note. — . Column 2 is the total number of the galaxies and column 3 is the number of 24 μm detected galaxies. Column 4 and 5 are the total number of the 24 μm detected galaxies that were classified based on two BPT diagrams. Class 1 is [O III]/Hβ versus [N II]/Hα BPT diagram and Class 2 is [O III]/Hβ versus [S II]/Hα BPT diagram. Column 6 to 11 are the numbers of classified galaxies. (See table 1.13 and table 1.14)

Based on these BPT plots we could find two AGNs, one LINER and one Seyfert galaxy in the clusters and seven AGNs, nine Seyferts and one LINER in the field. Also, from the broad lines in the spectrum of some of the sources, we could identifiy them as QSO, for example, the field galaxy FLS 18-3-5 (SDSS J171437.41+595647.9).

1.4.2.2 MORPHS Classification

The other classification we used, was proposed by MORPHS collaboration (Dressler et al., 1999). This classification is based on the equivalent widths of the [O II] emission line and the Hδ absorption line. Both of them are the best indicators of ongoing and recent star formation. Therefore we can classify our sample based on the star formation activity. We used the *IDL* code by Ricardo Demarco to measure the EWs of the 24 μm cluster galaxies. We used the index definition of Hδ and [O II] from Fisher et al. (1998) and Tran et al. (2003) (table 1.12). Based on the this spectral classification we classified these galaxies into Passive (k), Post-starburst [k+a and a+k] and Active [e(c), e(a), e(b) and e(n)] galaxies (table 1.16). The classes we used in this classification are (Poggianti et al. (2009) and Dressler et al. (2009a)):

k class: These are passively evolving galaxies that show no spectral sign of ongoing or recent star formation during the past 1-1.5 Gyr. They are characterized by no [O II] emission line and EW(Hδ) $<$ 3 Å . Their spectrum is similar to K type stars. For this reason we to them as "k galaxies".

Table 1.16. Adopted MORPHS Spectral Classification

Class	EW(O II) ($\AA$)	EW(Hδ) ($\AA$)	Type
k	< 5	< 3	Passive
k+a	< 5	3-8	Poststarburst/Moderate Balmer Absorption
a+k	< 5	> 8	Poststarburst/Strong Balmer Absorption
e(c)	5-40	< 4	Quiescent Star forming
e(a)	> 5	> 4	Dusty Starburst
e(b)	> 40	...	Starburst
e(n)	...	...	AGN from broad lines or BPT diagrams

Note. — Adopted MORPHS Spectral Classification used in this paper. (Dressler et al., 1999)

k+a / a+k classes: These are post-starforming and post-starburst galaxies with their star formation activity terminated sometime between 5×10^7 and 1.5×10^9 years before observation. They show no significant [O II] emission (EW(O II) < 5 Å) and for k+a galaxies 3 Å $<$ EW(Hδ) < 8 Å and for a+k galaxies EW(Hδ) > 8 Å . The names "k+a" or "a+k" come from the fact that their spectra are a mix of K type and A type stars.

e(c) class: They are quiescent star forming galaxies with moderate O II emission line ($5 <$ EW(O II) < 40 Å) and EW(Hδ) < 4 Å). Their spectra are similar to type Sa and type Sd spiral galaxies and have a continuous star formation history without any sudden variation.

e(a) class: They are ongoing dusty starburst galaxies with weak optical emissions which have EW(O II) > 5 Å and EW(Hδ) > 4 Å . There is a hypothesis that these active starbursts feed the post-starburst galaxies and are their progenitors. The active star formation of these galaxies has been obscured by heavy dust and for this reason their optical observations show insufficient emissions as starburst galaxies (Dressler et al., 2009a).

e(b) class: They are strong starbursts defined to have a strong O II emission line (EW(O II) > 40 Å) and are generally low mass and very late type galaxies (Poggianti et al., 1999) .

e(n) class: These are AGNs which can be identified from broad lines in their spectra or from BPT diagrams.

A list of all EW measurements are presented in table 1.17 and table 1.18. A summary of MORPHS classification is presented in table 1.19.

Most of the active galaxies are e(a)s and e(c)s that demonstrate the dusty star formation activity of the 24 μm sources. Dusty starbursts, e(a), are the majority of the 24 μm sources in the clusters and in the field. For those galaxies that we could not measure EW(O II) or EW(Hδ) in this classification, we classify them as Active star forming or passive based on their spectra. Based on our two different classifications, the population of cluster galaxies are 59/23/7/11 % Star forming/Passive/Post-Starburst/AGN and 57/8/2/33 % in the field.

Table 1.17. Spectroscopic Catalog of 24 μm Cluster Galaxies for MORPHS Classification

ID[a]	EW(O II) ($\mathring{A}$)	EW(Hδ) ($\mathring{A}$)	Spectral type
17	-5.48 ± 8.39	12.26 ± 9.86	e(a)
18	-15.53 ± 4.30	11.52 ± 2.24	e(a)
19	-15.95 ± 6.70	7.84 ± 2.54	e(a)
20	-19.33 ± 6.31	4.53 ± 5.35	e(a)
21	-69.8 ± 2.8	3.84 ± 1.92	e(b)
22	-8.06 ± 2.59	2.46 ± 1.50	e(c)
23	-9.21 ± 5.49	5.97 ± 2.94	e(a)
24	-12.91 ± 7.70	0.39 ± 2.55	e(c)
25	6.01 ± 5.96	3.40 ± 6.88	k+a
26	-27.24 ± 4.95	6.14 ± 2.57	e(a)
27	-26.32 ± 4.39	6.53 ± 2.57	e(a)
42	-4.19 ± 2.43	-1.03 ± 2.54	k
51	-7.83 ± 1.01	2.87 ± 3.30	e(c)
52	-17.12 ± 3.94	3.64 ± 3.16	e(c)
53	-42.86 ± 1.18	6.22 ± 0.66	e(b)
54	-39.97 ± 1.27	5.61 ± 0.78	e(a)
56	-1.53 ± 2.89	5.01 ± 1.30	k+a
57	-16.79 ± 8.81	6.34 ± 2.94	e(a)
58	-37.05 ± 0.63	3.95 ± 0.52	e(a)
73	1.43 ± 1.64	-0.57 ± 1.00	k
77	< 5	< 3	k
86	-2.53 ± 1.91	12.31 ± 1.80	a+k
87	-32.7 ± 2.85	0.91 ± 2.50	e(c)
102	-9.42 ± 6.33	-4.05 ± 6.11	e(c)
103	-25.29 ± 6.22	10.08 ± 4.28	e(a)

Table 1.17—Continued

ID[a]	EW(O II) ($\mathring{A}$)	EW(Hδ) ($\mathring{A}$)	Spectral type
105	-10.54 ± 8.03	2.74 ± 5.36	e(c)
106	-47.31 ± 12.13	7.91 ± 6.14	e(b)
116	-10.36 ± 3.81	4.48 ± 2.02	e(a)

[a]same as Tables 1.3 through 1.11.

Note. — . This Catalog is just for the identified 24 μm Cluster Galaxies in the sample. Identified AGNs *e(n)* from broad lines were excluded from this table.

Table 1.18. As for Table 1.17, but for 24 μm Field Galaxies

ID[a]	EW(O II) ($\AA$)	EW(Hδ) ($\AA$)	Spectral type
8	-13.3 ± 4.4	7.80 ± 4.24	e(a)
9	-62.35 ± 3.26	-0.04 ± 3.26	e(b)
10	-12.56 ± 2.59	1.41 ± 1.76	e(c)
11	-25.39 ± 3.95	5.41 ± 2.89	e(a)
12	-5.15 ± 1.39	3.57 ± 1.77	e(c)
13	-51.57 ± 10.91	2.13 ± 4.16	e(b)
14	-151.64 ± 8.13	7.74 ± 6.95	e(b)
15	-51.55 ± 4.08	1.57 ± 4.27	e(b)
16	-17.59 ± 4.57	4.22 ± 3.39	e(c)
30	-13.3 ± 4.4	7.80 ± 4.24	e(a)
33	-20.51 ± 5.24	1.17 ± 5.01	e(c)
34	-34.69 ± 4.00	14.22 ± 2.87	e(a)
35	-25.01 ± 6.27	-0.71 ± 5.99	e(a)
37	-8.55 ± 3.75	3.84 ± 2.86	e(c)
38	2.86 ± 7.59	5.43 ± 2.15	k+a
39	-61.82 ± 4.33	4.41 ± 2.44	e(b)
40	-37.83 ± 1.29	3.09 ± 1.03	e(c)
41	-40.54 ± 11.01	-0.56 ± 4.04	e(b)
48	-22.80 ± 3.47	7.63 ± 2.83	e(a)
49	-10.04 ± 1.91	6.23 ± 1.73	e(a)
50	-13.42 ± 8.76	8.30 ± 4.58	e(a)
59	-32.87 ± 3.18	6.22 ± 3.12	e(a)
60	-2.75 ± 1.41	-0.69 ± 2.21	k
61	-32.90 ± 1.19	6.59 ± 2.90	e(a)
63	-30.29 ± 2.26	6.58 ± 2.01	e(a)

Table 1.18—Continued

ID[a]	EW(O II) ($\AA$)	EW(Hδ) ($\AA$)	Spectral type
64	-36.05 ± 9.94	16.82 ± 8.94	e(a)
65	-5.50 ± 2.17	-1.58 ± 1.79	e(c)
82	-8.39 ± 0.55	3.24 ± 0.64	e(c)
83	-11.72 ± 2.22	7.72 ± 2.50	e(a)
95	-13.82 ± 2.62	2.22 ± 2.50	e(c)
96	-30.95 ± 2.32	10.50 ± 1.97	e(a)
97	-71.39 ± 5.33	13.32 ± 5.70	e(a)
99	-1.81 ± 1.53	3.08 ± 2.46	k
100	-28.40 ± 1.29	7.34 ± 0.77	e(a)
101	-64.72 ± 5.78	-0.58 ± 5.03	e(b)
113	-30.57 ± 2.71	10.84 ± 2.15	e(a)
127	-15.57 ± 3.88	-2.32 ± 2.99	e(c)
130	-14.99 ± 3.85	1.04 ± 4.21	e(c)
132	-0.06 ± 1.26	3.02 ± 2.59	k
133	-10.22 ± 3.33	1.89 ± 2.40	e(c)
134	-52.78 ± 11.66	2.81 ± 5.47	e(b)
135	-123.10 ± 0.00	37.76 ± 28.21	e(b)

[a]As for Tables 1.3 through 1.11.

Note. — . This Catalog is just for the identified 24 μm Field Galaxies in the sample. Identified AGNs *e(n)* from broad lines were excluded from this table.

Table 1.19. Summary of MORPHS Classification of the 24 μm Galaxies in Clusters and in the Field

Environment	N_{total}	N_{24}	N_{class}	k	k+a	a+k	e(c)	e(a)	e(b)	e(n)
Clusters	68	44	29	3	2	1	7	12	3	1
Field	67	61	46	3	1	0	11	17	9	5

Note. — . Column 2 is the total number of the galaxies, column 3 is the number of 24 μm detected galaxies and Column 4 is the total number of the 24 μm detected galaxies that were classified. Column 5 to 11 are the numbers of classified galaxies.(See table 1.17 and table 1.18)

This classification has some benefits when compared to BPT classification. With the presence of only two features (O II and Hδ), we can classify nearly all of the sample based on their star forming activities, but in BPT classification, four emission lines have to be present and measurable together in each spectrum. The reasons, such as sky lines, atmospheric absorptions, bad pixels, cosmic rays, and noise, destroy the features in the spectrum and make it difficult to analyze them. Also, BPT classification is restricted to $z < \sim 0.32$ because of [S II] 6717,6732 emission lines but MORPHS classification covers the redshift range of our sample.

1.4.3 SFR(Hα) : Optical Hα Star Formation Rate

Based on our classifications, we could identify AGNs in our sample and excluded them from active star forming galaxies. So far, all of the analyses we did have revealed that the majority of the 24 μm active star forming galaxies in clusters and in the field are dusty starbursts e(a). Based on a hypothesis, e(a) galaxies seem to be the progenitors of the post-starburst galaxies and feed them (Dressler et al., 2009a, 1999). If this is true, they play the most important role in the transformation of star forming galaxies into passive galaxies in clusters.

The Hydrogen Balmer line Hα 6563 is currently the most reliable tracer of star formation (Kewley et al., 2004) and for the redshift range of our data set it is the best choice. We take the relation of Kennicutt (1992):

$$SFR(H\alpha) = 7.9 \times 10^{-42} L(H\alpha) E(H\alpha) \tag{1.8}$$

with E(Hα) = 1 mag and

$$L(H\alpha) = Flux(H\alpha) \times 4\pi D_L^2 \tag{1.9}$$

$$Flux(H\alpha) = F_c \times EW(H\alpha) \tag{1.10}$$

where F_c is the continuum flux at the position of the Hα feature. The results are presented in section 1.5.4. Our estimated SFR(Hα)s are "observed SFR(Hα)s" because we derived them with no extinction correction. The uncertainty in SFR(Hα) is estimated from the uncertainty in equivalent width (see section 1.4.2.1) and Kennicutt (1992) SFR relation.

1.4.4 SFR(IR): IR Star Formation Rate

Although most of the studies about the star formation in clusters rely on Optical and UV tracers, they suffer from dust. Dust plays a very important role in the star formation history of the universe. Spitzer space telescope opened a new eye to our dust-obscured universe and revealed many new facts, such as strong dust-obscured star formation activities of the galaxies that were hidden and underestimated up to 90 %. In order to compare the Optical SFR with IR SFR we use Dale & Helou (2002) models to estimate total IR luminosity L_{IR} (3-1100 μm) from observed 24 μm fluxes of the galaxies. We measure observed 24 μm flux in μJy and convert it to erg s^{-1} cm^{-2} by c/23.8μm which is the central frequency of the 24 μm bandpass. Then we multiply this flux by $4\pi {D_L}^2$ to derive the observed 24 μm luminosity L^*_{24}. This observed 24 μm luminosity L^*_{24} corresponds to lower wavelengths which are redshifted. Using Dale & Helou (2002) templates and relations, we scale L^*_{24} based on the spectroscopic redshift of the galaxy to estimate L_{IR} as below:

$$L_{IR} = 1.559 \times \nu L_\nu(24\mu m) + 0.7686 \times \nu L_\nu(70\mu m) + 1.347 \times \nu L_\nu(160\mu m) \quad (1.11)$$

with factoring $\nu L_\nu(24\mu m)$, we have:

$$L_{IR} = \nu L_\nu(24\mu m) \times (1.559 + \frac{0.7686 \times \nu L_\nu(70\mu m)}{\nu L_\nu(24\mu m)} + \frac{1.347 \times \nu L_\nu(160\mu m)}{\nu L_\nu(24\mu m)}) \quad (1.12)$$

Since $\nu L_\nu(24\mu m)$ is the rest-frame 24μm luminosity $L_{rest}(24\mu m)$, total IR luminosity L_{IR} as a function of $L_{rest}(24\mu m)$ and relative νf_ν fractions is:

$$L_{IR} = L_{rest}(24\mu m) \times (1.559 + \frac{0.7686 \times \nu f_\nu(70\mu m)}{\nu f_\nu(24\mu m)} + \frac{1.347 \times \nu f_\nu(160\mu m)}{\nu f_\nu(24\mu m)}) \quad (1.13)$$

The relative νf_ν fractions in the above relation can be calculated by Dale & Helou (2002) models and tables, which are publicly available, and $24\mu m$ luminosity in the rest-frame of the galaxy $L_{rest}(24\mu m)$ is calculated by K-correction:

$$L_{rest}(24\mu m) = \frac{L^*_{24}}{K(z)} \tag{1.14}$$

$$K(z) = \frac{f_\nu}{f_{24}}(1+z) \tag{1.15}$$

We take the relation of Kennicutt (1998) :

$$SFR(IR) = 4.5 \times 10^{-44} L_{IR} \tag{1.16}$$

to derive SFR(IR) for star forming galaxies which have been identified by our classifications. We should note that there is a small difference between L_{IR} (3-1100 μm) defined by Dale & Helou (2002) and L_{IR} (3-1000 μm) by Kennicutt (1998), but this impacts the inferred SFR by less than 5 % (Finn et al., 2010). The uncertainty in SFR(IR) is estimated from the uncertainty in flux and Kennicutt (1998) SFR relation. The results are presented in section 1.5.4.

1.4.5 Stellar Mass Estimation

To estimate galaxy stellar masses, we match our sample with SDSS DR9 to pull out g' and r' magnitudes. Since 24 μm star forming galaxies are bright, they match very well and there is no misidentification problem.

K-corrections in g' band are calculated using the IDL code by Chilingarian et al. (2010). This code calculates K-correction as a function of redshift and observed color for galaxies at $z < 0.5$ except AGNs. Rest frame flux in g' band, $F_g(0)$ is derived as:

$$K_g(z, g-r) = -2.5log(\frac{F_g(0)}{F_g(z)}) \tag{1.17}$$

where K_g is the K-correction and $F_g(z)$ is the observed flux in g' band. Luminosity L_g is calculated by:

$$L_g = F_g(0) \times 4\pi D_L^2 \tag{1.18}$$

We estimate the stellar mass using the relation between mass-to-light ratio and rest frame (g'-r') color from Bell (2003):

$$log(\frac{M}{L_g}) = -0.499 + 1.519(g' - r') \tag{1.19}$$

The estimated masses in this paper are based on 'diet Salpeter' IMF (Bell, 2003). Just for comparison, we modify the above relation for a Kroupa IMF by a modification from Bell (2003) and estimate the mass for a sample of randomly selected galaxies from the stellar mass catalog of Kauffmann et al. (2003b). This sample has been selected from this catalog by picking all the galaxies at $z > 0.25$ (about 250 galaxies) and 5500 randomly selected galaxies at $0.07 < z < 0.25$ that have rest-frame (g'-r') color < 1.75 which is the color limit of our Palomar sample of star forming galaxies. Figure 1.27 and Figure 1.28 show this comparison. In these figures, M_a is our estimated mass and M_k is the estimated mass from Kauffmann et al. (2003b) catalog. The relative-mass-change R is defined as below:

$$R = \frac{M_a - M_k}{M_k} \tag{1.20}$$

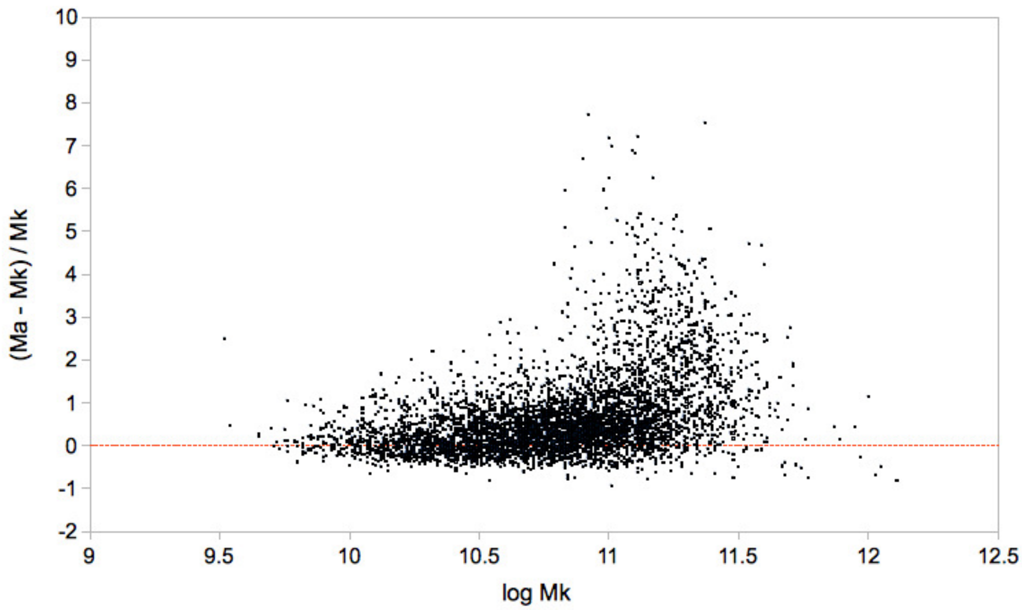

Figure 1.27 Stellar mass comparison. M_a is our estimated mass and M_k is the estimated mass from Kauffmann et al. (2003b).

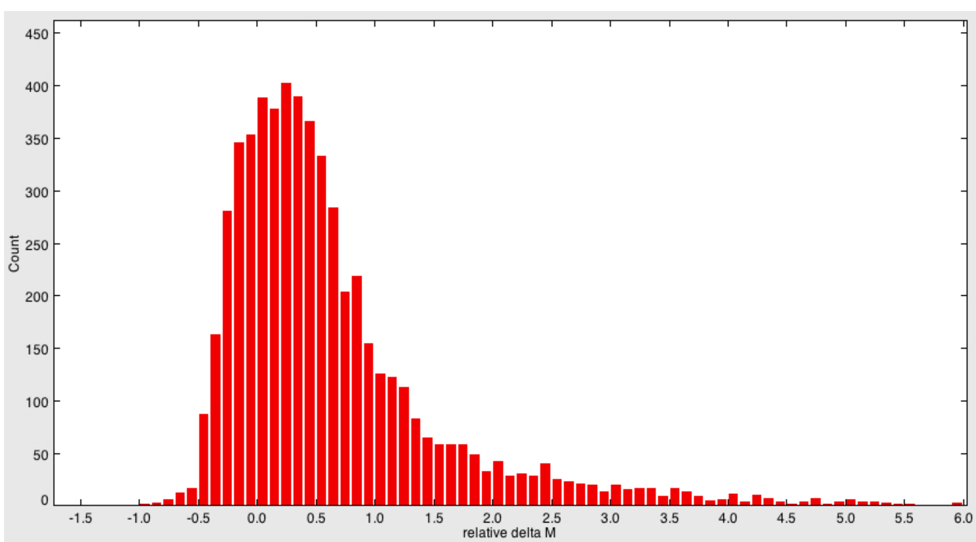

Figure 1.28 Relative-mass-change distribution. Horizontal axis of this plot is the vertical axis of previous figure.

In Figure 1.27 and Figure 1.28, about 90 % of the sample have relative-mass-change less than 0.75 which shows that our measured masses have an uncertainty of less than 0.25 dex with respect to Kauffmann et al. (2003b) estimations. Based on this comparison we can estimate an average uncertainty of 0.3 dex for our derived masses in our Palomar star forming sample.

1.4.6 Spectroscopic Completeness

To correct the measured properties of cluster members to total cluster galaxy population, we determine spectroscopic completeness. Since our sample is selected from red sequence bin on color-magnitude diagram and the variation of the color is small, we define the completeness as a function of magnitude (R or [3.6]) and distance (r). For each cluster, we bin all the galaxies in our photometric cluster catalog by magnitude and distance. The spectroscopic completeness function is defined from Muzzin et al. (2012) as below:

$$C_{spec}(mag, r) = \frac{N_{cluster,z}}{N_{gal}(N_{cluster,z}/(N_{field,z} + N_{cluster,z}))} \tag{1.21}$$

where $N_{cluster,z}$ is the total number of cluster members in that magnitude and distance bins with redshift, $N_{field,z}$ is the total number of field galaxies in that magnitude and distance bins with a spectroscopic redshift and N_{gal} is the total number of the galaxies with or without a redshift in that magnitude and distance bins. The computed completeness functions for SWIRE clusters are presented in Figure 1.29.

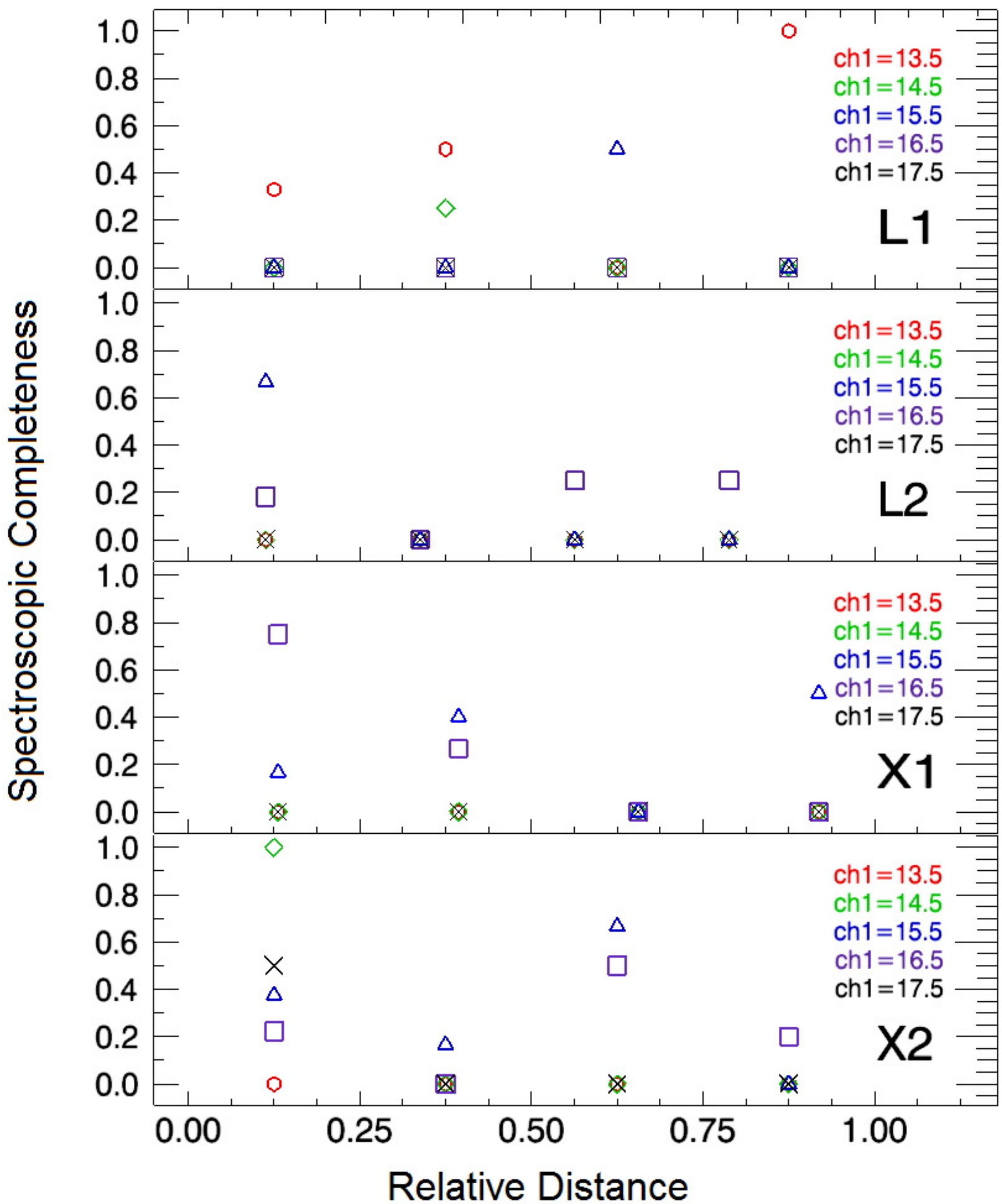

Figure 1.29 Spectroscopic completeness of cluster galaxies as a function of relative projected distance from the cluster center.

1.5 Results

1.5.1 Spectroscopic Confirmation of Nine Red-Sequence Selected Galaxy Clusters at $z < 0.5$ from SpARCS Survey

As we explained in Section 1.2 and 1.4.1, we spectroscopically confirmed nine galaxy clusters with enough members (n > 5) ($z = 0.125$, 0.247, 0.254, 0.253, 0.222 in FLS , $z = 0.288$, 0.353 in SWIRE-XMM and $z = 0.072$, 0.487 in SWIRE-Lockman) in SpARCS survey. The properties of these clusters are presented in table 1.1 and their catalogs are presented from table 1.3 to table 1.10. We find that FLS J172449+592122 is a system of two clusters about to merge. By considering this as two separate clusters we actually confirmed nine clusters. There are 68 cluster galaxies in total at $0.07 < z < 0.49$ and of these only 44 members are 24 μm sources. The spectra of the identified cluster galaxies are shown in Figure 1.1 through Figure 1.8 and the color-magnitude diagrams are presented in Figure 1.9 through Figure 1.16. The three-color composite images of the clusters are presented in Figure 1.17 through Figure 1.24.

1.5.2 Spectral types of 24 μm detected galaxies in Clusters and the Field

In this study, using BPT diagrams, we classify all of the 24 μm galaxies that the defined indexes can be measured for them, into AGNs (Seyfert/LINER), Composites and star forming galaxies. Figure 1.25 and Figure 1.26 show the BPT diagrams for the cluster and field galaxies. The fraction of identified AGNs in the field is higher with respect to the cluster galaxies. LINERs are very rare in both environments and the majority of the AGNs in the field were identified as Seyferts. The identified AGNs in these diagrams as well as those AGNs identified from broad lines, have been excluded from our star formation measurements.

Using MORPHS classification, we classify most of the galaxies into Active star forming [e(a), e(b) and e(c)], Post-starbursts [k+a and a+k] and Passive k galaxies (table 1.17, table 1.18 and table 1.19). The identified AGNs via broadlines in their spectra or BPT diagrams are labeled e(n). There are some galaxies that we could not measure EW(Hδ) or EW(O II) for them, but based on their spectra we classify them into Active or Passive galaxies.

We consider Composites as AGNs regardless of their MORPHS spectral types. Based on these classifications, we identified different populations in clusters (59/23/7/11 % Star forming/Passive/Post-Starburst/AGN) and in the field (57/8/2/33%), which may show the difference between evolutionary processes that govern in their environments but it is mainly biased by our galaxy selections in this sample. Note that we have selected red-sequence and 24 μm galaxies in the field of rich clusters based on their slit positions on the mask. The complexity of this selection makes the direct comparison of the cluster and field galaxies very difficult. Therefore, we compare the spectral types only in the environment they reside in. More than half of the galaxies in both environments (59/57% Cluster/Field) are active star forming galaxies that

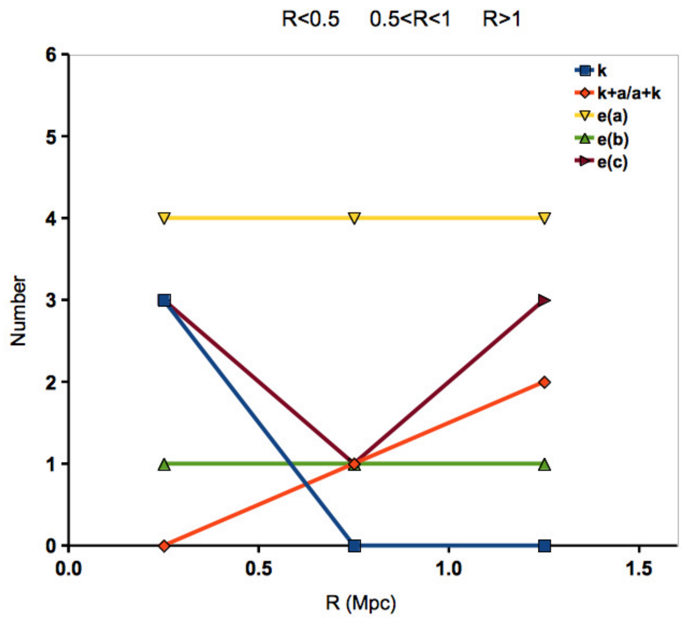

Figure 1.30 Positional abundance of spectral types in clusters.

are the majority of the 24 μm galaxies. Among these active galaxies, dusty starbursts e(a) and normal star forming galaxies e(c) are the majority of them. Also note that the majority of 24 μm galaxies are Dusty Starbursts e(a) (27/28% Cluster/Field, see table 1.19). The small fractions of passive galaxies (10/5%) are noticeable and shows the importance of mid-infrared data to study dusty star formation. We discuss passive 24 μm galaxies in discussion. Post-starburst galaxies are very rare in both environments at low redshifts $z <\sim 0.4$ and we could identify only three of them in the clusters and one in the field (7/2%).

Figure 1.30 presents positional abundance of the spectral types in galaxy clusters. All types of active star forming galaxies [e(a), e(b) and e(c)] are present every where in clusters regardless of their distance from the center (Dressler et al., 2009a).

1.5.3 Stacked Spectra

For comparing 24 μm star forming galaxies in clusters with those in the field, we stack the spectra to see if there is any difference. Stacking the spectra is performed based on the recipe in Muzzin et al. (2012). Each spectrum is normalized using the median flux in the range 4050Å - 4100Å rest-frame, which is the part of the spectrum that is redward of the 4000Å break and does not contain substantial absorption or emission lines. Then each galaxy is weighted by its completeness weight. Inasmuch as the rest-frame spectrum depends on the redshift of the galaxy, we only considered the spectra of those galaxies with a rest-frame spectrum span from 3600Å to 6800Å .

By stacking 22 spectra in clusters and 22 spectra in the field, the normalized and completeness corrected stacked spectra are produced and presented in Figure 1.31. In order to classify and compare these two stacked spectra, measured equivalent widths and line ratios are presented in table 1.20 and table 1.21. Both spectra look similar and tell us that star forming galaxies in these different environments do not show much difference at this range of redshift. Based on BPT classifications, both stacked spectra of cluster and field galaxies show a star forming nature. EW(Hδ) of the stacked spectrum in clusters is 4.47 ± 1.71 Å and in the field is 3.53 ± 1.77 Å . With these EW(Hδ) measurements which are around 4Å , we can not classify these two spectra into e(a) or e(c); therefore we classify them as a spectral type between dusty starburst and quiescent star forming galaxies (e(a),e(c)) (see table 1.21).

Table 1.20. Stacked Spectra of 24 μm Star forming Galaxies - BPT Classification

Environment	EW(O III)	EW(Hβ)	EW(N II)	EW(Hα)	EW(S II) ($\AA$)	Log[O III/Hβ]	Log[N II/Hα]	Log[S II/Hα]
Cluster	-4.32 ± 0.97	-2.09 ± 1.44	-10.53 ± 1.50	-35.49 ± 1.50	-10.10 ± 1.78	0.32 ± 0.31	-0.53 ± 0.06	-0.55 ± 0.08
Field	-7.13 ± 1.18	-3.16 ± 1.06	-7.95 ± 1.10	-29.53 ± 1.10	-7.33 ± 1.04	0.35 ± 0.16	-0.57 ± 0.06	-0.61 ± 0.06

Environment	Class 1 [a]	Class 2 [b]
Cluster	Star forming	Star forming
Field	Star forming	Star forming

[a]Based on [O III]/Hβ versus [N II]/Hα BPT diagram, we classified the galaxies into AGN, Composite and Star forming.

[b]Based on [O III]/Hβ versus [S II]/Hα BPT diagram, we classified the galaxies into Star forming, Seyfert and LINER

Note. — . Equivalent widths in $\AA$, line ratios and spectral types of the stacked spectra of 24 μm star forming galaxies in clusters and in the field are presented in this table.

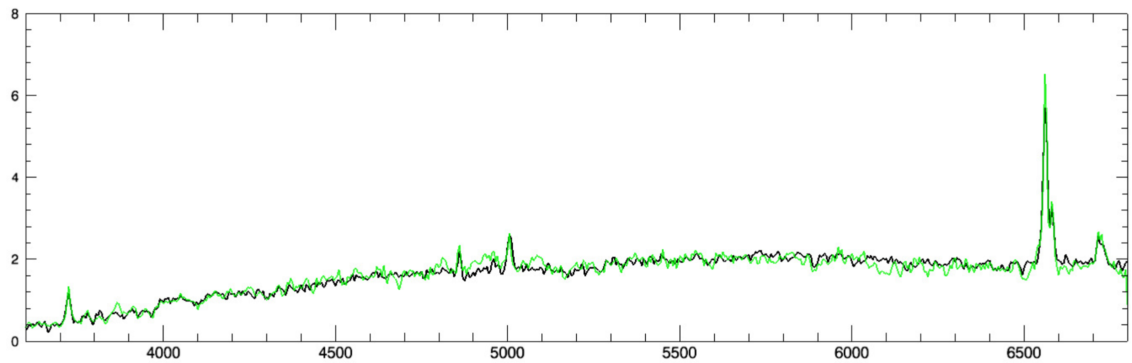

Figure 1.31 Normalized and completeness corrected stacked spectra of 24 μm star forming galaxies in clusters (green) and in the field (black) at $0.1 < z < 0.3$ (See table 1.20 and table 1.21). Each stacked spectrum is produced from the spectra of 22 galaxies. Stacked cluster and field spectra are very similar to each other. (See Section 1.4.6 and 1.5.3)

Table 1.21. Stacked Spectra of 24 μm Star forming Galaxies - MORPHS Classification

Environment	EW(O II) ($\AA$)	EW(Hδ) ($\AA$)	Spectral type
Cluster Galaxies	-17.72 ± 3.50	4.47 ± 1.71	e(a) , e(c)
Field Galaxies	-16.38 ±4.33	3.53 ± 1.77	e(a) , e(c)

Note. — . The stacked spectra of 24 μm star forming galaxies in clusters and in the field are classified in this table based on MORPHS classification.

1.5.4 Star Formation Rate and Stellar Mass of 24 μm galaxies in Clusters and the Field at $z <\sim 0.5$

The results of SFR(IR) and Stellar Mass M* estimations are presented in Figure 1.32. In this section we only analyze active star forming galaxies in order to understand the nature of pure star forming galaxies and compare them in different environments. Figure 1.32 shows that star forming galaxies in our sample are generally massive and there is an obvious correlation between SFR(IR) and stellar mass. Because of selection bias due to selection of cluster galaxies near the center of clusters, these selected galaxies are massive, spanning from 10^{10} to 10^{12} $M_{\odot}$. Both Field and cluster galaxies do not show much difference. Specific Star Formation Rate (SSFR) defined by SFR(IR)/M* as a function of stellar mass is presented in Figure 1.33 and shows a decline in SSFR as galaxy stellar mass increases. This correlation does not show much dependence on environment. We compare our SSFR estimations with empirical relation from Salim et al. (2007) that is shown by a solid line in Figure 1.33. This empirical linear relation (Salim et al., 2007) is only for identified pure star forming galaxies (with no AGN contribution) using the BPT diagrams.

Figure 1.34 shows the plot of observed SFR(Hα) versus redshift for these active star forming galaxies. Observed SFR(Hα) is derived from observed Hα luminosity $L_{H\alpha}$ with no extinction correction. Our estimations have been compared to the sample of Marleau et al. (2007) that is a spectroscopic survey of 24 μm galaxies, with flux

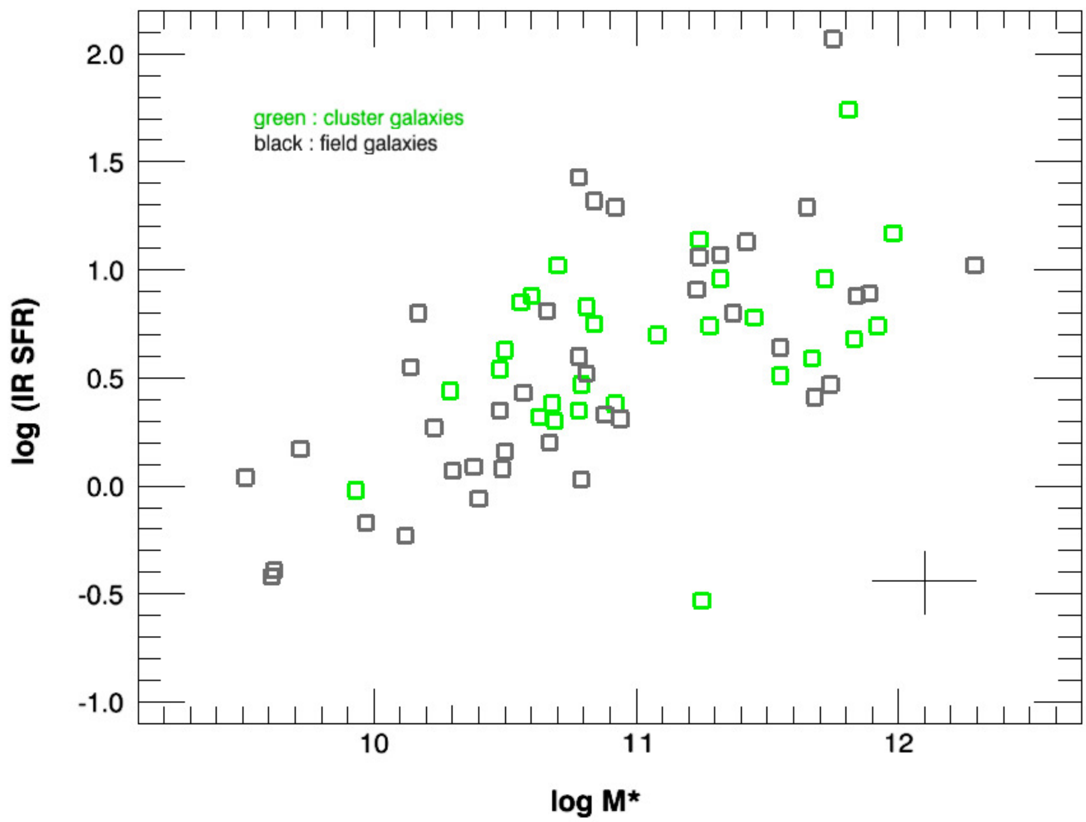

Figure 1.32 IR SFR versus Stellar Mass for 24 μm star forming galaxies. The green boxes are cluster galaxies and the black boxes are field galaxies. The cross in lower-right presents the maximum uncertainties in our estimations.

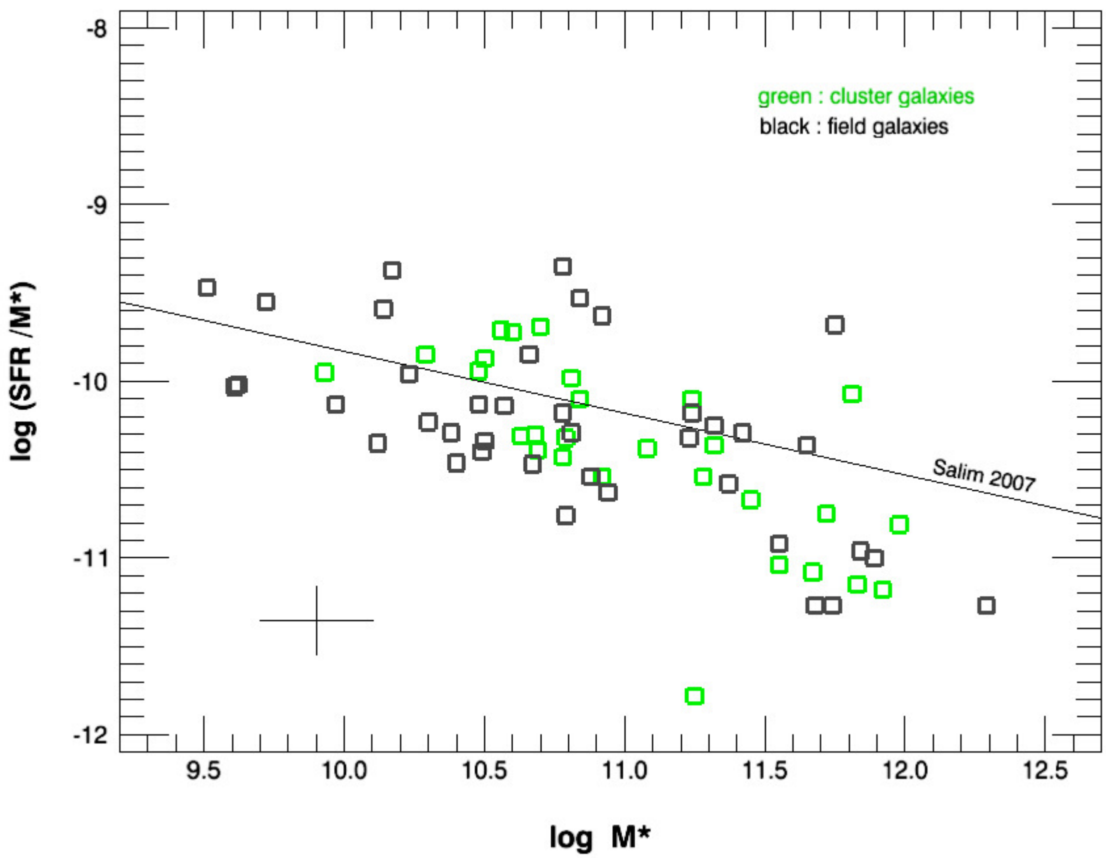

Figure 1.33 Specific SFR(IR) versus Stellar Mass for 24 μm star forming galaxies. The green boxes are cluster galaxies and the black boxes are field galaxies. The solid line is the empirical relation from Salim et al. (2007) for comparison. The cross in lower-left presents the maximum uncertainties in the estimations.

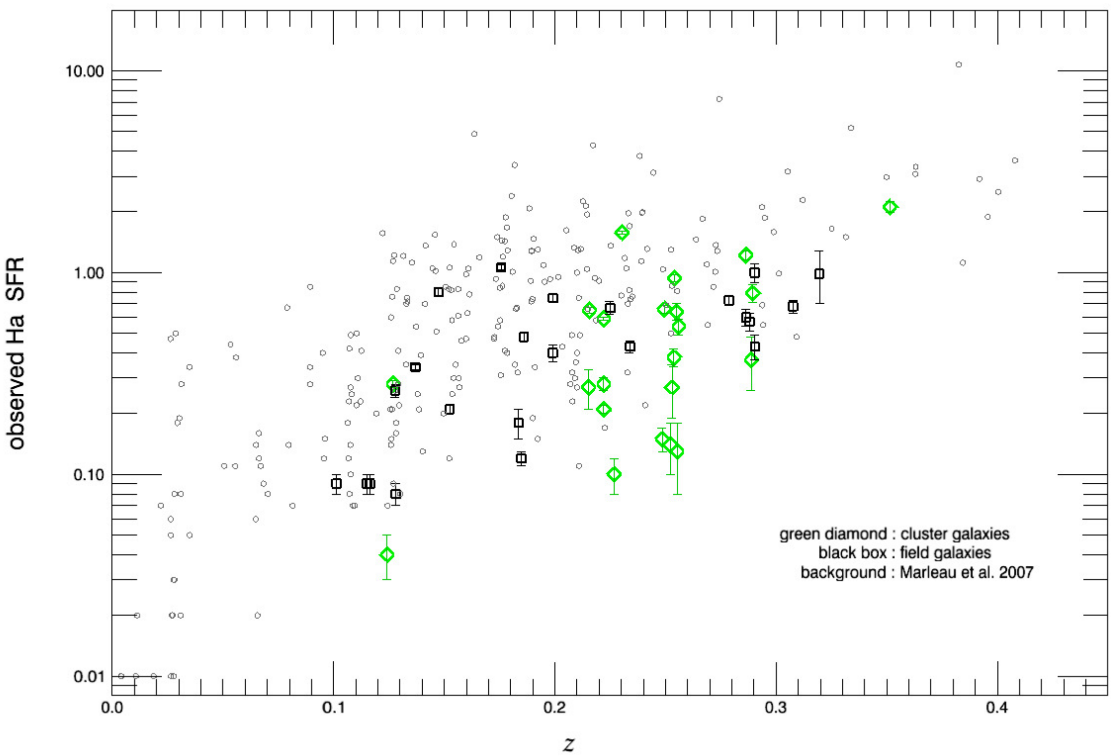

Figure 1.34 Observed SFR(Hα) versus redshift of active star forming galaxies. Observed SFR(Hα) was not corrected for extinction. AGNs, Post-starburst and Passive galaxies were excluded. Cluster galaxies are shown by green triangles and Field galaxies by black boxes. Background circles are data from Marleau et al. (2007) for comparison (See Section 1.5.4).

densities above 0.15 mJy, at redshifts $0 < z < 0.4$. As it is seen in Figure 1.34 our estimations are close to the data from Marleau et al. (2007), but some of the cluster galaxies in our sample show lower SFR(Hα)s that raises a question.

Infrared star formation rate SFR(IR) from 24 μm observation is very less affected by dust. Figure 1.35 shows the plot of estimated L_{IR} of the active star forming galaxies versus redshift and the results are compared to data from Kartaltepe et al. (2010). The two different populations do not show much difference in this plot. Data from Kartaltepe et al. (2010) are generally massive (10^{10}-10^{12} $M_{\odot}$) and bright objects. For this reason, in our comparison our objects are located in lower L_{IR} when we compare them to Kartaltepe et al. (2010).

In Figure 1.36 we present SFR(IR) versus SFR(Hα) for the galaxies that we could measure both L_{IR} and $L_{H\alpha}$. We compare our results to data from Marleau et al. (2007). The SFR inferred from Hα is lower for cluster galaxies than for field galaxies of the same IR-inferred SFR, suggesting that cluster galaxies may be dustier (Cluster galaxies in Figure 1.36 with log(IR SFR) > 0.5 and log(Hα SFR) < -0.5).

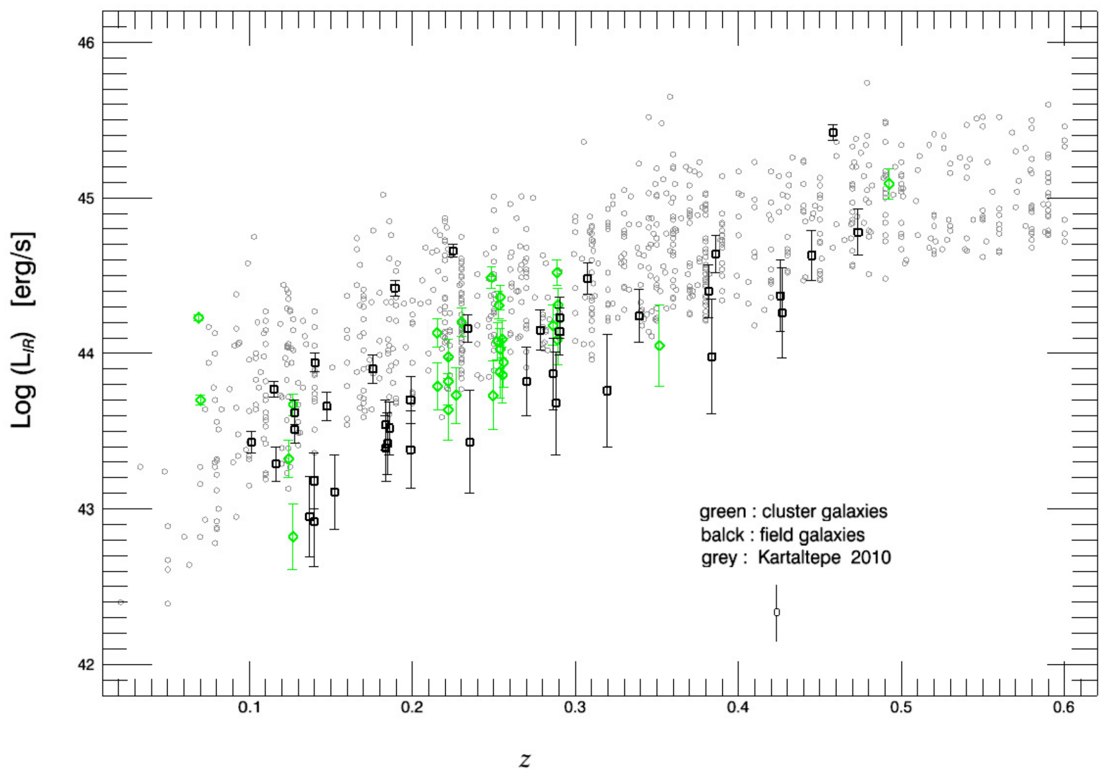

Figure 1.35 L_{IR} versus redshift of active star forming galaxies. AGNs, Post-starburst and Passive galaxies were excluded. Cluster galaxies are shown by green triangles and Field galaxies by black boxes. Background circles are data from Kartaltepe et al. (2010) for comparison (See Section 1.5.4).

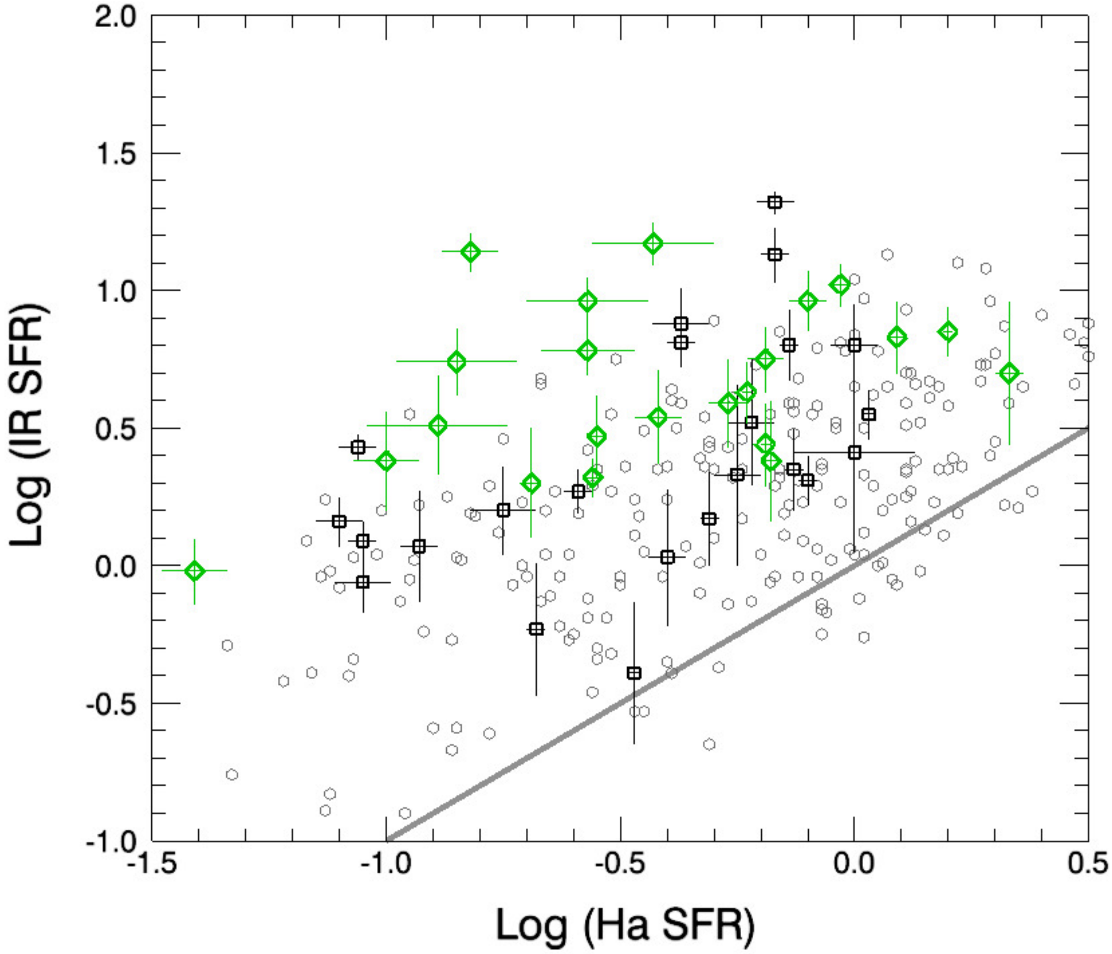

Figure 1.36 IR SFR versus Observed Hα SFR of those active star forming galaxies that both SFRs were measurable. Observed SFR(Hα) was not corrected for extinction. AGNs, Post-starburst and Passive galaxies were excluded. Cluster galaxies are shown by green diamonds and field galaxies by black boxes. Background grey circles are data from Marleau et al. (2007) for comparison. Solid line shows no extinction (IR SFR = observed Hα SFR).

1.5.5 The Specific Star Formation Rates (SSFR) of 24 μm Star forming Galaxies at Fixed Environment and Fixed Stellar Mass

To understand and compare the role of stellar mass and environment in star formation activities of 24 μm galaxies, we stack individual star forming cluster galaxies within different stellar mass and environmental bins. Note that we only analyze the 24 μm star forming galaxies in clusters in this section. In Figure 1.37 we plot the SSFRs of the star forming galaxies as a function of clustercentric radius in different stellar mass bins. This plot presents that SSFR is nearly independent of environment and agrees with the SDSS results (Kauffmann et al., 2004; Peng et al., 2010). Also, in Figure 1.38 we plot their SSFRs in different environments as a function of stellar mass and we find out that SSFR strongly depend on stellar mass. An order of magnitude drop in SSFR, independent of environment, from 10^{10} to 10^{12} $M_{\odot}$ shows the role of stellar mass that strongly dominates the importance of environment. Muzzin et al. (2012) found the same results for high redshift galaxy clusters at $z \sim 1$ from SpARCS GCLASS data and this conclusion is like what others found in the field studies.

We have to be careful about the role of environment. Although SSFR of star forming galaxies in clusters depends on stellar mass, environment quenches star formation faster than stellar mass. In clusters, star formation quenching is very rapid and its time scales are not comparable to the field.

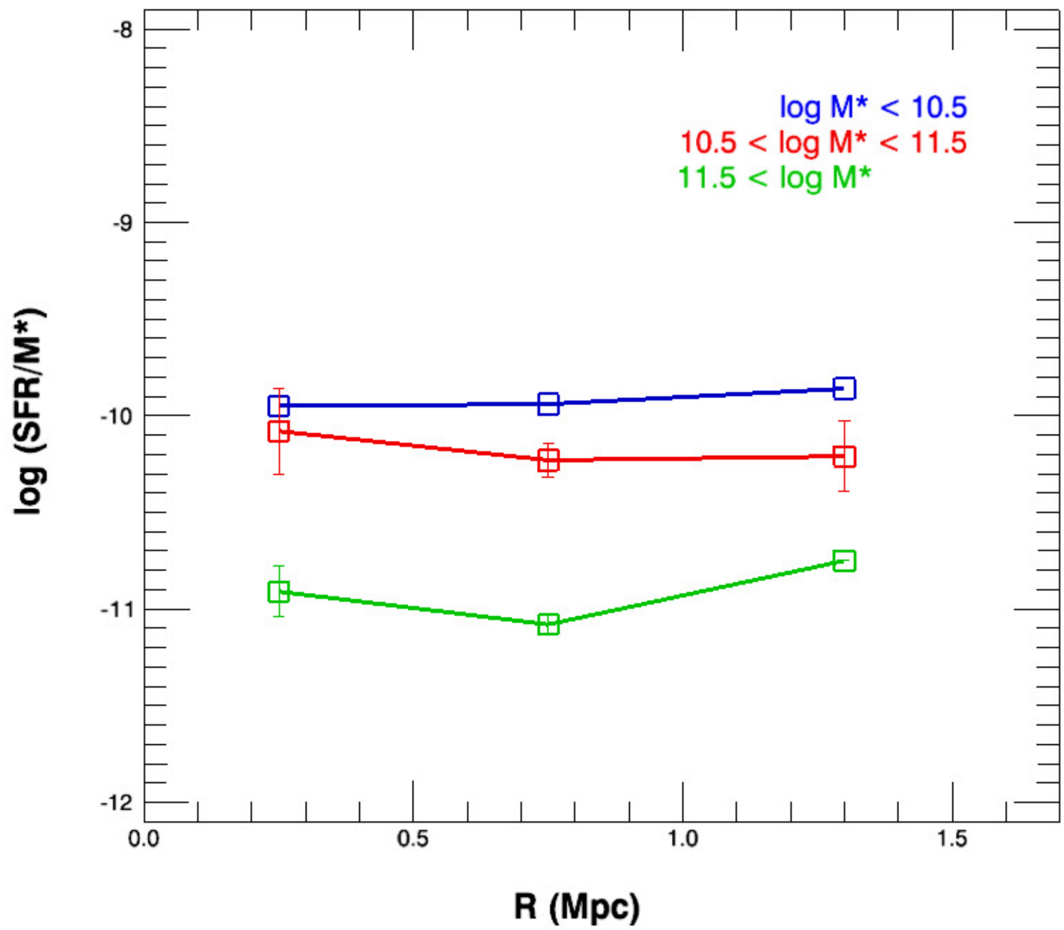

Figure 1.37 Logarithm of the mean SSFR of star forming galaxies in clusters as a function of clustercentric radius for galaxies with different stellar masses. The SSFR is nearly independent of environment at all stellar masses. The error bars represent the standard error in mean SSFR.

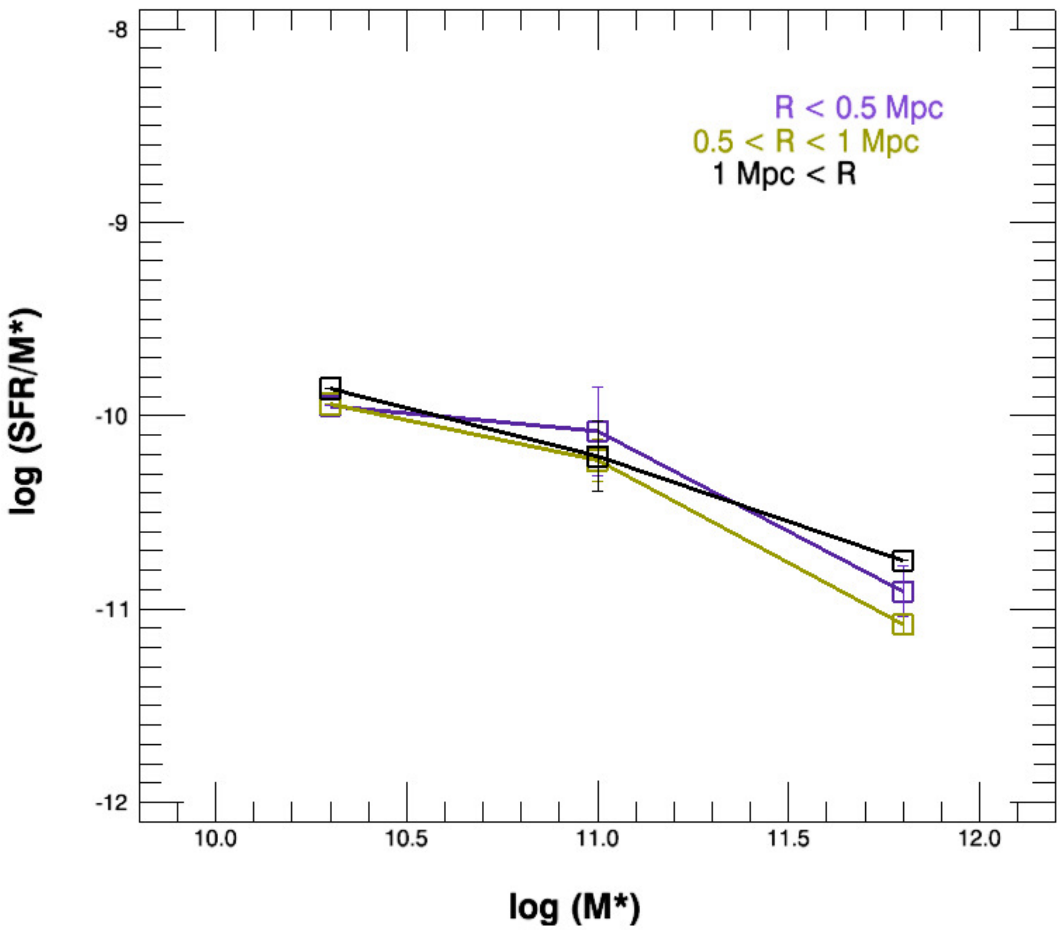

Figure 1.38 Logarithm of the mean SSFR of star forming galaxies in clusters as a function of stellar mass for galaxies in different environments. The SSFR is correlated with stellar mass in all environments. The error bars represent the standard error in mean SSFR.

1.6 Discussion

1.6.1 AGN Fraction in Clusters and in the Field

The fraction of AGNs in local rich clusters is much smaller than the field and past spectroscopic studies show that while 5% of the field galaxies have AGN activities, only 1% of the galaxies in local clusters have these activities (Dressler et al., 1985). In a study, Martini et al. (2009) found that cluster AGN fraction increases by a factor of eight from the present to $z \sim 1$, suggesting an evolution similar to the Butcher-Oemler effect for star forming galaxies, which supports the hypothesis that black holes and galaxies coevolve in dense environments. In our sample most of the identified AGNs are at higher redshifts and the AGN fraction in clusters is 7% (11% of 24 μm galaxies) in comparison to the field which is 30% (33% of 24 μm galaxies). Because our sample is small we can not quantify AGN fraction evolution with the redshift. We identify AGNs by optical diagnostic line ratios and our AGN fractions are much higher than optical samples in general. This is simply because we selected bright 24 μm sources. The fraction of 24 μm sources dominated by AGNs decreases with decreasing flux density (Donley et al., 2008; Brand et al., 2006), and in our sample luminous AGNs are much more than faint AGNs.

1.6.2 Star Formation History

Based on optical and infrared studies of the star formation activity in different environments we conclude that the amount of SFR of the 24 μm galaxies do not show much difference, but the amount of optical dust extinction of some IR luminous (massive) cluster galaxies seem to be more than the field galaxies with the same mass and infrared luminosity. In Figure 1.36, Hα SFR (uncorrected for the dust) of some of IR luminous cluster galaxies are less than their counterparts in the field (cluster galaxies with log(IR SFR) $>$ 0.5 and log(Hα SFR) $<$ -0.5). The optical SFR inferred from Hα emission of these cluster galaxies suggest that they may be dustier. The dependence of dust extinction on environment can be very important in star formation history. We need to work on a larger sample to finalize our conclusion in this section.

1.6.3 Passive Bright 24μm Galaxies

In our sample we discovered 11 bright 24 μm galaxies (8% of the entire sample, 6 in the clusters and 5 in the field) (24μm Flux $>$ 500 μJy) that are classified as either k galaxies or galaxies with Ell, Sa and Sb spectra. The 24 μm emissions from these dust-enshrouded passive galaxies reveal their AGN or star forming activities. Their mid-infrared emissions need a challenging interpretation. Figure 1.39 presents SDSS optical images of these galaxies in the clusters.

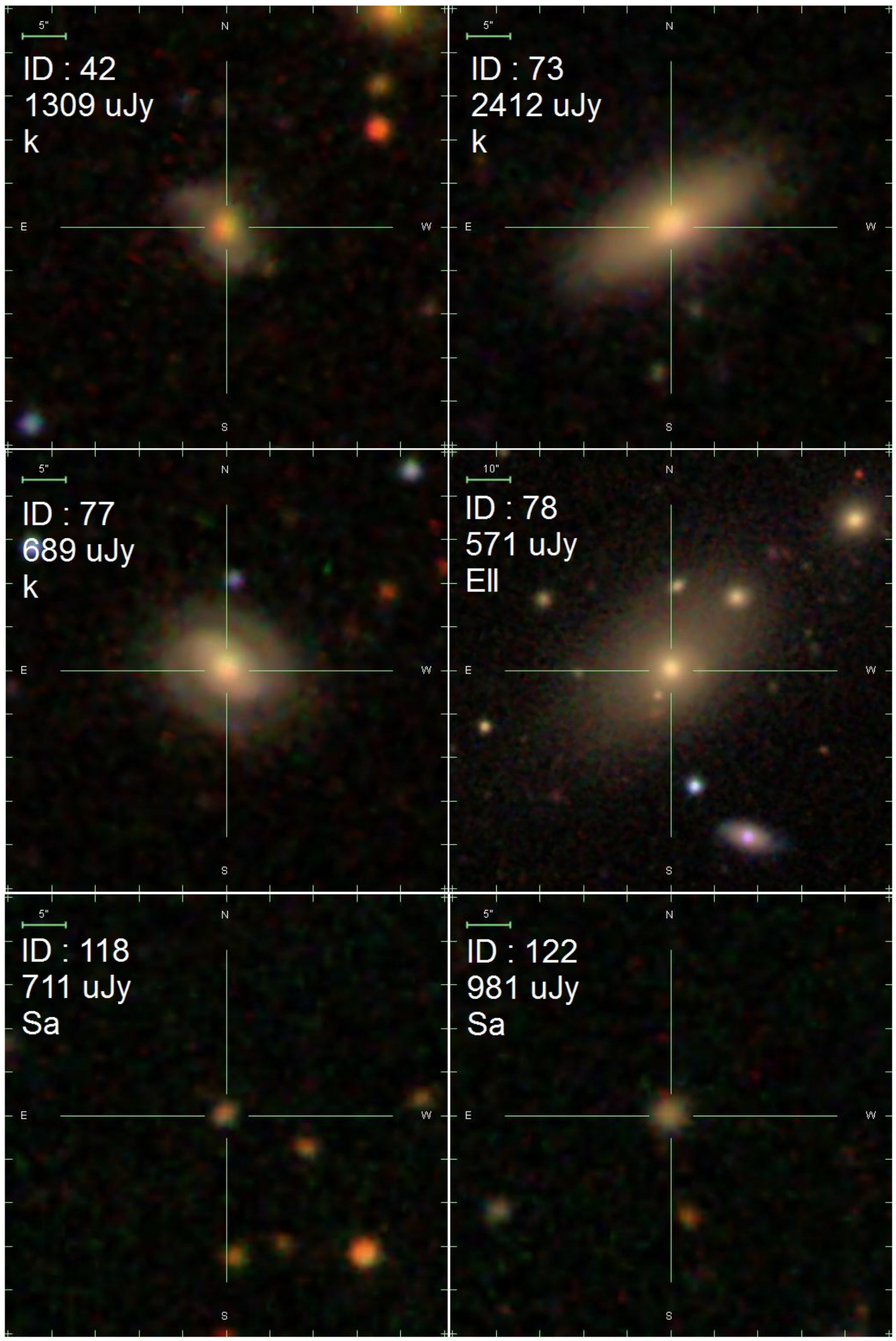

Figure 1.39 SDSS optical images of the bright passive 24 μm galaxies in clusters. Each galaxy is labled with ID, 24 μm flux and spectral type.

1.6.4 Poststarburst Galaxies in Clusters

Poststarbursts galaxies are rare among bright galaxies in all environments in the local universe ($z < 0.3$). At intermediate redshifts ($0.3 < z < 0.6$), several spectroscopic surveys of the galaxy clusters have reported large fractions of poststarbursts reaching to 1/4 of the entire population in distant massive clusters, which are more than the field (Poggianti et al., 2009; Dressler et al., 1999; Tran et al., 2003). The MORPHS survey (Dressler et al., 1999) of 10 rich galaxy clusters at $0.37 < z < 0.56$ reported a high poststarburst fraction of 21 $\pm$ 2 % in clusters. The CNOC1 survey (Balogh et al., 1999) of 15 clusters at $0.18 < z < 0.55$, of which only 4 of the clusters were in the redshift range of the MORPHS, found a low poststarburst fraction of 2.1 $\pm$ 0.7 %. Comparisons between these two surveys are discussed in details in Balogh et al. (1999). We only found three poststarbursts in our sample of cluster galaxies and they are all 24 μm sources. In an analysis, when we divide the sample into two groups of 24 μm galaxies at $0.07 < z < 0.27$ (37 galaxies) and $0.35 < z < 0.49$ (7 galaxies), we find one in the first group and two poststarbursts in the second group, which nearly agree with MORPHS and CONC1 results. We only found one poststarburst in our field sample which is also a 24 μm source.

Based on a hypothesis (Dressler et al., 2009a), e(a) galaxies are infalling starbursts which will be transformed to post-starburst galaxies with substantial burst followed by sudden decline in star formation rate. This scenario explains the general transformation of infalling spiral galaxies into elliptical galaxies in clusters. Unfortunately, poststarburst galaxies are very rare at low redshifts and it makes very hard to find enough evidences to support this hypothesis.

1.6.5 *Spitzer* MIPS 24 μm and Spectral Classifications

Infrared detections are potentially powerful methods of observing dust-obscured galaxies, which their nature are hidden under dust in the view of X-ray, UV, and optical observations. In this chapter we show the application of MIPS 24 μm observations in the study of star forming galaxies and AGNs. The low fraction of passive galaxies in the sample of 24 μm selected galaxies helps us to study star forming galaxies. About two thirds of our clusters and field samples are star forming galaxies, which shows the importance of 24 μm data in detection and measurement of SFR together. This is also true for AGN. MIPS 24 μm detection is another helpful tool to detect poststarbursts extensively; also, the high fraction of these rare galaxies at low redshifts in our sample in comparison with other surveys without 24 μm data, shows its importance. MIPS 24 μm observations should be considered as a "strong function of spectral type" (Dressler et al., 2009a).

Bibliography

Adelman-McCarthy, J. K. et al. 2009, VizieR Online Data Catalog, 2294, 0

Bai L. et al., 2007, Apj, 664, 181

Baldwin J. A., Phillips M. M., Terlevich R., 1981, pasp, 93, 5

Balogh, M. L., Morris, S. L., Yee, H. K. C., Carlberg, R. G., & Ellingson, E., 1999, Apj, 527, 54

Balogh M. L., Schade D., Morris S. L., Yee H. K. C., Carlberg R. G., Ellingson E., 1998, ApJ, 504, L75

Bell, E. F., McIntosh, D. H., Katz, N., & Weinberg, M. D. 2003, ApJS, 149, 289

Bertin, E., & Arnouts, S. 1996, A&AS, 117, 393

Bouwens, R. J., et al. 2008, ApJ, 686, 230

Brand et al., 2006, ApJ, 644, 143

Butcher, H.,& Oemler, A. Jr. 1978, ApJ, 279, 18

Chilingarian, I. V., Melchior, A.-L., & Zolotukhin, I. Y. 2010, MNRAS, 405,1409

Dale, D. A., & Helou, G. 2002, ApJ, 576, 159

Demarco, R., Wilson, G., Muzzin, A., et al. 2010, ApJ, 711, 1185

Donley et al., 2008, ApJ, 719, 1393

Dressler, A., Oemler, A., Gladders, M. G., Bai, L., Rigby, J. R., & Poggianti, B. M. 2009a ApJ, 699, L130

Dressler A., Smail I., Poggianti B. M., Butcher H., Couch W. J., Ellis R. S., Oemler A., Jr, 1999, ApJS, 122, 51

Dressler, A., Thompson, I. B., & Shectman, S. A. 1985, ApJ, 288, 481

Dressler A.,& Gunn J.E. 1983, ApJ, 270, 7

Fadda D. et al., 2006, AJ, 131, 285

Finn, R. A., Desai, V., Rudnick, G., Poggianti, B., Bell, E. F., Hinz, J., Jablonka, P., Milvang-Jensen, B., Moustakas, J., Rines, K., Zaritsky, D., 2010, ApJ, 720, 8

Finn, R. A., Zaritsky, D., & McCarthy, D. W. 2004, ApJ, 604, 141

Fisher, D., Fabricant, D., Franx, M., & van Dokkum, P. 1998, ApJ, 498, 195

Gladders M. D., & Yee H. K. C., 2005, ApJS, 157, 1

Gladders M. D., & Yee H. K. C., 2000, AJ, 120, 2148

Kartaltepe, J. S. et al., 2010a, ApJ, 709, 572

Kauffmann G. et al., 2004, MNRAS, 353, 713

Kauffmann G. et al., 2003a, MNRAS, 346, 1055

Kauffmann G. et al., 2003, MNRAS, 341, 33

Kennicutt, R. C. 1998, ARA&A, 36, 189

Kennicutt R. C. Jr, 1992, ApJ, 388, 310

Kewley, L. J., Groves, B., Kauffmann, G., & Heckmann, T. 2006, MNRAS, 372, 961

Kewley, L. J., Geller, M. J., & Jansen, R. A. 2004, AJ, 127, 2002

Kewley L. J., Dopita M. A., Sutherland R. S., Heisler C. A., Trevena J., 2001a, ApJ, 556, 121

Kurtz, M. J., Mink, D. J., Wyatt, W. F., Fabricant, D. G., Torres, G., Kriss, G. A., & Tonry, J. L. 1992, in ASP Conf. Ser. 25, Astronomical Data Analysis Software and Systems I, ed. D. M. Worrall, C. Biemesderfer,& J. Barnes (San Francisco, CA: ASP), 432

Lacy, M., et al., 2005, ApJS, 161, 4

Marleau et al., 2007, ApJ, 663, 218

Martini, P., Sivakoff, G. R., & Mulchaey, J. S. 2009, ApJ, 701, 66

Muzzin A. et al., 2012, ApJ, 746, 188

Muzzin, A., Wilson, G., Lacy, M., Yee, H. K. C., & Stanford, S. A., 2008, ApJ, 686, 966

Oemler, A. et al. 2009, ApJ, 693, 152

Papovich, C. et al. 2006, ApJ, 132, 231

Peng, Y., et al. 2010, ApJ, 721, 193

Poggianti, B. M. et al., 2009, ApJ, 693 112

Poggianti, B. M. et al., 1999, ApJ, 518, 576

Reddy, N. A., Steidel, C. C., Pettini, M., Adelberger, K. L., Shapley, A. E., Erb, D. K., & Dickinson, M. 2008, ApJS, 175, 48

Saintonge, A., Tran, K.-V. H., & Holden, B. P, 2008, ApJ, 685, L11

Salim S. et al., 2007, ApJS, 173, 267

Sargsyan, L. A., & Weedman, D. W. 2009, ApJ, 701, 1398

Tonry, J., & Davis, M. 1979, AJ, 84, 1511

Tran, K.-V. H., Franx, M., Illingworth, G., Kelson, D. D., & van Dokkum, P. 2003, ApJ, 599, 865

Vulcani B., Poggianti B. M., Finn R. A., Rudnick G., Desai V., Bamford S., 2010, ApJ, 710, L1

Watson, C. R., et al. 2009, ApJ, 696, 2206

Worthey, G., & Ottaviani, D. L. 1997, ApJS, 111, 377

Yan, R. et al 2006, ApJ, 648 281

Zhu, Y. N., Wu., H., Li, H. N., & Cao, C. 2010, Res. Astron. Astrophys., 10, 329

Chapter 2

The Evolution of Dusty Star Formation in Galaxy Clusters to z=1 in the SpARCS Survey

2.1 Introduction

Although the well known Butcher-Oemler effect has been studied thoroughly in optical and UV passbands, the hidden part of this iceberg is still unclear. In order to create a more comprehensive picture for galaxy evolution studies, a study of the mid-infrared Butcher-Oemler effect is necessary. The cause of increase in the number of star forming galaxies in clusters over redshift is still unknown for us and needs challenging explanations in astronomy. This evolution has been reported varying significantly : $f_{SF} \propto (1+z)^{2-7}$ (Kodama et al. 2004; Geach et al. 2006; Saintonge et al. 2008; Bai et al. 2009; Haines et al. 2009; Popesso et al. 2011). The observational importance of measuring this evolution $(1+z)^n$ is obvious for constraining our current galaxy evolution models.

After years of observations, data reductions and processing, SpARCS Cluster Survey catalogs are ready to use. Hundreds of galaxy clusters have been identified in this large 50 degree survey and we found a great opportunity to study dust-obscured star formation in clusters through *Spitzer* MIPS 24 μm passband. Our first goal is to present the Mid-infrared evolution of dusty starbursts in galaxy clusters. This project is similar to a project that has been done by our colleague Tracy Webb from McGill University on RCS survey with 42 clusters and deep 24 μm observations ($\sim$100 μJy) (Webb et al., 2013). Her experience with RCS data motivated us to perform this study on SpARCS data with two strong reasons : First, increasing the number of clusters in the analysis; second, extending the study to larger radii because the RCS study was limited to R_{200} .

2.2 Data

Our SpARCS survey covers the six fields of *Spitzer* SWIRE survey. We used 5 ready cluster catalogs (XMM field is still under construction). The localization of the red-sequence in color space gives us the cluster photometric redshifts with 5% accuracy. For each cluster, the optical richness has been parametrized by N_{red} (Lu et al., 2009), the number of red-sequence galaxies brighter than M*+2 within 0.5 Mpc. From the richness-velocity dispersion relation (Lu et al., 2009), we have an estimate of the radius R_{200}, and the total cluster mass M_{200} as below :

$$N_{red} \propto \sigma^{1.9} \tag{2.1}$$

$$N_{red} = 10^{-4} \times \sigma^{1.9} \tag{2.2}$$

$$R_{200} = \frac{\sqrt{3}\sigma}{10H(z)} \tag{2.3}$$

$$M_{200} = \frac{3\sigma^2 R_{200}}{G} \tag{2.4}$$

In this project, we selected 250 clusters from the SpARCS parent catalog to uniformly fill the redshift range $0.2 < z < 1.0$ and to span roughly an order of magnitude in mass (N_{red} =10-50 with $\sim$ 25% uncertainties and M_{200} =$10^{14-15} M_\odot$ with $\sim$ 40% uncertainties). In Figure 2.1 Mass-redshift distribution of our sample is presented and it shows that there is no bias due to our selection.

We use 24 μm source catalog of SWIRE fields (Shupe et al., 2008) that gives us 24 μm flux of the detected sources. The depth of this catalog allows us to reach at 350 μJy in EN1, EN2, CDFS and Lockman fields and also at 450 μJy in ES1 field, with

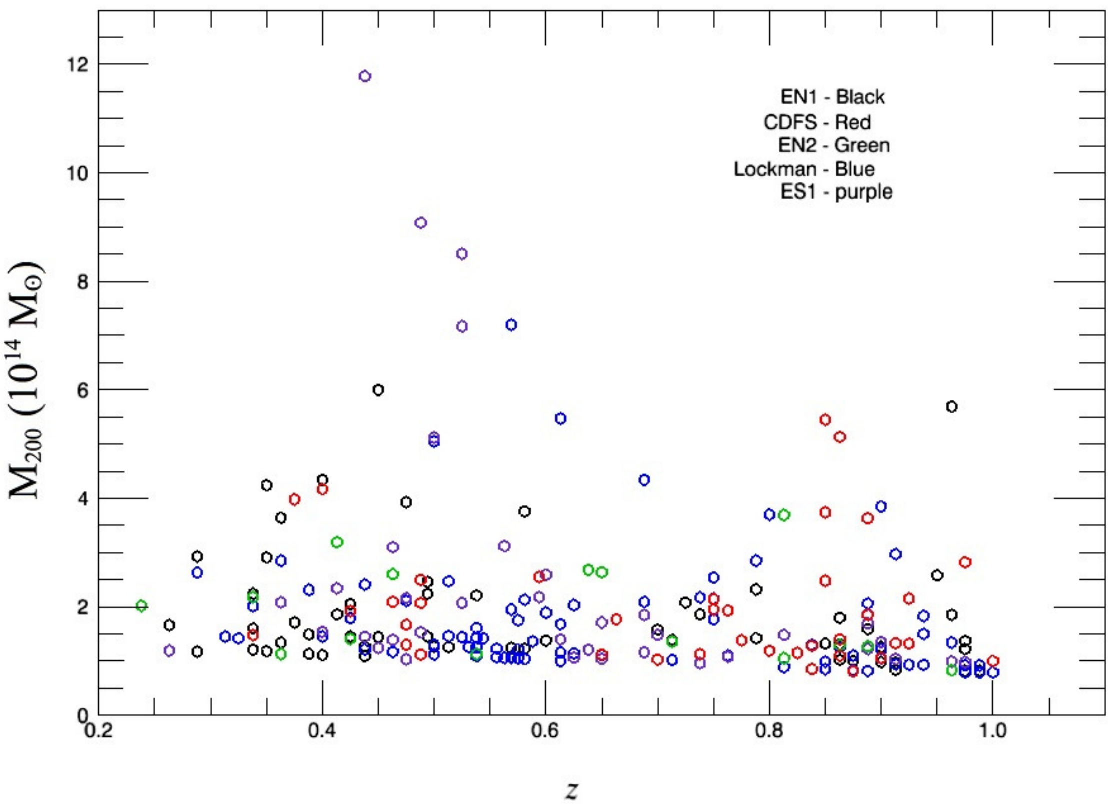

Figure 2.1 Estimated cluster mass versus redshift of our sample.

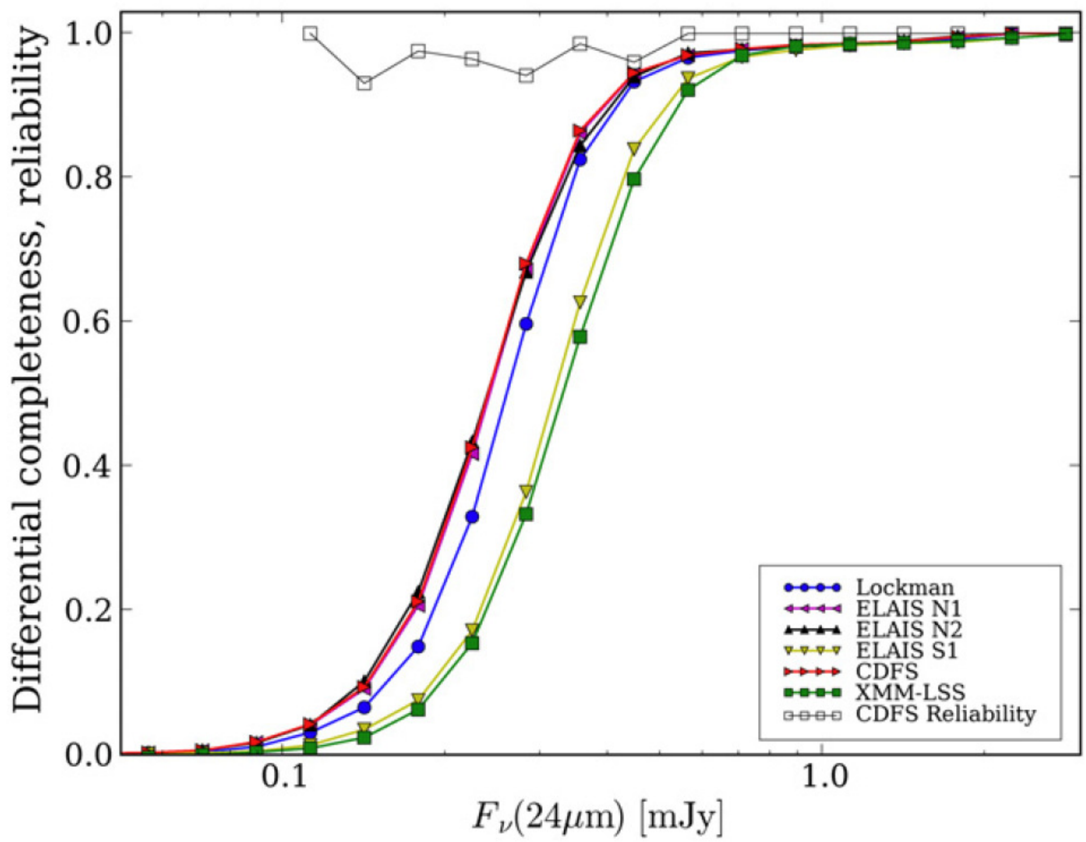

Figure 2.2 Filled symbols: differential completeness from simulations for EN1, EN2, and XMM-LSS fields. The curves for the other three fields were obtained by shifting the EN1 curve. Open squares: differential reliability defined as the fraction of SWIRE sources found in the deeper GTO data in CDFS. This plot is from Shupe et al. (2008).

80% completeness (Figure 2.2). We try to identify and eliminate stars from some stellar catalogs and also our z-band masks.

2.3 Analysis

By using Chary & Elbaz (2001) and Dale & Helou (2002) models, we computed the observed 24 μm flux at each cluster redshift, corresponding to a constant luminosity limit. Figure 2.3 presents the results of these computations. The constant luminosity limit in this project has been selected to be $L_{IR} = 6\times10^{11} L_\odot$ so we can reach at a flux limit of 350 μJy at $z = 1$ with 80% completeness corresponding to this luminosity limit. We assume that the shape of the IR SED of galaxies does not evolve appreciably over the redshift range of interest. This luminosity limits our sample to Luminous Infrared Galaxies (LIRGs) and brighter, that have corresponding star formation rates (SFRs) of more than $\sim 90\ M_\odot \mathrm{y}r^{-1}$.

For each cluster we count the number of galaxies above its calculated flux limit and within the fixed radii and corresponding R_{200} of cluster center. In order to estimate the background, for each cluster, we measure the average number of galaxies above its calculated flux limit and within the same radius in hundreds of randomly placed apertures in the corresponding SWIRE field. We used about 250 random apertures per deg^2 in each field. For example, the EN1 field that is 9.64 deg^2 has about 2400 random apertures. The standard deviation of the counts in random apertures gives

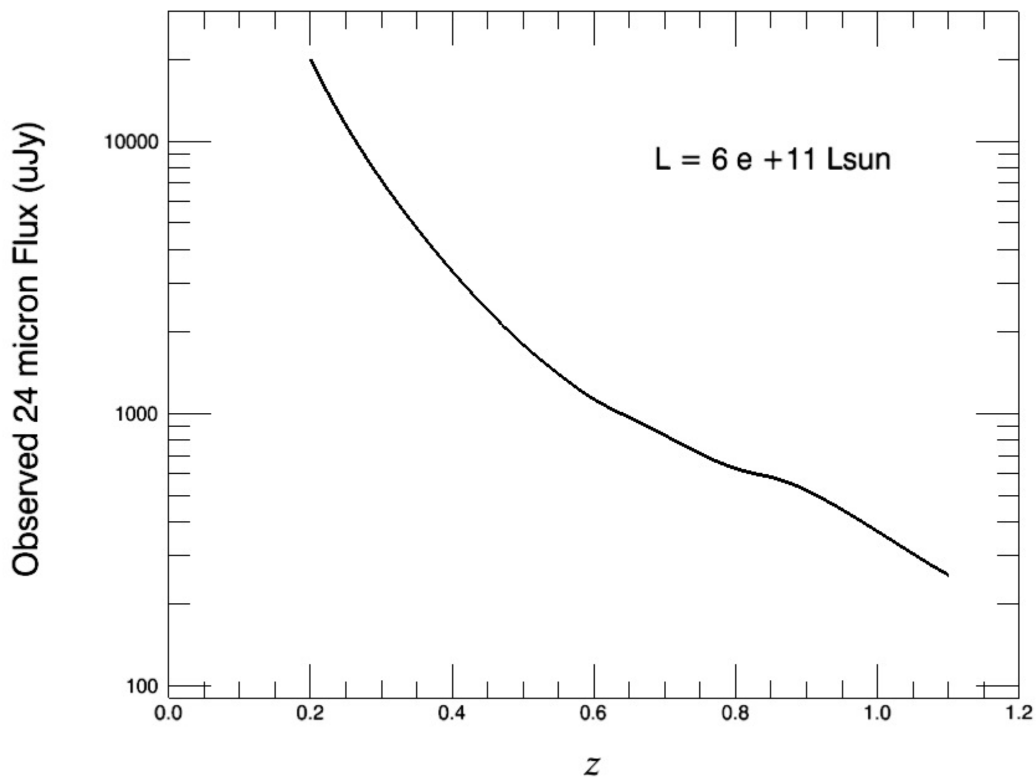

Figure 2.3 The expected observed 24 μm flux of a template galaxy with $L_{IR} = 6{\times}10^{11}L_{\odot}$ computed from the combined models of Chary & Elbaz (2001) and Dale & Helou (2002). Our 24 μm source catalog is deep enough to reach at this luminosity at $z = 1$ with 80% completeness (350 μJy).

us an estimate of the field to field variance in the background. We use this as the dominant uncertainty on each cluster measurement.

Note that we estimated R_{200} and M_{200} from the richness-velocity dispersion relation (Lu et al., 2009) (relation 2.1) that has an intrinsic scatter. The richness parameter N_{red} also has ~25 % uncertainty. There are random errors in the redshifts and systematic errors in the flux-limit estimates. In this work, we do not attempt to incorporate these uncertainties. Random uncertainties will be minimized by our stacking technique and systematics only matter if they are redshift dependent. The size of our sample is large enough to remove uncertainties due to cluster to cluster variations by averaging over bins of redshift with a minimum of ~50 clusters per bin.

2.4 Results

2.4.1 Number counts of IR galaxies in Galaxy Clusters

For each cluster, by subtracting the background average from the cluster count, we measure the total number of galaxies with $L_{IR} > 6\times10^{11} L_{\odot}$ in excess of the average background counts, within the fixed radii and R_{200} of the cluster center. Figure 2.4 through Figure 2.9 show our results for fixed radii in SpARCS fields. We also normalize each integrated count by the total mass of the cluster to remove additional scatter due to the random variation in the average mass from bin to bin. Figure 2.10 through Figure 2.15 show the results of these measurements in 5 fields of the SpARCS survey. Figure 2.16 and Figure 2.17 show the average number counts of IR galaxies in clusters in four redshift bins.

By analyzing Figure 2.4 to Figure 2.15, we found a bias in the number counts from $z = 0.56$ to $z = 0.73$ which makes the average of these numbers negative in this redshift bin. Even by comparing these figures by eye, we can conclude that most of the clusters in this bin have less IR galaxies than the field. It seems that the problem is underestimating the clusters photometric redshifts in this redshift bin in our cluster catalog. As we see in Figure 2.9, this region lowers the number counts of the middle redshift bins that makes the evolution stronger than its reality. Since this region gives suspiciously negative number counts, we eliminate this region which has 50 clusters, from the rest of our analysis at this point. Remember, our sample had 250 clusters at first, so by eliminating 50 clusters in this suspicious region we work on the remaining 200 clusters.

Figure 2.16 and Figure 2.17 show the results for the rest of 200 clusters in the sample, in four redshift bins, with the same number of clusters in each bin. The increase in the average number of IR luminous galaxies per unit cluster halo mass at higher redshifts is an evidence of evolution in clusters. The best power-law fit in the form of $N_{>}/\mathrm{M} \propto (1+z)^n$ gives n = 9.6 $\pm$ 1.6 for R = 2 Mpc and n = 5.2 $\pm$ 0.5 for R_{200} (least-squares fitting method using Gnuplot). Note that we choose the largest radius (R = 2 Mpc) because we want to catch the infrared galaxies as much as possible and also we choose R_{200} because it is about the virial radius of the clusters.

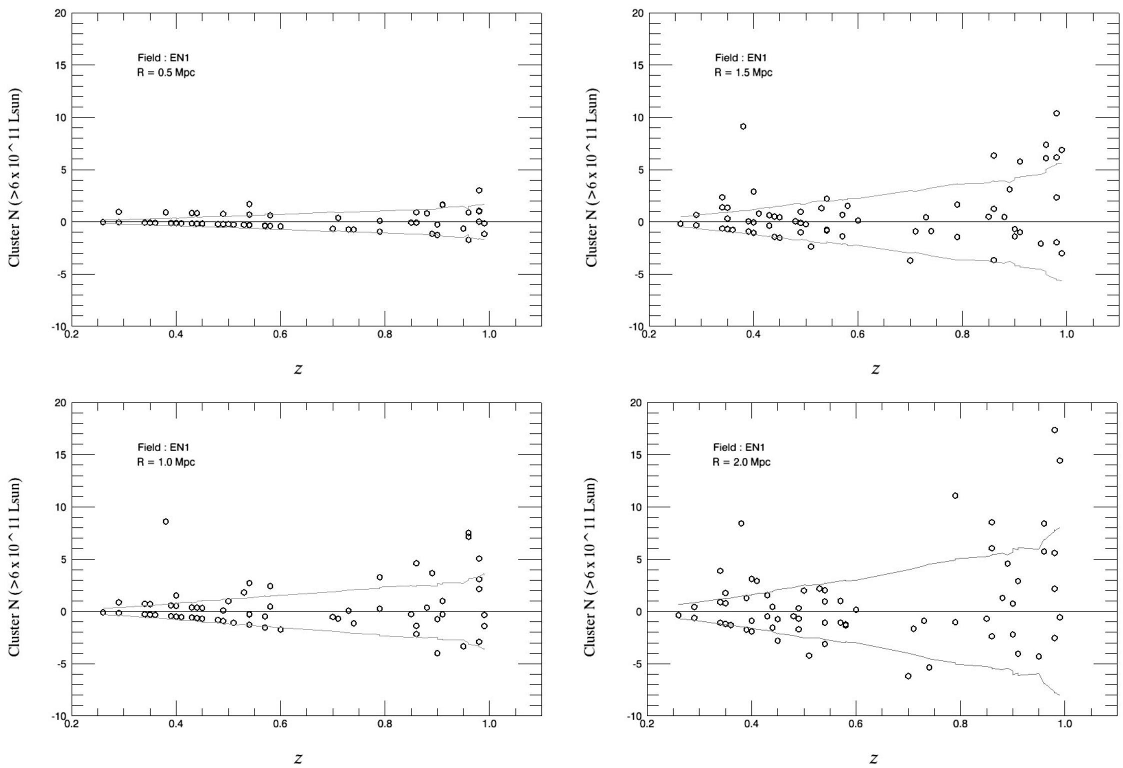

Figure 2.4 The total number of galaxies with $L_{IR} > 6{\times}10^{11} L_{\odot}$ in excess of the average background counts, within the fixed radii (0.5, 1.0, 1.5 and 2.0 Mpc) of the cluster centers in EN1 field. The solid lines represent the standard deviation of the average background counts ($\pm\sigma$). Since the number of random apertures is 1250 < n < 2750 and the random error of the background average is calculated from $\sigma/\sqrt{n}$, error bars are small and can not be displayed on this diagram.

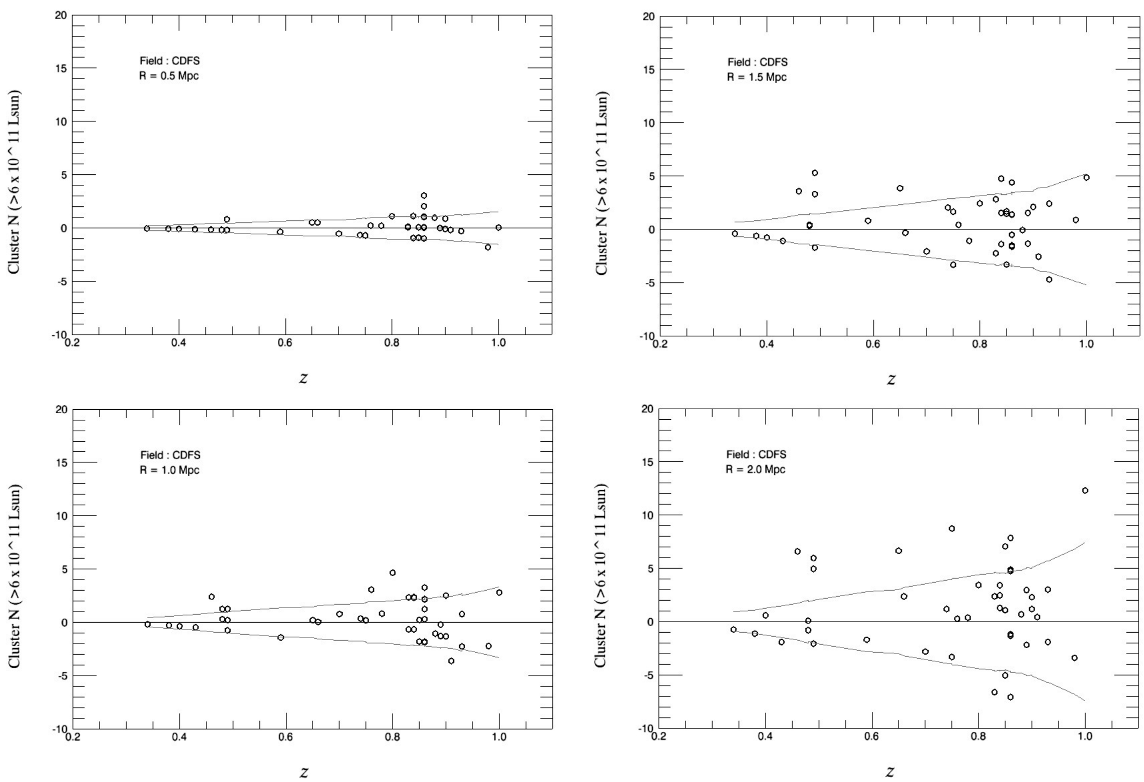

Figure 2.5 Same as figure 2.4 but for CDFS field.

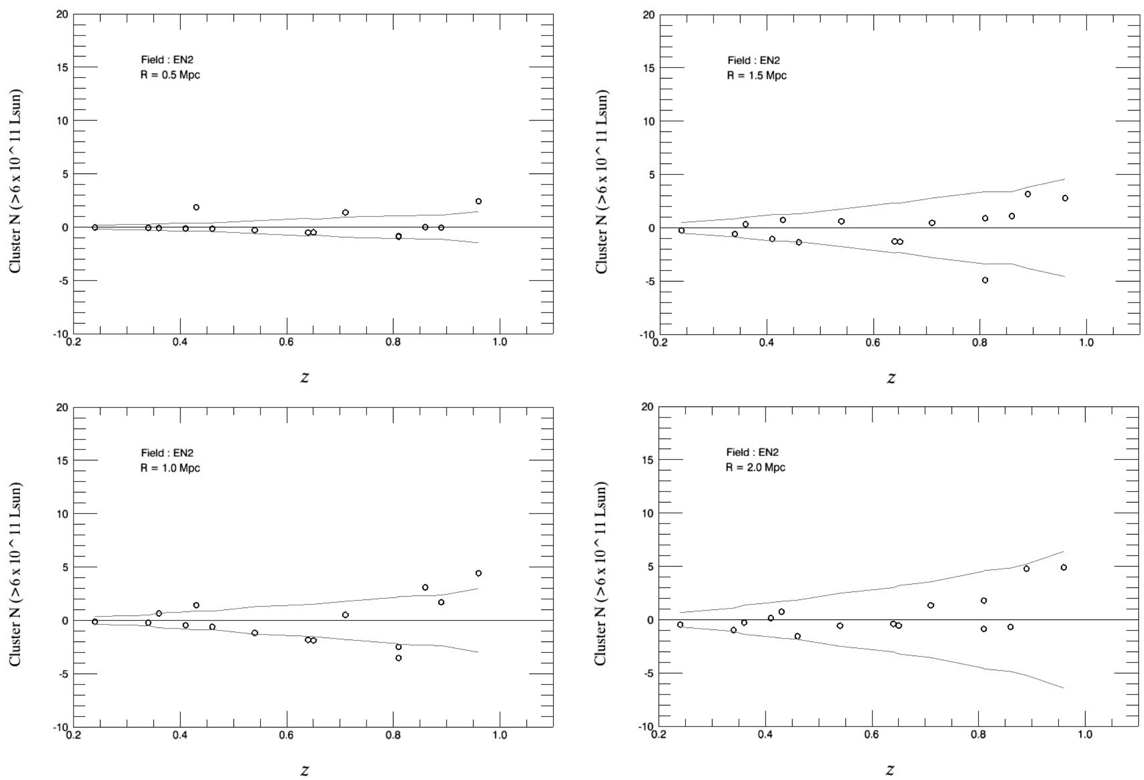

Figure 2.6 Same as figure 2.4 but for EN2 field.

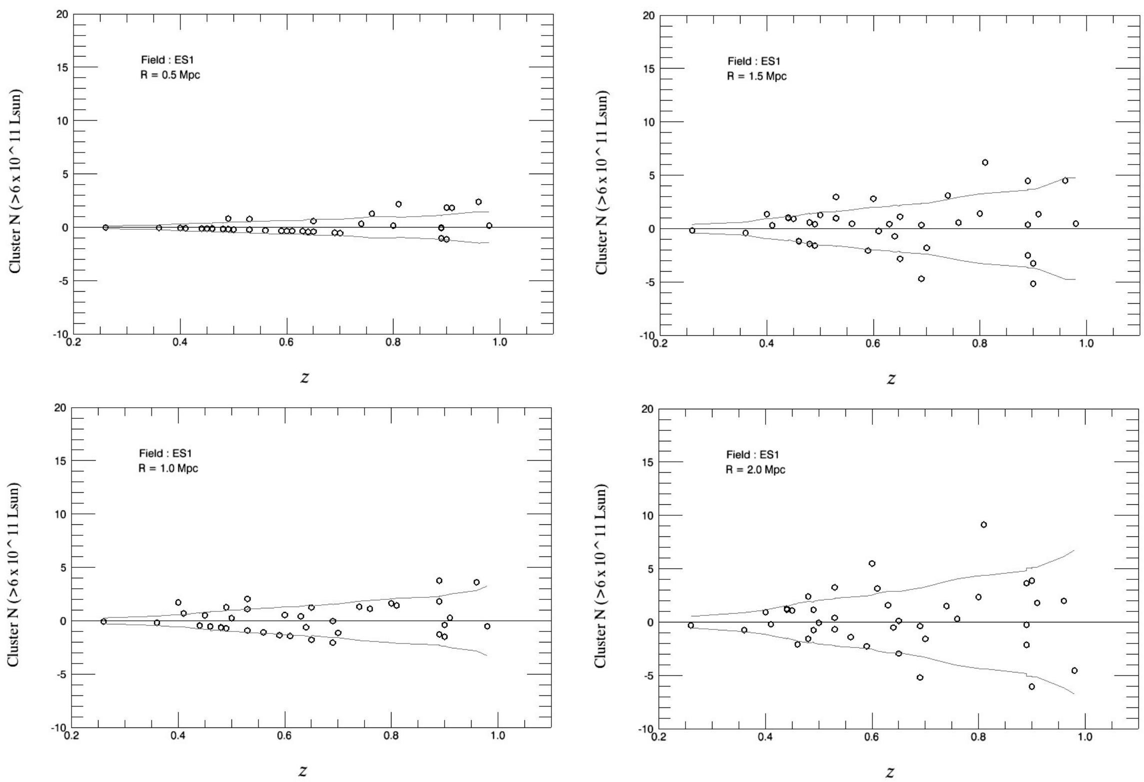

Figure 2.7 Same as figure 2.4 but for ES1 field.

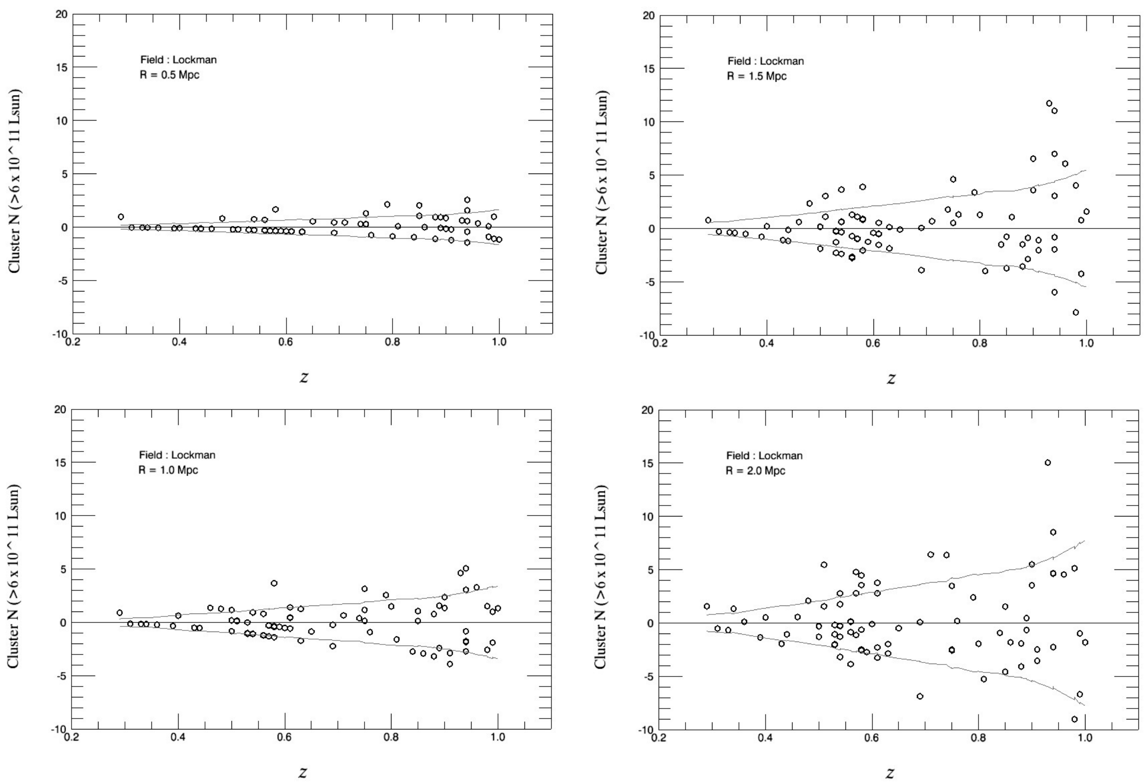

Figure 2.8 Same as figure 2.4 but for Lockman field.

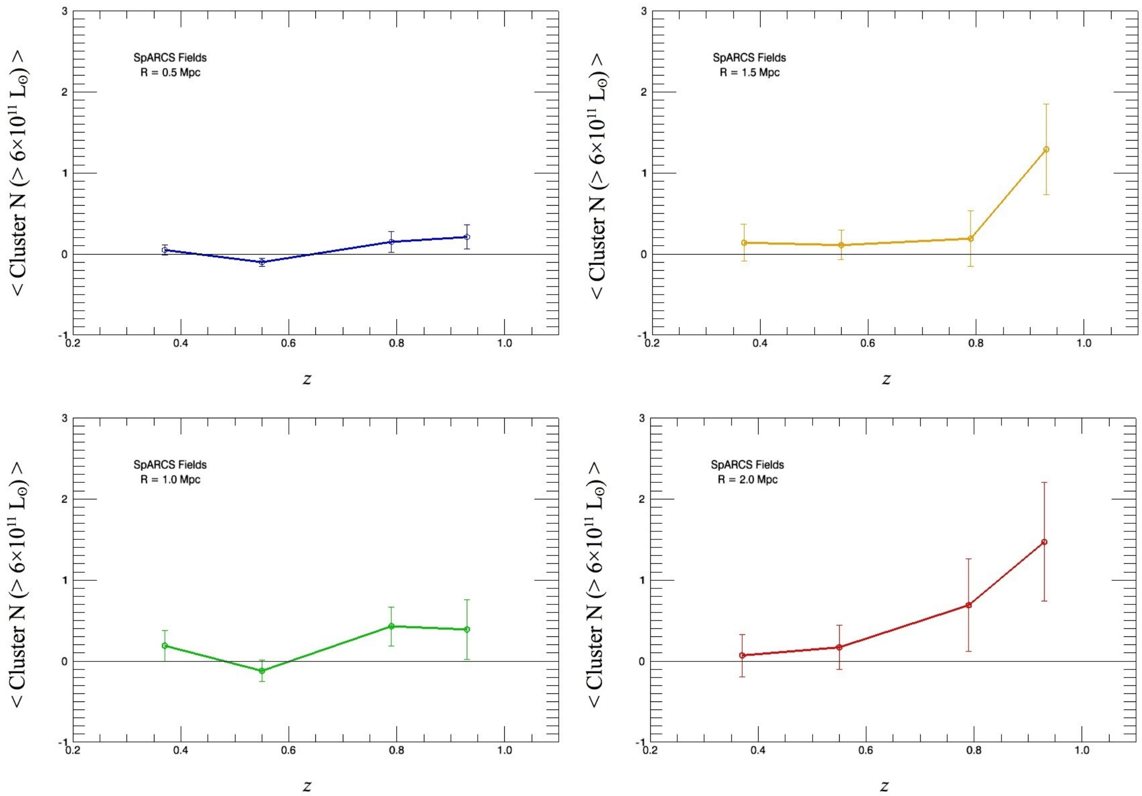

Figure 2.9 The mean number of galaxies with $L_{IR} > 6{\times}10^{11}L_{\odot}$ in excess of the average background counts, within the fixed radii (0.5, 1.0, 1.5 and 2.0 Mpc) of the cluster center. We averaged figure 2.4 to 2.8 in four redshift bins and the uncertainties correspond to the standard errors in the mean.

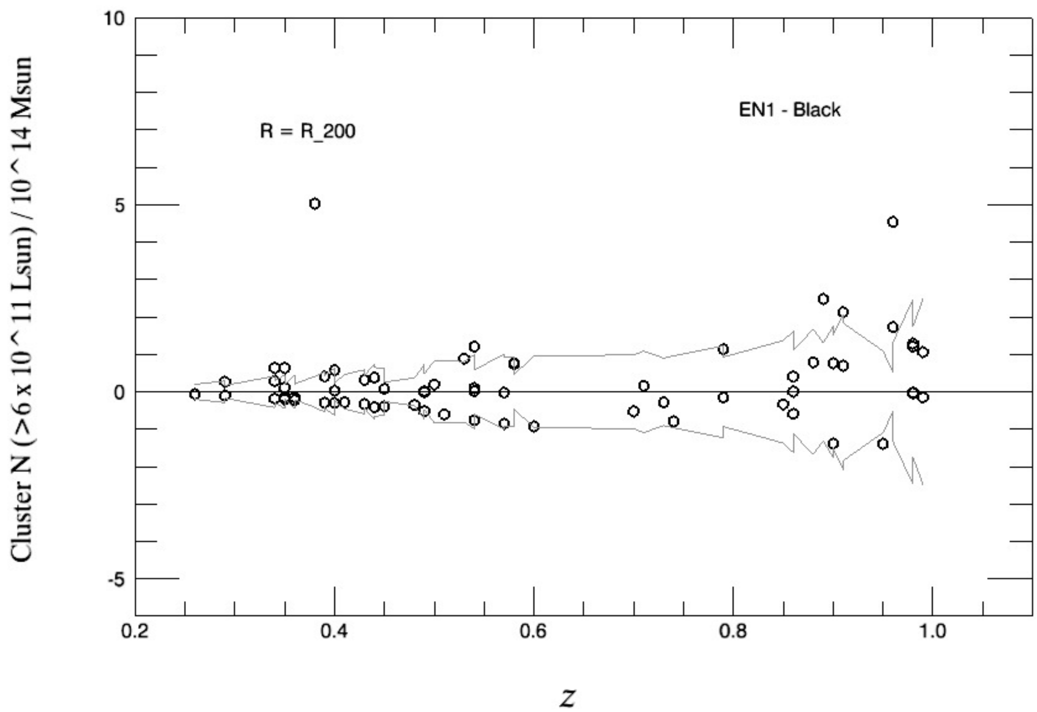

Figure 2.10 The total number of galaxies with $L_{IR} > 6{\times}10^{11} L_{\odot}$ in excess of the average background counts, within R_{200} of the cluster center and divided by total mass of the cluster in EN1 field. The continuous solid lines represent the standard deviation of the average background counts divided by total mass for each cluster ($\pm\sigma/M_{200}$). For each cluster, $\pm\sigma/M_{200}$ is on the solid lines.

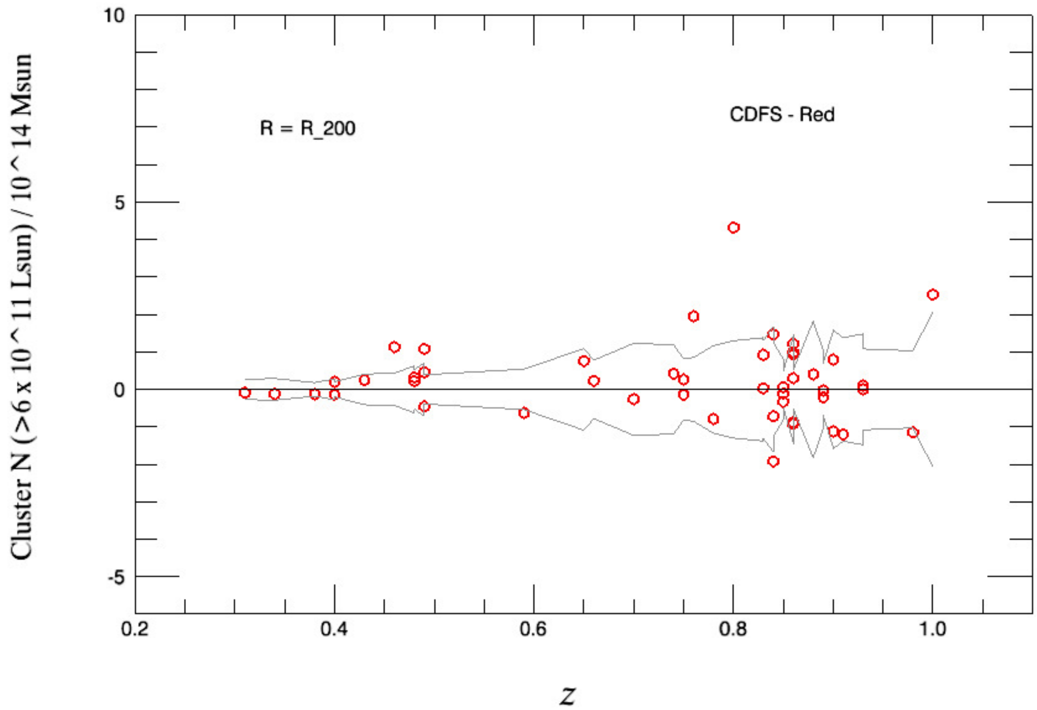

Figure 2.11 same as figure 2.10 but for CDFS field.

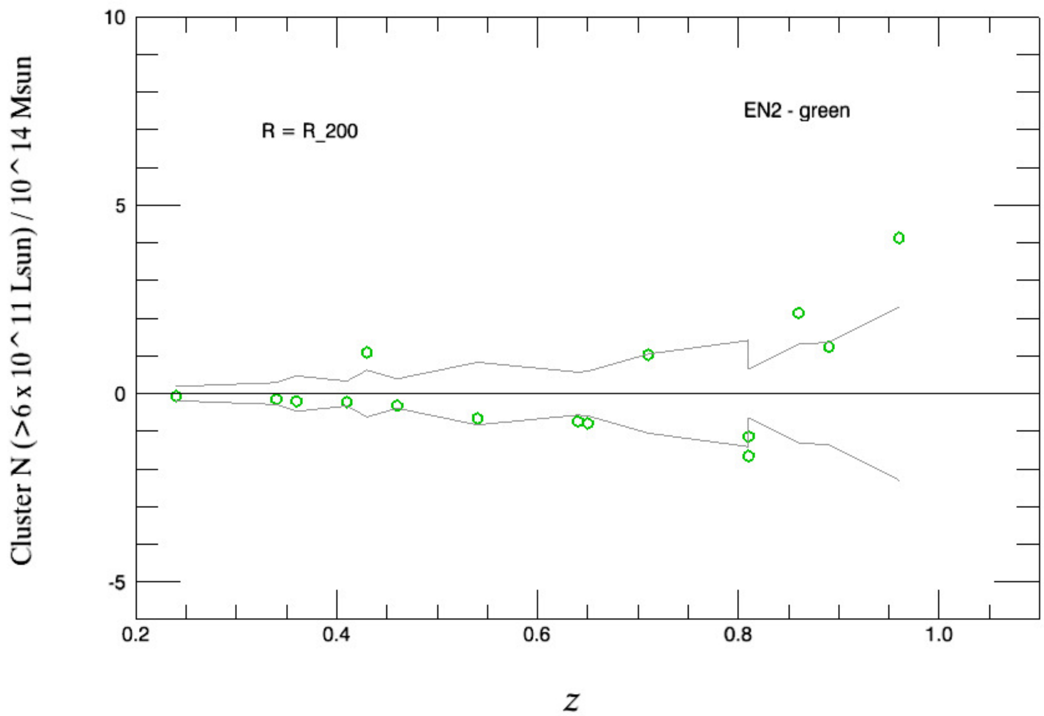

Figure 2.12 same as figure 2.10 but for EN2 field.

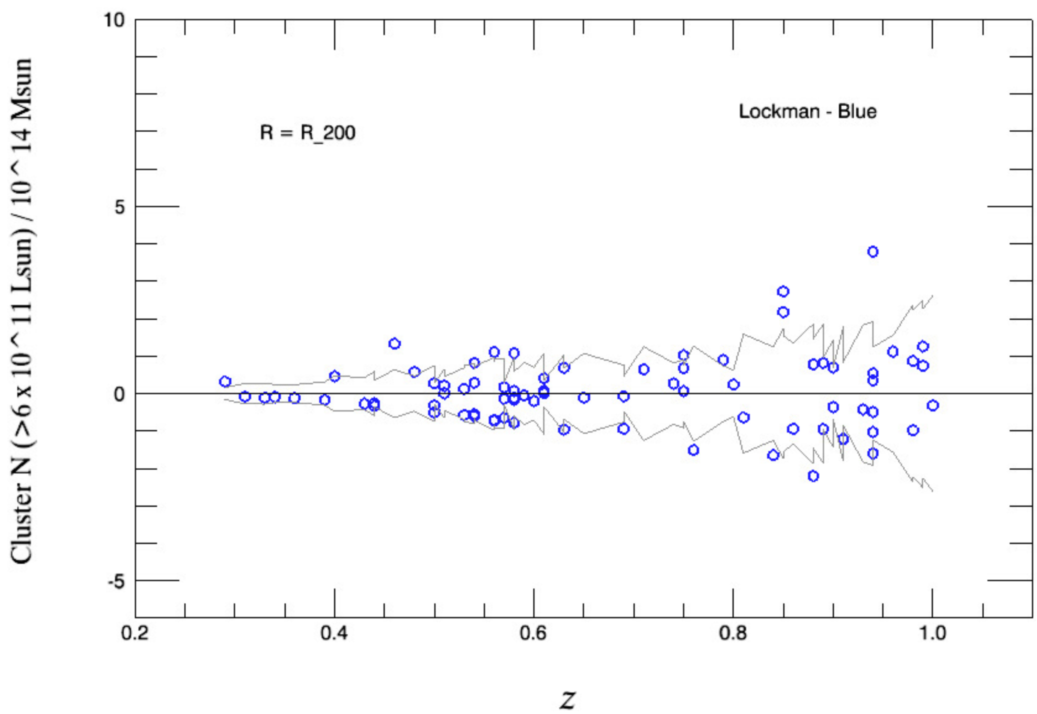

Figure 2.13 same as figure 2.10 but for Lockman field.

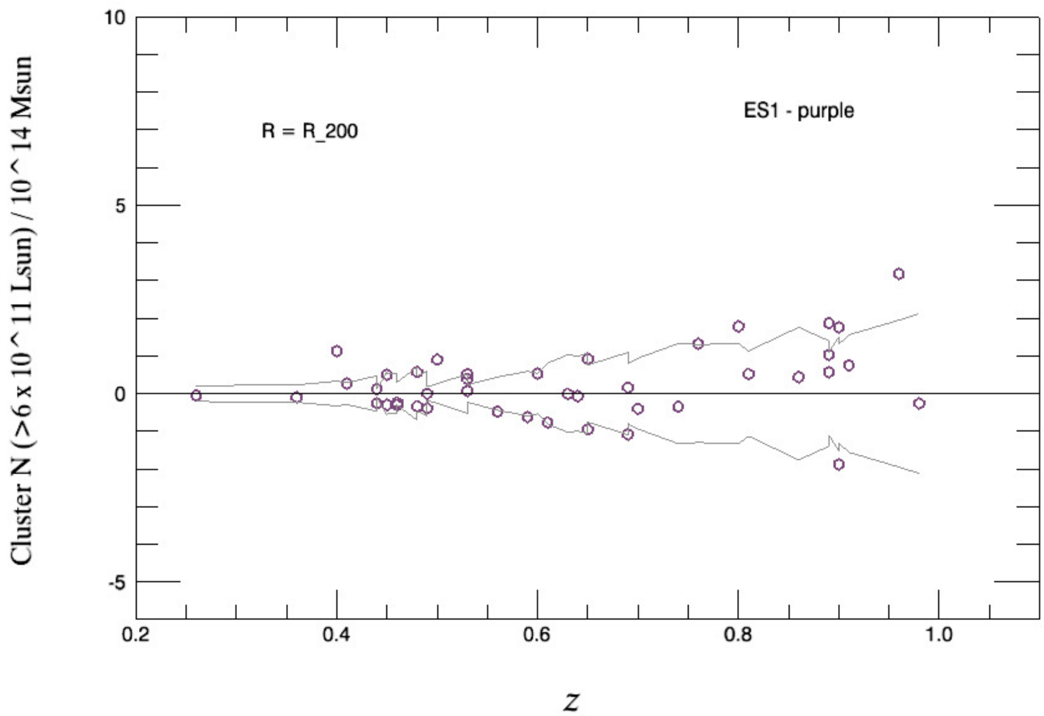

Figure 2.14 same as figure 2.10 but for ES1 field.

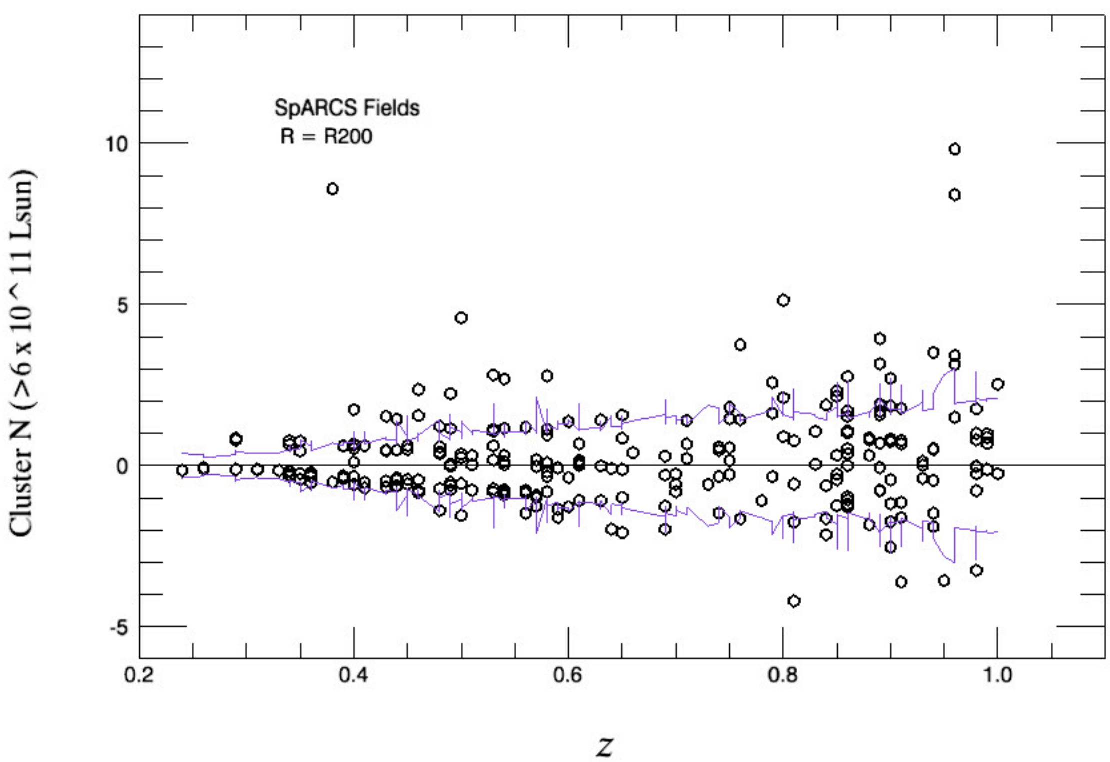

Figure 2.15 same as figure 2.4 but for all the fields within R_{200} of the cluster centers.

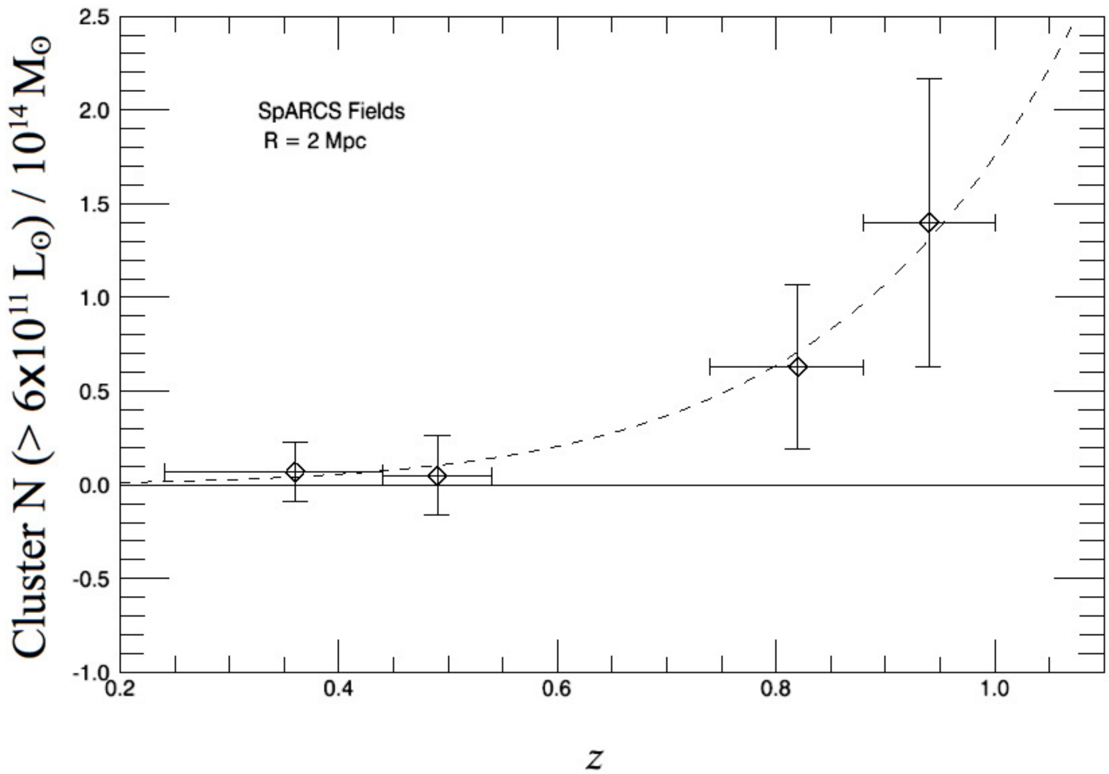

Figure 2.16 The number of galaxies with $L_{IR} > 6{\times}10^{11} L_{\odot}$ in excess of the average background counts, within 2 Mpc of the cluster center, normalized by cluster halo mass M_{200} and averaged in four redshift bins. Y error bars correspond to the standard errors in the mean and X error bars only present the redshift ranges of the bins. The dashed line represents the best power-law fit in the form of $N_{>}$/M $\propto (1+z)^n$ with n $= 9.6 \pm 1.6$.

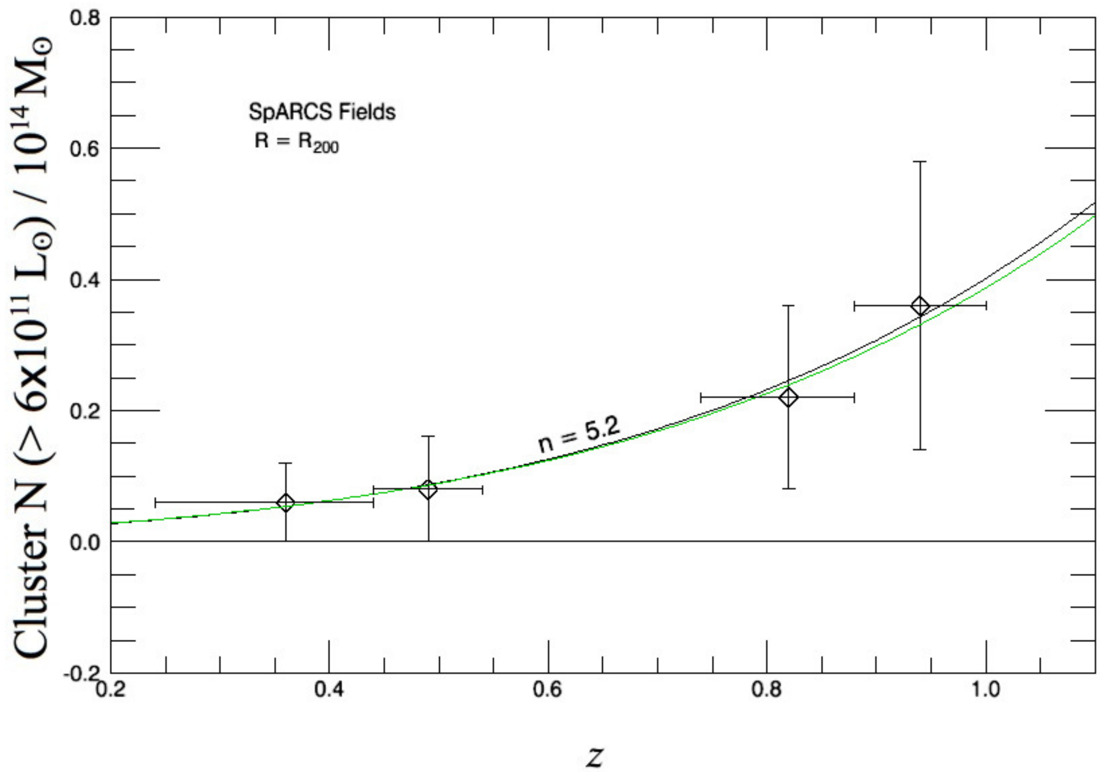

Figure 2.17 Same as figure 2.16 but within R_{200} of the cluster center. The black dashed line represents the best power-law fit in the form of $N_{>}/\mathrm{M} \propto (1+z)^n$ with n = 5.2 ± 0.5, the green dotted line is the best fit of Webb et al. (2013) with n = 5.1 and normalized at z = 0.4 to our fit. Note Y error bars correspond to the standard errors in the mean and X error bars only present the redshift ranges of the bins.

2.4.2 Comparison with the Evolution in the Field

Previous section shows that the average number of IR luminous galaxies increases with redshift. In order to study the evolutionary effects on galaxies in clusters, we need to consider the evolution of the field galaxies in the same redshift range. Clusters are continually accreting new galaxies from the field; however, as the most dense regions in the universe, their environments show some evolutionary effects that belong specifically to clusters. Therefore, any observed evolution in a cluster can be accounted either for the new infall population or for the cluster itself. In order to distinguish these two different behaviors in our observed evolution, we compare our results in clusters with the field. Since the infall galaxies are newly accreted galaxies, their evolution should follow the same evolution seen in the field. Based on this assumption, we use Le Floc'h et al. (2005) IR luminosity functions for the field galaxies as below :

$$\phi_{IR}(L) = \frac{dN(L)}{dV d\log(L)} = \phi^{\star}_{IR}\left(\frac{L}{L^{\star}_{IR}}\right)^{1-\alpha_{IR}} \exp\left(-\frac{1}{2\sigma^2_{IR}}\log^2\left[1+\frac{L}{L^{\star}_{IR}}\right]\right) \tag{2.5}$$

These luminosity functions show the evolution of $L^{\star}_{IR}$ and $\phi^{\star}_{IR}$ in the forms of :

$$L^{\star}_{IR} \propto (1+z)^{3.2} \tag{2.6}$$

$$\phi^{\star}_{IR} \propto (1+z)^{0.7} \tag{2.7}$$

The comparison is based on the method of Webb et al. (2013) and Haines et al. (2009). By using the $L^{\star}_{IR}$ evolution relation and normalizing the depth of $L_{IR} = 6\times10^{11}L_{\odot}$ at $z = 1$, the corresponding flux depth at each redshift is calculated and presented with the dashed line in Figure 2.18. By repeating the same analysis done for Figure 2.16 and Figure 2.17, the number of IR luminous galaxies above this parametrized flux depth is counted. These number counts are averaged in previous redshift bins and the results are presented in Figure 2.19 and Figure 2.20. Note that in Section 2.4.1, the number of galaxies above the solid line ($L_{IR} = 6{\times}10^{11} L_{\odot}$) is counted but in this section the number of galaxies above the dashed line is counted. The results show the excess of IR galaxies in each redshift bin but there is no increase in these numbers with redshift. The best power-law fit in the form of $N_{>}/\mathrm{M} \propto (1+z)^n$ gives us n = 0.16 ± 0.28 for R = 2 Mpc and n = -0.6 ± 1.0 for R_{200} (least-squares fitting method using Gnuplot). These fits are almost flat and comparing these results with the results in Section 2.4.1 shows that the population of IR cluster galaxies follows the field evolution. Therefore, the observed evolution in Section 2.4.1 is due to new infalling galaxies not the cluster itself. Note that the parametrized flux depth is only used in this section.

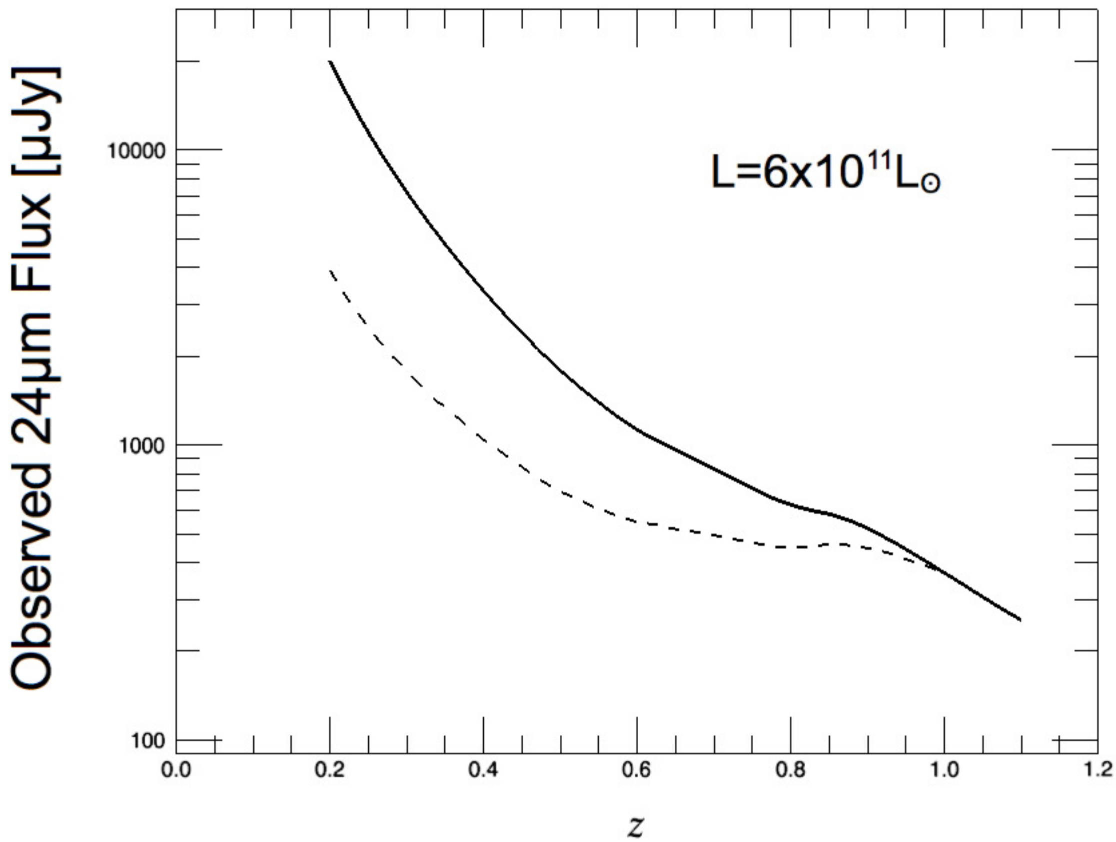

Figure 2.18 Solid line : The expected observed 24 μm flux of a template galaxy with $L_{IR} = 6{\times}10^{11}L_{\odot}$ computed from the combined models of Chary & Elbaz (2001) and Dale & Helou (2002). Our 24 μm source catalog is deep enough to reach at this luminosity at $z = 1$ with 80% completeness (350 μJy) . Dashed line : Parametrized flux depth of $L_{IR} = 6{\times}10^{11}L_{\odot}$ at $z = 1$ which follows the evolution of $L^{\star}_{IR}$ of the field at $z < 1$. This parametrized flux depth is only used in Section 2.4.2.

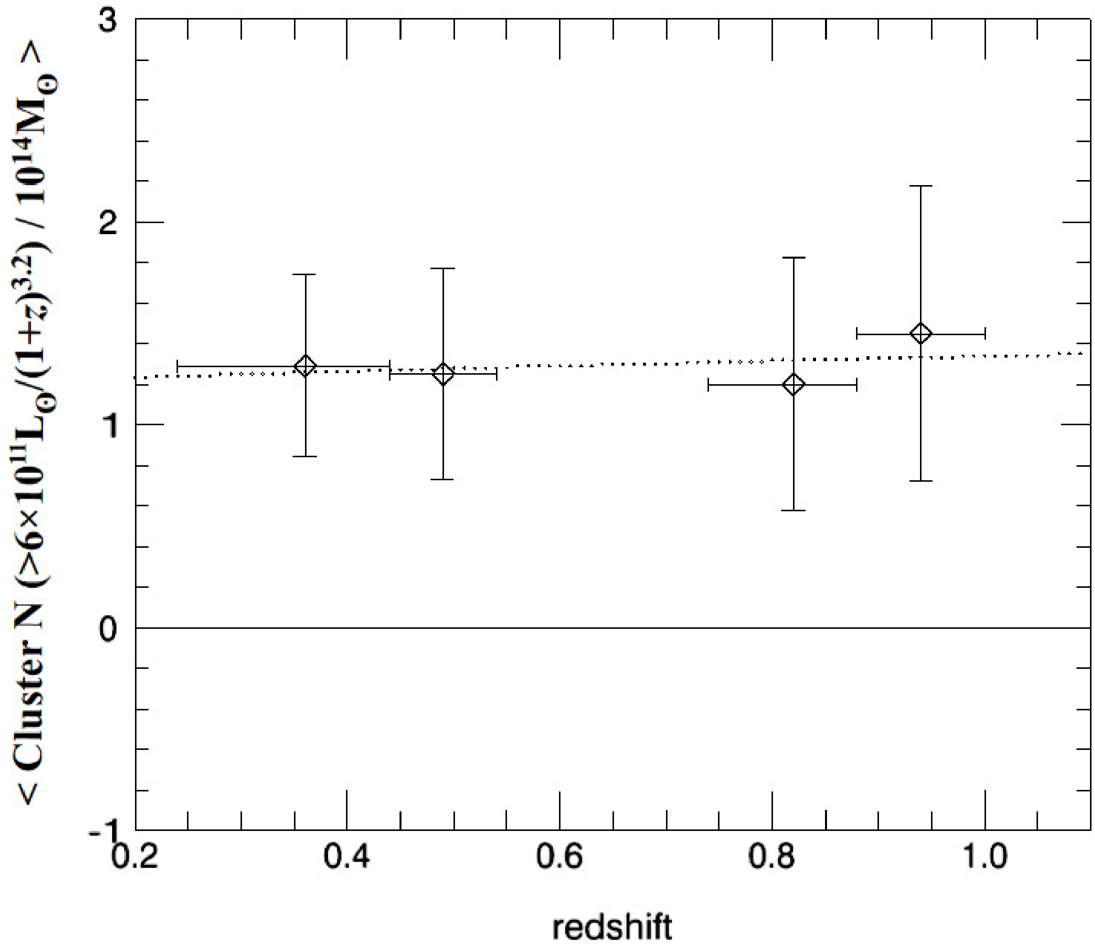

Figure 2.19 Similar to figure 2.16, but with considering the evolution of $L^{\star}_{IR}$ in the field. We count the number of IR luminous galaxies above the parametrized flux depth in figure 2.18 and within R = 2 Mpc of the cluster center. The dotted line represents the best power-law fit in the form of $N_{>}/\mathrm{M} \propto (1+z)^n$ with n = 0.16 ± 0.28 . Note that X error bars only present the redshift ranges of the bins and Y error bars correspond to the standard errors in the mean.

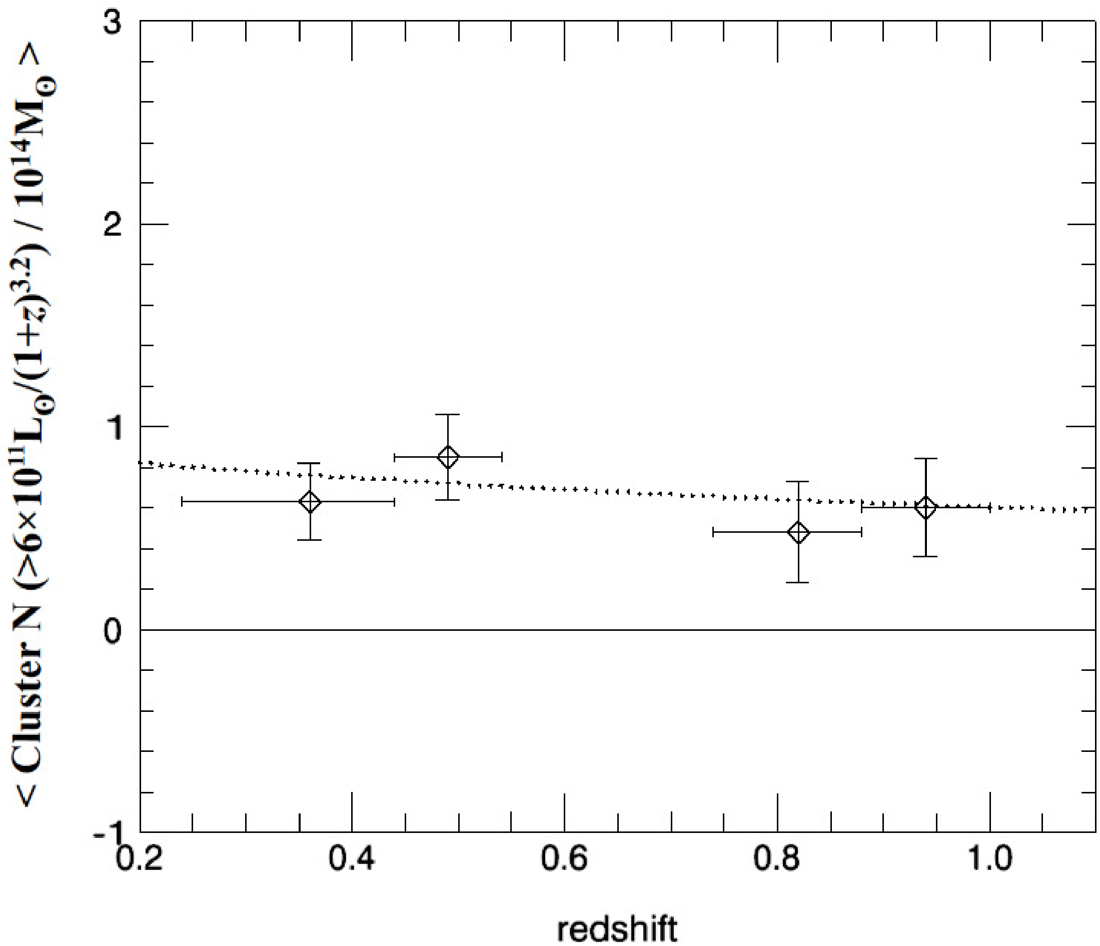

Figure 2.20 Same as figure 2.19 but within R_{200} of the cluster center. The dashed line represents the best power-law fit in the form of $N_{>}/\mathrm{M} \propto (1+z)^n$ with n = -0.6 $\pm$ 1.0 . Note that X error bars only present the redshift ranges of the bins and Y error bars correspond to the standard errors in the mean.

2.4.3 The Evolution of total SFR per unit Cluster Mass

In Section 2.4.2 we show that the observed Mid-IR luminosity is due to star forming galaxies and they follow the same evolution we see in the field. In this section we use the number counts in Section 2.4.1 to estimate total IR star formation rate ΣSFR of individual clusters within R_{200}. By using Le Floc'h et al. (2005) luminosity functions (relation 2.5), depending on the redshift of each cluster, we calculate the number density $\mathbf{n}_{L>6\times10^{11}L_\odot}$ and luminosity density $\mathbf{L}_{L>6\times10^{11}L_\odot}$ of field galaxies with L_{IR}>6×$10^{11}L_\odot$ as below :

$$\mathbf{n} = \int_{6\times10^{11}L_\odot}^{\infty} \phi_{IR}(L)dL \tag{2.8}$$

$$\mathbf{L} = \int_{6\times10^{11}L_\odot}^{\infty} L\phi_{IR}(L)dL \tag{2.9}$$

We then use these densities to estimate the total IR luminosity ΣL_{IR} for each cluster from its number count as below :

$$\frac{\mathbf{n}}{\mathbf{L}} = \frac{N(>6\times10^{11}L_\odot)}{\Sigma L_{IR}} \tag{2.10}$$

We convert ΣL_{IR} to integrated total star formation rate ΣSFR using the relation in Bell (2003) and then normalize it by cluster halo mass to estimate ΣSFR/M_{200}. Figure 2.21 and Figure 2.22 present the evolution of the mean ΣSFR/M_{200} over the redshift range, within 2Mpc and R_{200} of cluster center respectively and the best power-law fit in the form of ΣSFR/$M_{200} \propto (1+z)^n$ gives n = 8.6 ± 1.5 for R = 2 Mpc and n = 5.6 ± 0.5 for R_{200} (least-squares fitting method using Gnuplot). Note

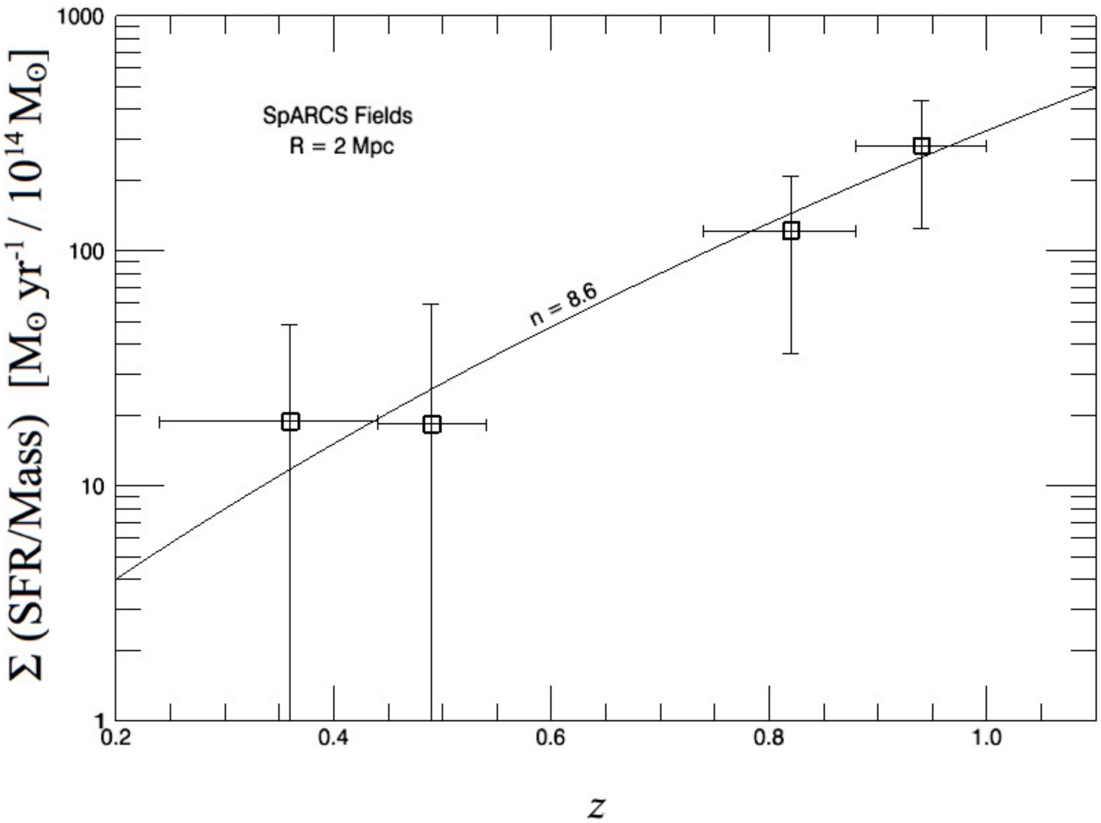

Figure 2.21 Averaged integrated total star formation rate per unit cluster mass $\Sigma\mathrm{SFR}/M_{200}$, within R = 2 Mpc from cluster center in four redshift bins. The solid line is the best power-law fit in the form of $\Sigma\mathrm{SFR}/M_{200} \propto (1+z)^n$ with n = 8.6 ± 1.5 . Note that X error bars only present the redshift ranges of the bins and Y error bars correspond to the standard errors in the mean.

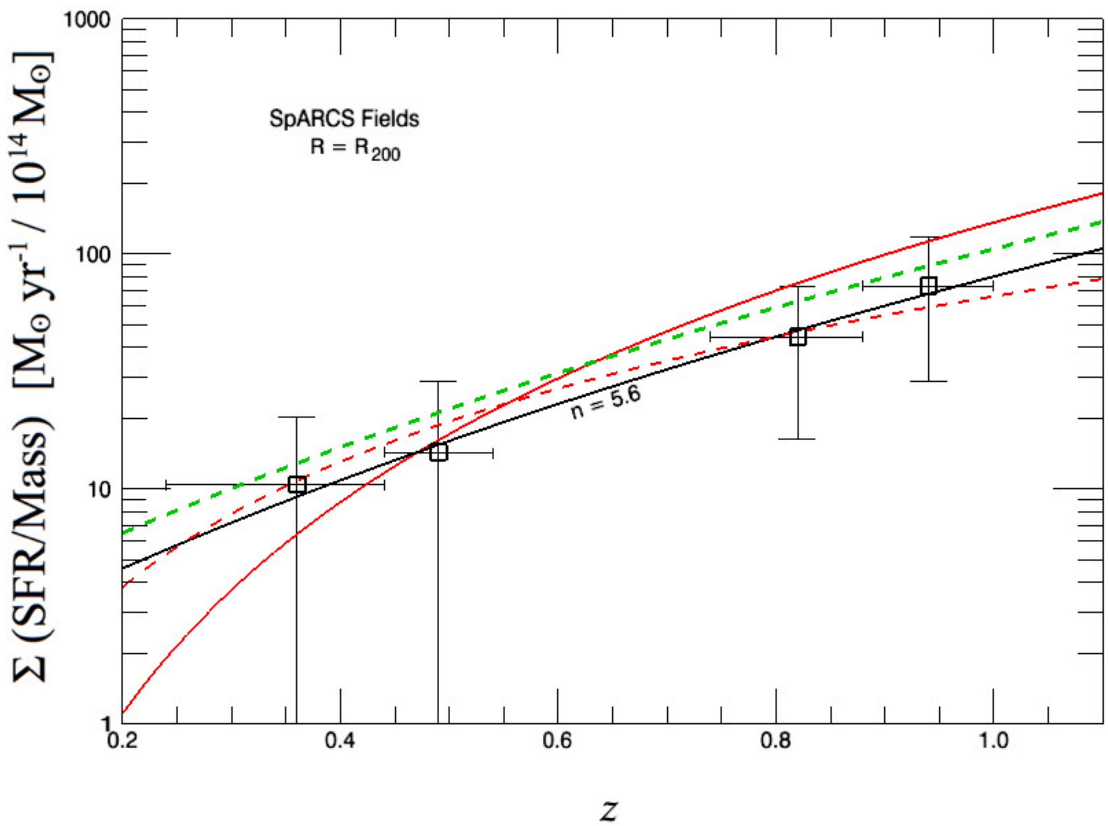

Figure 2.22 Same as figure 2.21 but within R_{200} from cluster center. The solid line is our best power-law fit in the form of $\Sigma\mathrm{SFR}/M_{200} \propto (1+z)^n$ with n = 5.6 ± 0.5 . The green dashed line is Webb et al. (2013) result with n = 5.4 and since it is very close its scaled fit to our data we just use the actual result here. The red dashed line is from Popesso et al. (2012) and the red line is its scaled fit to our data. Note that X error bars only present the redshift ranges of the bins and Y error bars correspond to the standard errors in the mean.

that the power n in these plots are nearly the same the power n in number count plots in Figure 2.16 and Figure 2.17 and show that they have the same evolution.

Popesso et al. (2012) accurately estimate $\Sigma\mathrm{SFR}/M_{200}$ for 9 massive clusters ($\sim 10^{15} M_{\odot}$) at this redshift range and show that the evolution of $\Sigma\mathrm{SFR}/M_{200}$ in clusters is much faster than the field. Dashed lines in Figure 2.22 show the results of Webb et al. (2013) (green) and Popesso et al. (2012) (red) and for comparison we scaled these fits to our average mass and IR depth. The red solid line is the scaled Popesso et al. (2012) fit and since the scaled Webb et al. (2013) fit is very close to itself, we show both of them with a green dashed line. Interestingly our power index is very close to Webb et al. (2013) with n = 5.4 . This is expected since we use the same method. Our fit is almost the same fit in Webb et al. (2013). The scaled relation of Popesso et al. (2012) fits to our low redshift clusters, however it does not fit our high redshift clusters perfectly and overestimates the data.

2.4.4 Radial Distribution of IR Luminous Galaxies

In Section 2.4.1, we have counted the number of IR luminous galaxies above the background within 0.5, 1.0, 1.5 and 2.0 Mpc from the cluster centers. In this section, we use these data to investigate the radial distribution by calculating the relative number density of these galaxies versus relative radius R/R_{200}. To calculate the relative number density, in two high and low redshift bins, we divide the number counts by relative area (= physical area/πR_{200}^2). Figure 2.23 presents our averaged results at 0.24 < z < 0.54 and 0.74 < z < 1.0. Although these results have poor statistics, some points are very important. As we expect, high redshift clusters have higher IR galaxy densities than low redshift clusters. Both high and low redshift bins show an increase toward the smaller radii and reveal the increase in star formation activities toward the cluster cores. In low redshift clusters, the density is almost zero beyond about 1.5 R_{200} and this reveals that clusters barely accrete new IR galaxies from the field at these redshifts. In high redshift clusters, we observe IR galaxies with flat radial distribution between 1.5 R_{200} and 2.5 R_{200}. As it shows, high redshift clusters were continually accreting IR galaxies from the field. Note that since our high redshift clusters have relatively lower R_{200} in comparison with low redshift clusters, we see different relative distance R/R_{200} bins in Figure 2.23. The average R_{200} of high redshift clusters is 0.8 Mpc while it is 1.0 Mpc for lower redshifts.

The results in Section 2.4.1 can be interpreted based on the radial distribution of IR galaxies. The number counts normalized by cluster mass evolve with $(1 + z)^{5.2}$

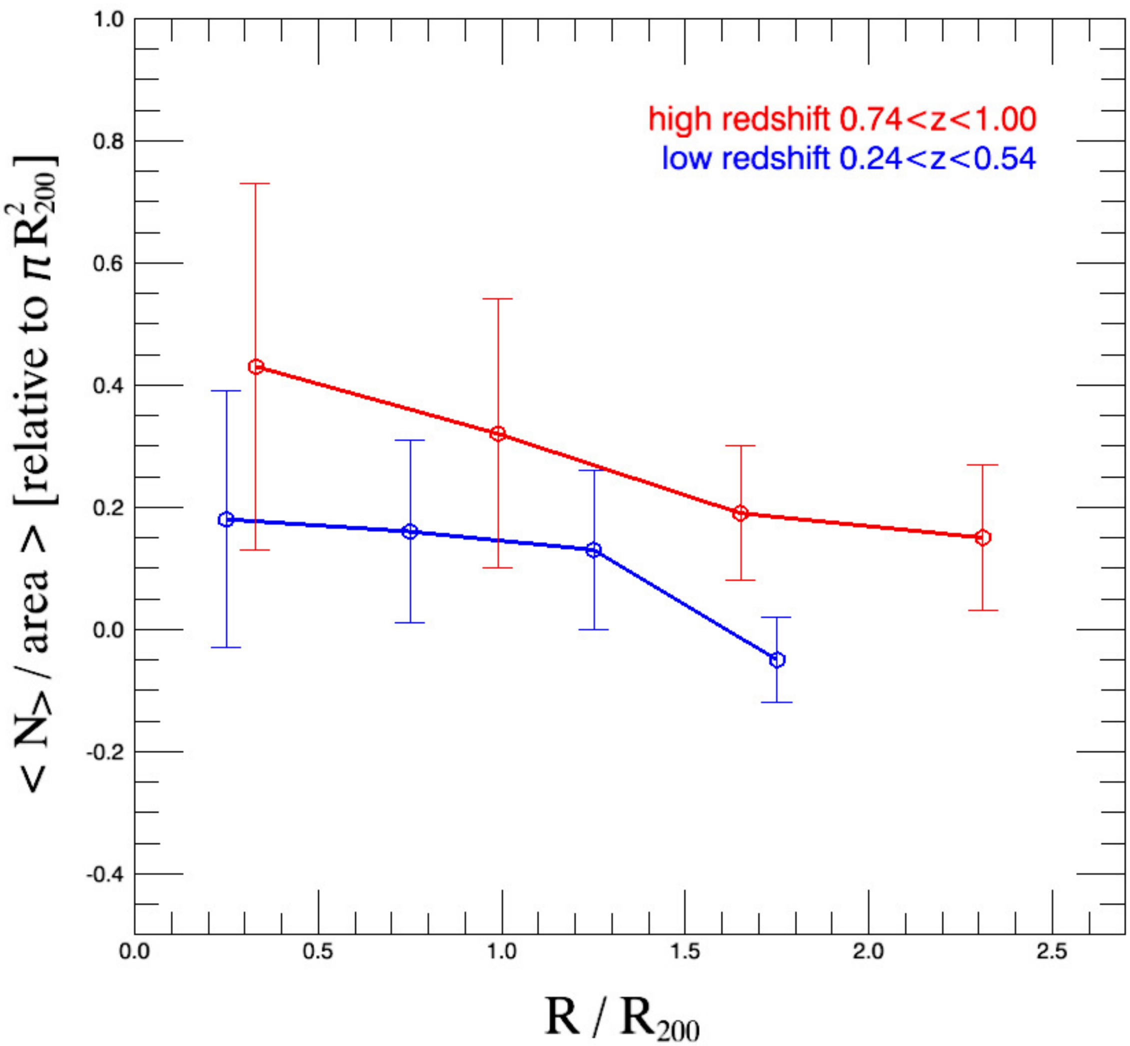

Figure 2.23 The surface density of the IR luminous galaxies in cluster-centric annuli. Y error bars correspond to the standard errors in the mean.

within R_{200} and with $(1 + z)^{9.6}$ within 2 Mpc. The distance of 2 Mpc is about $2\times<R_{200}>$ in low redshifts and $2.5\times<R_{200}>$ in high redshifts, where $<R_{200}>$ is the average R_{200} of the clusters at each redshift bin. According to Figure 2.23, in the low redshift clusters the surface density at distances beyond 1.5 R_{200} drops to zero and there should not be significant number of IR galaxies beyond that, therefore, we can consider their number counts within 2 Mpc as the number counts within 2.5 R_{200} from the cluster centers to match $2.5\times<R_{200}>$ of the high redshift clusters. So the relative number counts between R_{200} and 2 Mpc or between R_{200} and 2.5 R_{200} from cluster centers evolve as below:

$$< N_{>}/M_{200} >_{R_{200}} \propto (1+z)^{5.2\pm0.5} \tag{2.11}$$

$$< N_{>}/M_{200} >_{2.5\times R_{200}} \propto (1+z)^{9.6\pm1.6} \tag{2.12}$$

$$\frac{< N_{>} >_{2.5\times R_{200}}}{< N_{>} >_{R_{200}}} \propto (1+z)^{4.4\pm1.7} \tag{2.13}$$

Assuming R_{200} as the virial radius of a cluster, the number of IR luminous galaxies between R_{200} and 2.5 R_{200} (outskirts) relative to the number of these galaxies within R_{200} can be expressed as :

$$1 + \frac{< N_{>} >_{outskirt}}{< N_{>} >_{R_{200}}} \propto (1+z)^{4.4\pm1.7} \tag{2.14}$$

This relation expresses how fast the infalling IR galaxies in the outskirt of a galaxy cluster were being accreted. A study on the accretion rate of the galaxy clusters (McGee et al., 2009) shows that clusters of a given mass at higher redshift must assemble their mass more quickly, which is in agreement with our result.

Bibliography

Bell, E. F. 2003, ApJ, 586, 794

Chary, R., & Elbaz, D. 2001, ApJ, 556, 562

Dale, D. A., & Helou, G. 2002, ApJ, 576, 159

Haines, C. P., Smith, G. P., Egami, E., et al. 2009, ApJ, 704, 126

Le Floc'h, E., Papovich, C., Dole, H., et al. 2005, ApJ, 632, 169

Lu, T., Gilbank, D. G., Balogh, M. L., & Bognat, A. 2009, MNRAS, 399, 1858

McGee S. L., Balogh M. L., Bower R. G., Font A. S., McCarthy I. G., 2009, MNRAS, 400, 937

Popesso P. et al. 2012, A&A, 537, A58

Saintonge, A., Tran, K.-V. H., & Holden, B. P. 2008, ApJ, 685, L113

Shupe, D. L., Rowan-Robinson, M., Lonsdale, C. J., et al. 2008, AJ, 135, 1050

Webb, T., O'Donnell, D., Yee, H., Gilbank, D., Coppin, K., Ellingson, E., Faloon, A., Geach, J., Gladders, M., Noble, A., Muzzin, A., Wilson, G., Yan, R., 2013, AJ, 146, 84

Chapter 3

Spitzer IRAC Color-Color Diagrams: Classification of Spectroscopic Galaxies in Clusters at $z < 0.5$

3.1 Galaxy Cluster SpARCS J104101+581741

In Chapter 1, we spectroscopically confirmed nine galaxy clusters. According to Chapter 1, galaxy cluster SpARCS J104101+581741, with 9 members at $z = 0.072$ is the lowest redshift cluster of our sample with measured $R_{200} = 1.3 \pm 0.5$ Mpc, $M_{200} = 2.6 \times 10^{14}\ M_{\odot}$, and the line-of-sight rest-frame velocity dispersion $\sigma_v = 538 \pm 220$

kms^{-1}. The recent tenth SDSS Data Release (DR10) (Ahn et al., 2013) has covered the field of this cluster. We have found 48 new spectroscopically confirmed members and this increases the number of members in this cluster to 57. Using the method we explained in Section 1.4.1, we measured R_{200} = 1.42 ± 0.19 Mpc, M_{200} = (3.49 ± 1.41)×10^{14} $M_{\odot}$ and the line-of-sight rest-frame velocity dispersion σ_v = 595 ± 80 kms^{-1} more precisely. This cluster is at $z_{cluster}$ = 0.0726 ± 0.0003 and the average redshift of the members is $z_{average}$ = 0.0726 which is exactly the same redshift as the Brightest Cluster Galaxy (BCG). We consider the BCG as the center of this cluster. Since the BCG's redshift is same as the average redshift of the members, considering the BCG as the center of this system is a good assumption.

In table 3.1 we briefly report this cluster's properties and table 3.2 is photometric, redshift, and spectral type catalog of the members. In this catalog, the coordinates, z' magnitude, and IRAC photometric information are from SpARCS catalogs (Degroot et al. (in prep)) and redshifts are from Chapter 1 and SDSS DR10. To find the MIPS 24 μm flux of these galaxies, we matched this catalog to 24 μm source catalog of SWIRE fields (Shupe et al., 2008). Those undetected galaxies in MIPS 24 μm have no flux in table 3.2. For the new members, we measured the equivalent width of Hδ and [O II] features from their SDSS spectra and classify them based on MORPHS classification (Dressler et al., 1999) (Section 1.4.2.2). The Spectral types are either from SDSS DR10 or are classified based on our BPT diagrams and MORPHS clas-

Table 3.1. SpARCS J104101+581741 properties

Properties	
BCG R.A.	160.25442
BCG Dec.	58.29493
$z_{cluster}$	0.0726 ± 0.0003
$z_{average}$	0.0726
z_{BCG}	0.0726
Member	57
24 μm detected member	42
σ_v	595 ± 80 kms^{-1}
R_{200}	1.42 ± 0.19 Mpc
M_{200}	$(3.49 \pm 1.41) \times 10^{14} M_\odot$
Star forming	23
Passive	30
Post-starburst	1
AGN	3

Note. — σ_v is the line-of-sight rest-frame velocity dispersion.

Table 3.2. Photometric, Redshift and Spectral Type Catalog for SpARCS J104101+581741

ID	R.A.	Dec.	Redshift	Class	F_{24} [μJy]	z'	[3.6]	$\log(S_{8.0}/S_{4.5})$	$\log(S_{5.8}/S_{3.6})$
1	160.62444	58.38200	0.0666	SF,e(c)	639	18.09	18.42	0.53	-0.29
2	160.04846	58.03613	0.0676	SF,e(c)	564	18.65	19.18	0.65	-0.14
3	159.74431	58.37603	0.0690	SB, e(b)	20373	16.43	16.27	0.87	-0.05
4	160.58856	58.13136	0.0693	e(c)	426	-	18.84	0.44	-0.30
5	160.24507	58.28425	0.0699	AGN,SF,QSO	10677	17.10	16.77	0.36	0.19
6	160.10104	58.15506	0.0700	SB, e(b)	4363	17.20	16.55	0.71	-0.08
7	160.48073	58.11477	0.0701	e(c)	834	17.83	18.10	0.55	-0.22
8	160.47704	58.24948	0.0702	k	251	15.97	16.27	-0.28	-0.32
9	160.93907	58.15288	0.0707	e(c)	994	18.36	17.94	0.70	-0.12
10	160.20415	58.34975	0.0710	k	-	16.95	17.31	-0.36	-0.33
11	160.23210	58.30442	0.0710	Passive	188	16.50	16.75	-0.17	-0.34
12	160.82101	58.23691	0.0710	k	-	16.86	17.24	-0.32	-0.35
13	159.88904	58.36202	0.0711	k	-	16.44	16.41	-0.07	-0.33
14	160.64975	58.58961	0.0713	k	-	17.15	17.46	-0.34	-0.38
15	160.89716	58.10629	0.0715	k	349	15.72	15.94	-0.34	-0.32
16	160.78673	58.14848	0.0715	k	549	16.62	16.93	-0.30	-0.32
17	159.83186	58.31490	0.0716	k	523	16.34	16.55	0.00	-0.31

Table 3.2—Continued

ID	R.A.	Dec.	Redshift	Class	F_{24} [μJy]	z'	[3.6]	$\log(S_{8.0}/S_{4.5})$	$\log(S_{5.8}/S_{3.6})$
18	160.41621	58.31722	0.0716	k	1930	16.14	16.12	0.25	-0.26
19	160.91536	58.06912	0.0716	k	-	17.04	17.39	-0.33	-0.34
20	160.16212	58.33630	0.0718	SF, Seyfert	1241	18.30	18.31	0.92	-0.06
21	160.33966	58.20194	0.0719	k	386	17.77	18.04	0.27	-0.31
22	160.35614	58.40980	0.0720	k	963	16.95	17.04	0.27	-0.29
23	160.06532	58.43799	0.0722	k	-	17.21	17.55	-0.36	-0.40
24	160.92297	58.10228	0.0722	k	-	16.44	16.74	-0.34	-0.36
25	159.63919	58.26009	0.0723	k	356	17.40	17.63	0.27	-0.31
26	159.76376	58.33225	0.0724	k	200	16.63	16.90	-0.33	-0.33
27	161.12833	58.16055	0.0725	k	-	17.29	17.66	-0.33	-0.34
28	160.56898	58.10541	0.0726	SF,e(c)	893	17.49	17.84	0.55	-0.20
29	160.25442	58.29493	0.0726	Ell , BCG	380	15.92	16.17	-0.31	-0.32
30	160.62018	58.33945	0.0727	k	313	15.91	16.11	-0.22	-0.31
31	160.14742	58.00487	0.0728	e(c)	-	17.10	17.45	-0.32	-0.36
32	159.78502	58.23114	0.0729	e(c)	2902	16.61	16.81	0.21	-0.11
33	160.12242	58.16778	0.0732	SF,e(c)	1833	16.91	17.05	0.51	-0.19
34	160.56987	58.36087	0.0732	e(c)	508	17.12	17.36	0.22	-0.28

Table 3.2—Continued

ID	R.A.	Dec.	Redshift	Class	F_{24} [μJy]	z'	[3.6]	$\log(S_{8.0}/S_{4.5})$	$\log(S_{5.8}/S_{3.6})$
35	159.87878	58.12532	0.0732	k	-	-	16.92	-0.30	-0.29
36	160.18411	58.28239	0.0733	e(c)	-	16.47	16.78	-0.33	-0.36
37	160.20708	58.25691	0.0733	k	575	16.47	16.64	-0.07	-0.30
38	160.95203	58.19658	0.0733	SF, e(n)	6133	16.51	16.47	0.44	-0.07
39	159.77425	58.36163	0.0733	k	-	16.94	17.15	-0.14	-0.34
40	161.14621	58.29416	0.0734	SB, e(b)	862	18.31	18.70	0.86	-0.06
41	160.61819	58.33983	0.0739	k	-	16.98	17.62	-0.34	-0.32
42	160.26678	58.26315	0.0739	e(c)	1080	17.53	17.75	0.51	-0.21
43	159.84743	58.34779	0.0739	e(c)	1855	17.70	17.78	0.60	-0.15
44	160.36899	58.35627	0.0740	k	-	16.75	17.15	-0.37	-0.39
45	160.76416	57.99533	0.0741	SB, e(b)	2550	17.91	17.96	0.95	-0.02
46	159.91118	57.93356	0.0744	e(c)	882	15.93	16.15	-0.14	-0.32
47	159.70488	58.16049	0.0746	e(c)	684	17.66	17.86	0.40	-0.23
48	160.65347	57.85717	0.0746	SB, e(b)	457	18.27	18.94	0.53	-0.25
49	160.51933	58.17895	0.0746	k+a	-	16.97	17.36	-0.29	-0.37
50	160.58452	58.20798	0.0748	k	651	15.77	15.87	-0.13	-0.34
51	160.05849	58.31596	0.0748	k	199	16.23	16.61	-0.35	-0.34

Table 3.2—Continued

ID	R.A.	Dec.	Redshift	Class	F_{24} [μJy]	z'	[3.6]	$\log(S_{8.0}/S_{4.5})$	$\log(S_{5.8}/S_{3.6})$
52	159.73135	58.33435	0.0751	SF,e(c)	1322	17.90	18.19	0.66	-0.13
53	159.89868	57.98545	0.0752	SF,e(c)	4992	16.74	16.72	0.73	-0.13
54	160.15352	58.29995	0.0759	Ell	162	16.86	17.16	-0.28	-0.33
55	160.77135	58.05380	0.0765	k	4463	-	16.52	0.33	-0.26
56	160.15352	58.29995	0.0771	k	162	16.86	17.16	-0.28	-0.33
57	160.81296	58.34097	0.0773	SF,e(c)	3310	17.34	17.11	0.87	-0.05

Note. — Coordinates are in J2000 epoch. The MORPHS spectral types in column 5 are classified by us in this work (See Section 1.4.2.2 and Table 1.16). The other spectral types are from either our BPT diagrams or SDSS. Column 6, 7 and 8 are MIPS 24μm flux in μJy, the magnitude in z' band (AB) and the total magnitude in IRAC 3.6μm band (AB). Column 9 and 10 are IRAC channels' flux ratios. The uncertainties in column 6 and 8 are ~ 20 μJy and ~ 0.10 . The uncertainties in column 9 and 10 are ~ 0.06 .

sification . Figure 3.1 presents the color-magnitude diagram for this cluster and the red-sequence of early-type galaxies is seen in it.

In Figure 3.2, the spectroscopic redshift distribution of the members is presented. The redshift bins were optimized by Scott's normal rule and the best gaussian fit is shown by red solid line. Note that Scott's normal reference rule is optimal for random samples of normally distributed data, in the sense that it minimizes the integrated mean squared error of the density estimate.

The velocity of each member relative to the mean cluster velocity is calculated using relation 1.1 in Section 1.4.1 and is presented as a function of clustercentric distance in Figure 3.3. The position of each member is presented in Figure 3.4. Photometric detected objects around the BCG, and its *rig* image (SDSS *r, i and g* bands), are presented in Figure 3.5 and Figure 3.6.

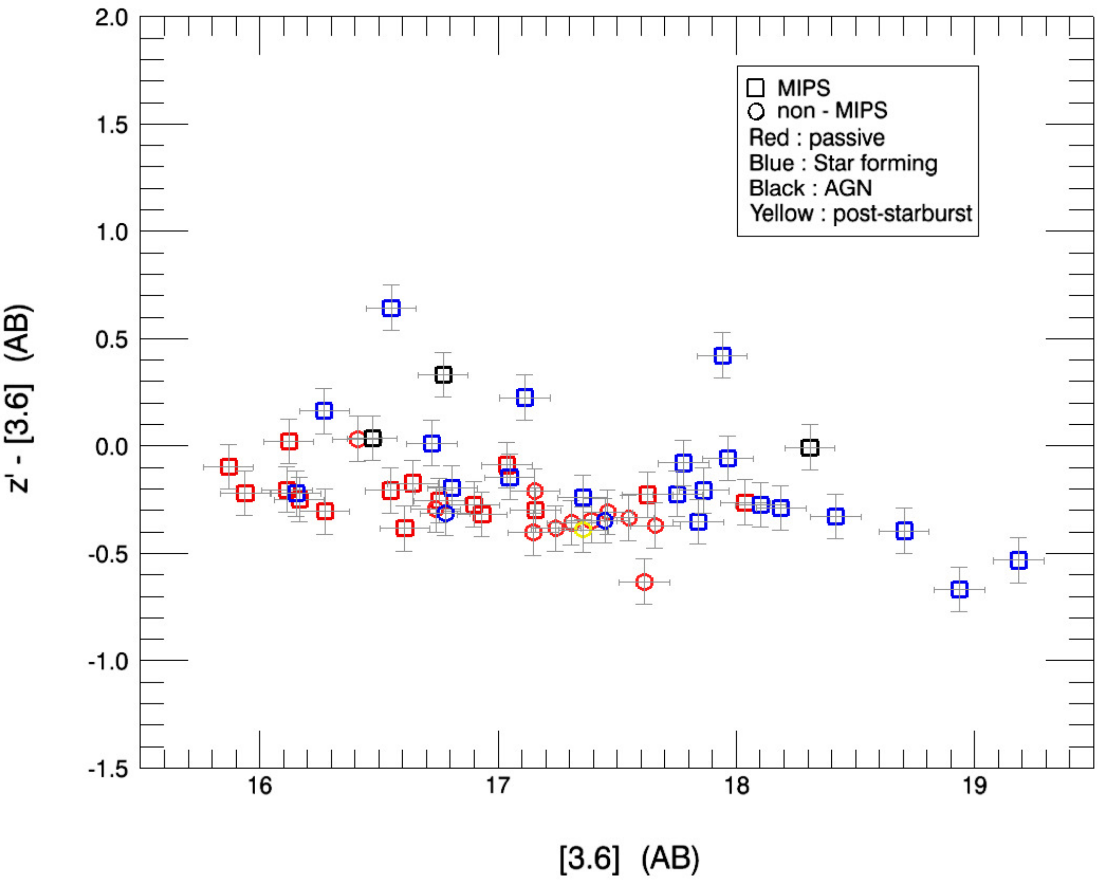

Figure 3.1 The color-magnitude diagram for SpARCS J104101+581741. The boxes are the MIPS 24 μm detected galaxies and circles are the undetected galaxies. Passive galaxies are in red, active star forming galaxies are in blue, post-starbursts are in yellow and AGNs are in black.

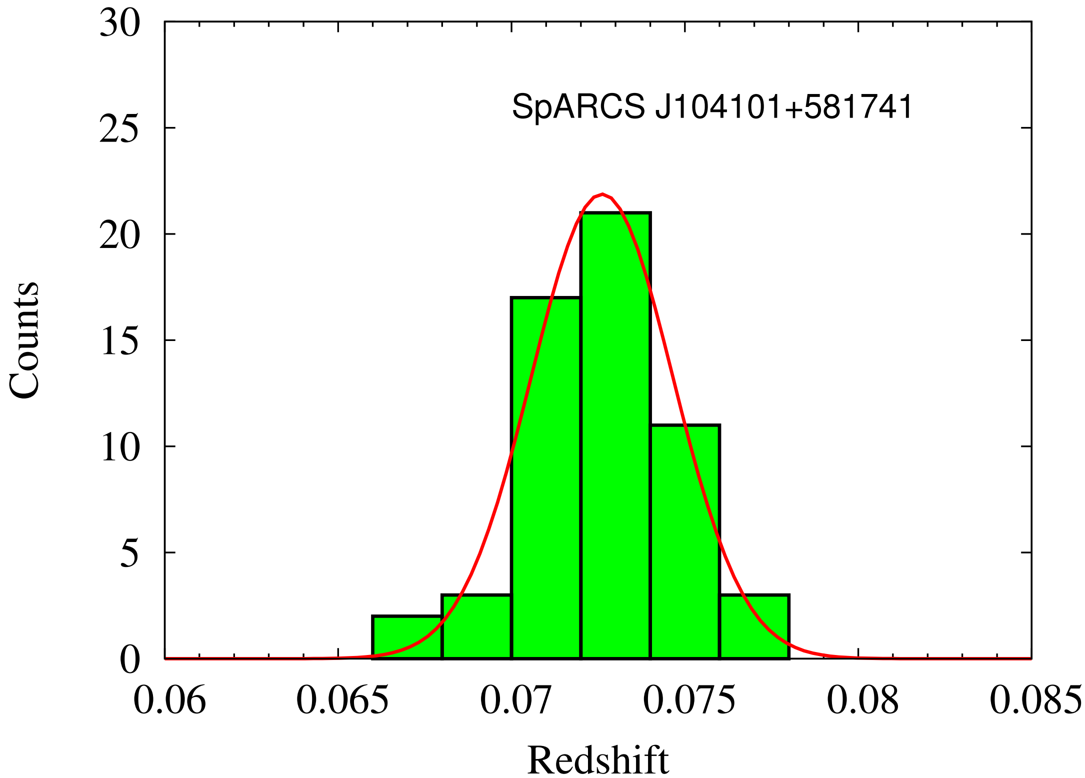

Figure 3.2 The histogram of spectroscopic redshifts in SpARCS J104101+581741. The redshift bins were optimized by Scott's normal rule and the best gaussian fit is shown by red solid line.

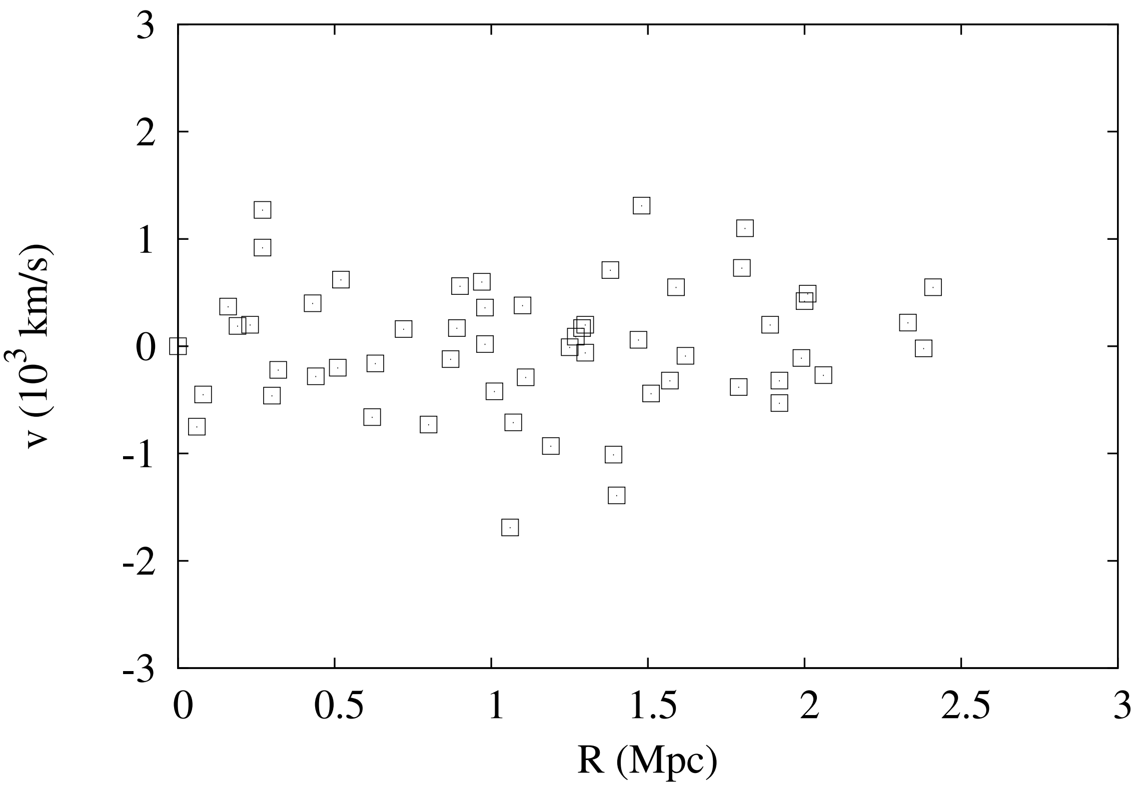

Figure 3.3 The velocity of each member relative to the mean cluster velocity as a function of clustercentric distance .

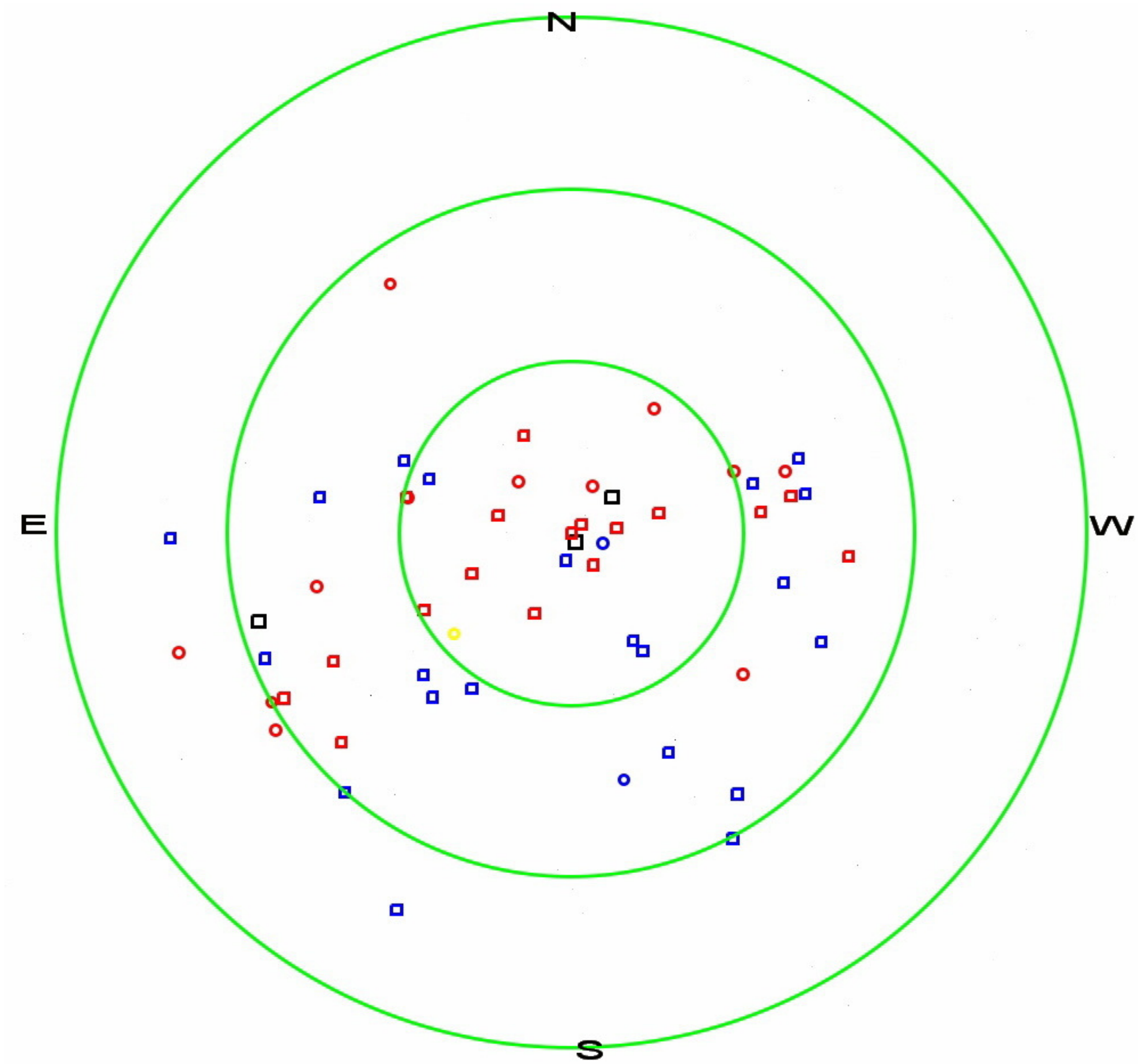

Figure 3.4 The position of cluster members in SpARCS J104101+581741. The BCG is at the center and green solid lines represent 1, 2 and 3 Mpc distance from the center. The boxes are the MIPS 24 μm detected galaxies and circles are the undetected galaxies. Passive galaxies are in red, active star forming galaxies are in blue, post-starbursts are in yellow and AGNs are in black. 1 Mpc at cluster's redshift is about 12 arc minutes.

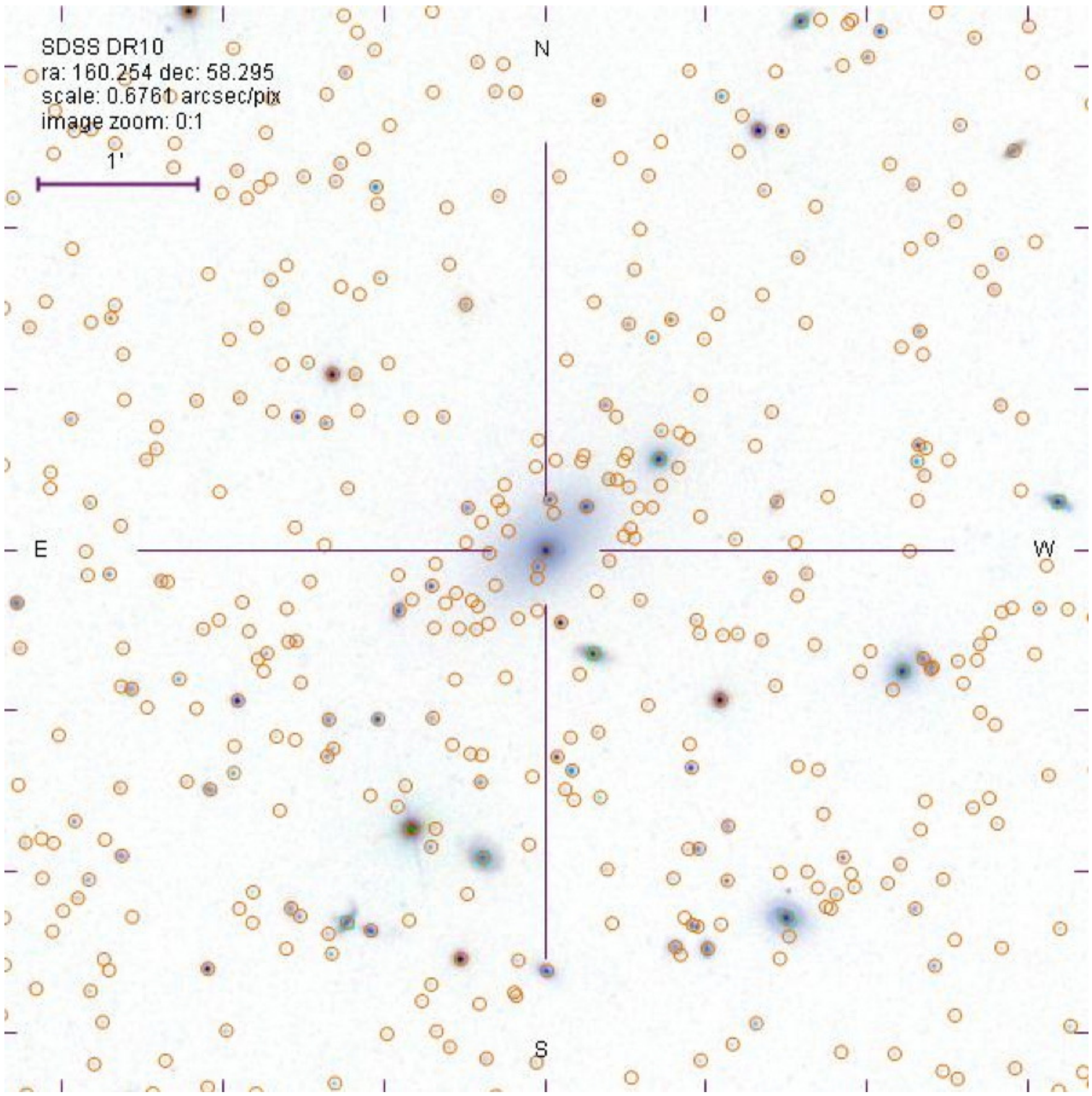

Figure 3.5 The BCG of SpARCS J104101+581741 at $z = 0.0726$ is the center of this cluster. This image from SDSS DR10 present all photometric detected objects around this galaxy.

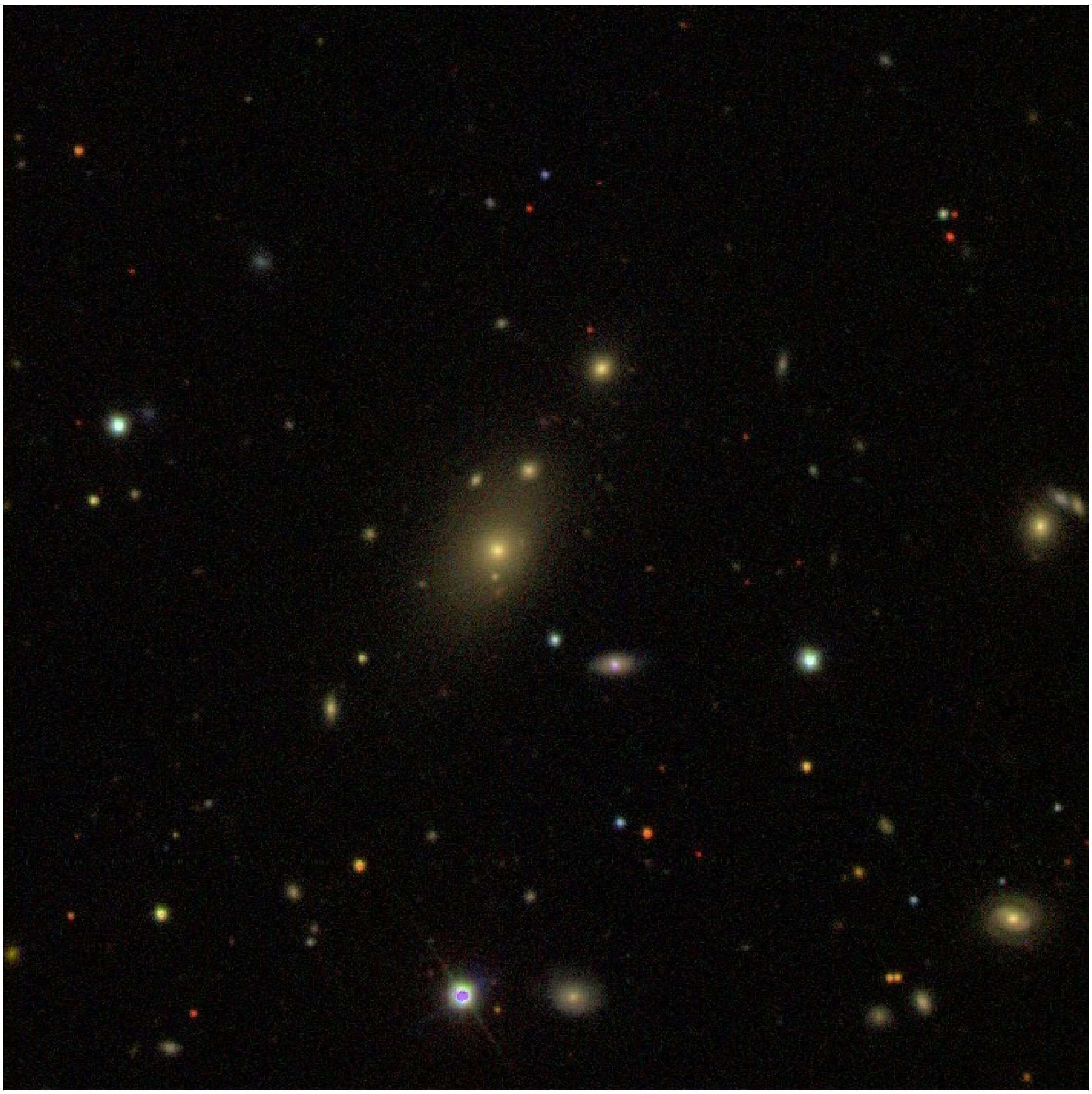

Figure 3.6 The BCG of SpARCS J104101+581741 in SDSS r, i *and* g bands.

3.2 *Spitzer* IRAC Color-Color Diagram

Infrared Array Camera (IRAC) is a near-infrared camera on board on *Spitzer* Space Telescope. This instrument operates simultaneously on four wavelengths 3.6, 4.5, 5.8 and 8 μm. This covered band by IRAC (3.6 - 8 μm) is the interference between the direct stellar light and the reproduced light by dust and gas, therefore the IRAC color-color diagram ($S_{5.8}/S_{3.6}$ versus $S_{8.0}/S_{4.5}$) can be used as a strong tool to identify the nature of the near-infrared light sources even if their redshift is unknown. The main contributors in this band are old stellar populations, light from polycyclic aromatic hydrocarbon (PAH) emission lines and power-law continuum emission (AGNs).

Sajina et al. (2005) used a simple parametrization of the near-infrared spectra of a wide range of galaxy types in order to predict their distribution in the IRAC color-color diagram. In this model, the SED of any galaxy can be represented by a combination of direct stellar emission, PAH emission, and a power-law continuum. Fitting the observed spectra of a range of galaxy types with this model using the Markov chain Monte Carlo approach provides the probability distribution of each parameter. The power-law continuum (increasing spectrum in wavelength) of continuum dominated galaxies put them in high $S_{5.8}/S_{3.6}$ and $S_{8.0}/S_{4.5}$ regions of this diagram and the decreasing spectrum (in wavelength) of old stars in stellar dominated galaxies put them in low $S_{5.8}/S_{3.6}$ and $S_{8.0}/S_{4.5}$ regions of this diagram. In the PAH-dominated galaxies, depending on their redshifts, the PAH features enter and leave the IRAC passbands and put these galaxies in different regions in the IRAC color-color diagram. In the next sections we plot this diagram for the galaxies in clusters and the field at different redshifts and study their MORPHS spectral types on this diagram.

3.3 *Spitzer* IRAC Color-Color Diagram for Cluster SpARCS J104101+581741 at $z = 0.0726$

We matched the catalog of cluster SpARCS J104101+581741 to our SpARCS five-passband (IRAC 3.6, 4.5, 5.8, 8.0μm and z') source catalogs (Degroot et al. (in prep)) to plot IRAC color-color diagram. According to the segmentation in IRAC color-color diagram of Sajina et al. (2005), we divided the galaxies into three categories of Continuum dominated (AGN), PAH dominated and, Stellar dominated galaxies. In this cluster's catalog (table 3.2), we classify the galaxies based on MORPHS classification (Dressler et al., 1999) (see Section 1.4.2.2). This classification is based on the equivalent widths of the O II emission line and the Hδ absorption line. Both of these spectral features are the best indicators of ongoing and recent star formation. This classification classifies the galaxies into Star forming (e(c), e(a), and, e(b)), Passive (k), Poststarbursts (k+a and a+k) and AGN (e(n)) (see Table 1.16). In this work, the idea is comparing the spectroscopic classification of MORPHS with the photometric classification of Sajina et al. (2005).

Figure 3.7 presents the IRAC color-color diagram for the members of SpARCS J104101+581741. In this plot, according to the segmentation in Sajina et al. (2005), the upper-left section corresponds to very low redshift ($z < 0.3$) star forming galaxies, the upper-right is AGN section (continuum dominated), lower-right is the section for stellar (passive galaxies) and PAH dominated galaxies at high redshifts ($z > 1.6$) and lower-left is the section for stellar (passive galaxies) and PAH dominated galaxies at low redshifts.

Figure 3.7 shows a strong agreement between the spectroscopic classification of MORPHS and the photometric classification of Sajina et al. (2005) at $z \sim 0.07$. All the AGNs in our sample are identified through their broadlines or BPT diagrams. In the upper-right section (the AGN section) we have two out of three of the identified AGNs (ID# 5 and 38 in table 3.2). The third AGN, ID# 20, is an identified Seyfert through BPT diagrams, but it has been located in the upper-left section of the figure (star forming section). ID# 32 is a normal star forming galaxy (e(c)) which has been located in the AGN section of the figure.

In the upper-left section (star forming galaxies) of Figure 3.7 a clear sequence of star forming galaxies is seen. All of these galaxies have been detected in 24 μm and they make a sequence from 24 μm-bright passive galaxies to normal star forming galaxies and then to starbursts. In cluster SpARCS J104101+581741 we identified 18 normal star forming galaxies (e(c)) and 5 starbursts (e(b)) as star forming galaxies. It is interesting that we did not detect any dusty starburst galaxy, e(a), in this cluster.

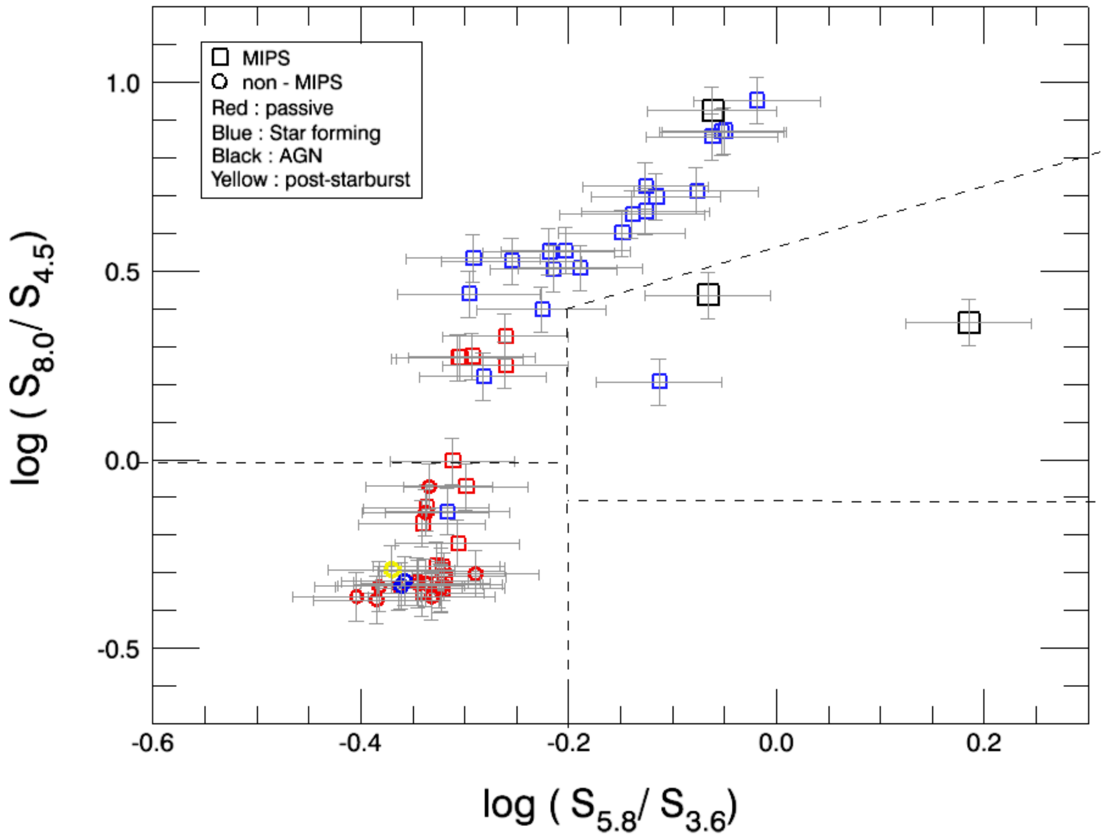

Figure 3.7 *Spitzer* IRAC Color-Color Diagram for Cluster SpARCS J104101+581741 at $z = 0.0726$. The boxes are the MIPS 24 μm detected galaxies and circles are the undetected galaxies. Passive galaxies are in red, active star forming galaxies are in blue, post-starbursts are in yellow and AGNs are in black. According to Sajina et al. (2005), the upper-left section corresponds to low redshift ($z < 0.3$) PAH dominated galaxies, the upper-right is AGN section (continuum dominated), lower-right the section for stellar and PAH dominated galaxies at high redshifts ($z > 1.6$) and lower-left is the section for stellar and PAH dominated galaxies at low redshifts.

Figure 3.8 only presents the star forming galaxies of the previous plot. We see that in the IRAC color-color diagram, star forming galaxies make a sequence from 24 μm-faint normal star forming galaxies (or 24 μm-bright passive) to 24 μm-bright and then to starbursts.

Figure 3.9 zooms the lower-left section of Figure 3.7. Stellar and PAH dominated galaxies are in this section. Among 30 cluster members detected as passive galaxies, 26 galaxies (87%) are in this section. Also, all 24 μm-faint members are in this section and make a concentrated region. The 24 μm-bright passive galaxies, along with the 24 μm-faint star forming galaxies, tend to follow the sequence of star forming galaxies from this concentrated region of early-type galaxies. Also ID# 49, the only detected post-starburst in this cluster, lies in this region.

3.4 *Spitzer* IRAC Color-Color Diagram for Galaxies in Clusters and in the Field at $z < 0.5$

In this section, we plot the IRAC color-color diagram for the members in the other three clusters in the SWIRE fields from Chapter 1 : SpARCS J022258-040715 (z = 0.288), SpARCS J021528-044041 (z = 0.353) and SpARCS J104209+575350 (z = 0.487) (See table 1.8, 1.9 and 1.10). In total there are 26 members in these galaxy clusters (table 3.3). To make a sample of field galaxies comparable to our cluster

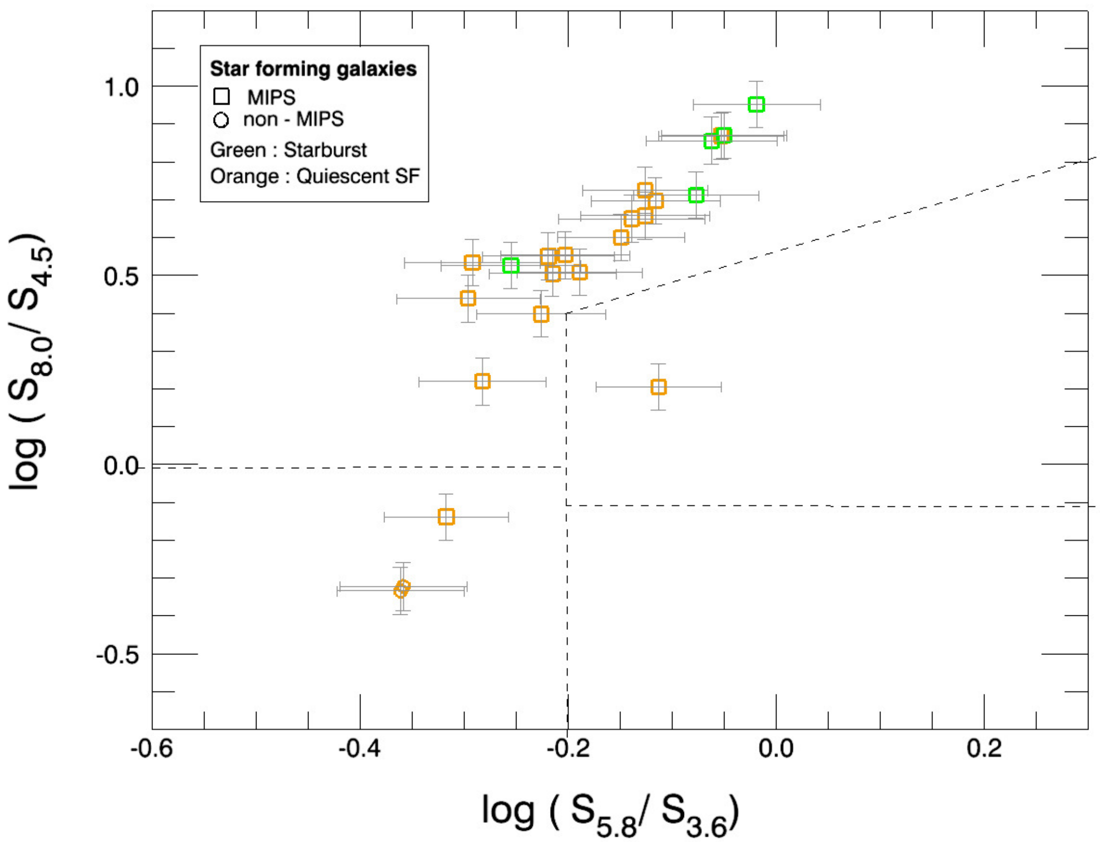

Figure 3.8 Same as figure 7 but for active star forming galaxies. Starbursts (*e(b)*) are in green and Quiescent (normal) star forming galaxies (*e(c)*) are in orange. Note that in MORPHS classification normal star forming galaxies are labeled as quiescent star forming galaxies (Dressler et al., 1999) (See Section 1.4.2.2 and Table 1.16).

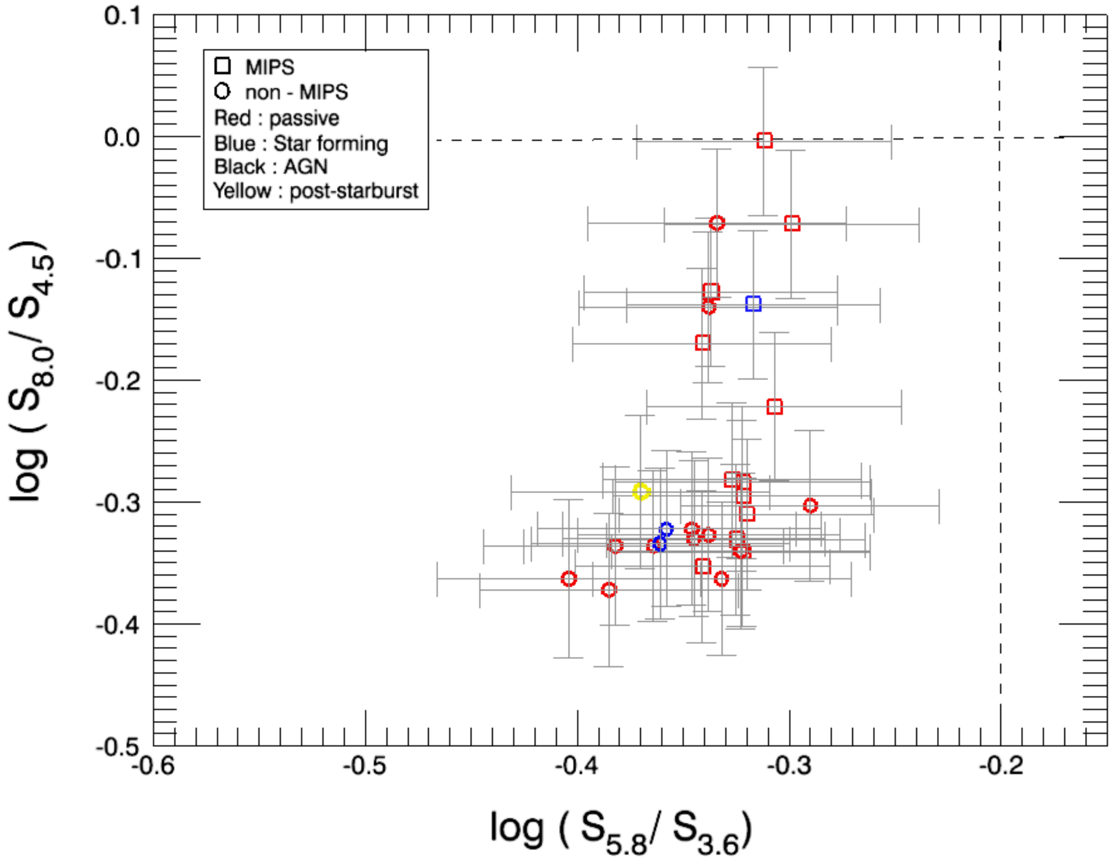

Figure 3.9 A zoom-in of the lower-left region of Figure 7.

Table 3.3. Photometric, Redshift and Spectral Type Catalog for the members of SpARCS J022258-040715, SpARCS J021528-044041 and SpARCS J104209+575350

ID	R.A.	Dec.	Redshift	Class	F_{24} [μJy]	[3.6]	$\log(S_{8.0}/S_{4.5})$	$\log(S_{5.8}/S_{3.6})$
1	33.85736	-4.70205	0.3514	SF, e(a)	303	19.95	0.17	-0.33
2	33.86019	-4.67546	0.3508	k	-	19.50	-1.07	-0.20
3	33.86757	-4.67812	0.3462	k	315	17.42	-0.49	-0.28
4	33.87223	-4.68195	0.3495	k	-	18.20	-0.58	-0.23
5	33.87399	-4.67971	0.3572	k+a	375	18.33	-0.63	-0.28
6	33.88244	-4.66522	0.3556	k	946	18.59	0.20	-0.11
7	33.88952	-4.68907	0.3588	k	468	19.57	-0.02	-0.31
8	33.90405	-4.67940	0.3510	k	228	18.53	-0.28	-0.35
9	33.92080	-4.71598	0.3544	k	-	19.46	-0.44	-0.33
10	33.92888	-4.72418	0.3554	k	1109	18.56	0.14	-0.03
11	33.97503	-4.67478	0.3565	k	-	18.99	-0.44	-0.43
12	35.70670	-4.07833	0.2888	e(c)	1026	17.79	-0.12	-0.10
13	35.73036	-4.11694	0.2888	k	-	19.53	-0.48	-0.40
14	35.73452	-4.10968	0.2896	k	-	18.31	-0.50	-0.27
15	35.73729	-4.13154	0.2880	k	-	19.15	-0.73	-0.49
16	35.75026	-4.11926	0.2864	k	-	19.16	-0.61	-0.69

Table 3.3—Continued

ID	R.A.	Dec.	Redshift	Class	F_{24} [μJy]	[3.6]	$\log(S_{8.0}/S_{4.5})$	$\log(S_{5.8}/S_{3.6})$
17	35.75901	-4.09267	0.2847	k	289	19.27	-0.04	-0.57
18	35.77528	-4.10599	0.2863	SF, e(b)	663	19.60	0.28	-0.12
19	35.79328	-4.10123	0.2894	SF, e(a)	767	18.93	0.24	-0.21
20	35.82792	-4.07131	0.2891	e(c)	438	17.98	-0.10	-0.18
21	160.38460	57.84986	0.4924	e(c)	784	19.34	0.20	-0.05
22	160.42569	57.86704	0.4784	a+k	294	19.07	-0.08	-0.37
23	160.54018	57.89741	0.4905	k	-	18.04	-0.44	-0.24
24	160.55391	57.89756	0.4820	k	-	18.67	-0.35	-0.27
25	160.55428	57.91573	0.4893	k	-	19.10	-0.02	-0.36
26	160.58777	57.89862	0.4893	k	-	18.94	-0.34	-0.34

Note. — Same as Table 3.2 but for the members of SpARCS J022258-040715, SpARCS J021528-044041 and SpARCS J104209+575350.

sample, we use the 24 identified foreground/background galaxies in the fields of these clusters at $z < 0.5$ (table 3.4).

In the same fashion as the analysis performed in Section 3.3, we present the IRAC color-color diagram for the members in these three clusters in Figure 3.10. All of 24 μm-faint galaxies and post-starburst galaxies are in the lower-left section of the plot (same as what we see in Figure 3.7). All early-type and passive galaxies lie in this section which has no star forming galaxies present. The lower-right region of the plot is empty. Unlike Figure 3.7, star forming galaxies are spread in upper sections and most of them are in the AGN section.

In Figure 3.11 we present the IRAC color-color diagram for the field galaxies at z < 0.5 . Upper sections do not separate AGNs (or Composites) from pure star forming galaxies. The only identified field QSO (ID# 2 in table 3.4) is located in upper-right and it is what we expect from its continuum-dominated spectrum, however the rest of our AGNs, along with pure star forming galaxies, are spread in the upper sections. Note that with the exception of the only QSO, all other AGNs in this sample are composites and Seyferts. Since their spectra look like star forming spectra, they can not be classified in this continuum-dominated part of the color-color diagram.

As the color evolution diagrams based on the simulations in Sajina et al. (2005) show, star forming galaxies are spread in the diagram at higher redshifts and the observed sequence in Figure 3.8 is only for the lower redshifts. At higher redshifts, PAH emission lines spread star forming galaxies in these four sections on IRAC color-

Table 3.4. Photometric, Redshift and Spectral Type Catalog for the field galaxies.

ID	R.A.	Dec.	Redshift	Class	F_{24} [μJy]	[3.6]	$\log(S_{8.0}/S_{4.5})$	$\log(S_{5.8}/S_{3.6})$
1	33.81490	-4.67687	0.1371	SF	348	20.21	0.34	-0.74
2	33.81547	-4.63557	0.0413	SF, e(n), QSO	10423	18.11	0.52	0.14
3	33.83600	-4.71398	0.2902	e(c)	285	19.03	-0.03	0.96
4	33.89537	-4.65351	0.3409	k	-	18.92	-0.73	-0.30
5	34.73731	-3.84519	0.2249	SF	3226	19.40	0.67	0.25
6	34.74628	-3.81911	0.1279	SF, e(c)	961	18.60	0.67	-0.22
7	35.44691	-3.78219	0.1990	e(b)	303	18.66	0.13	-0.47
8	35.47009	-3.74885	0.5951	k	374	18.52	0.35	-0.26
9	35.47078	-3.80965	0.4259	e(c)	340	18.54	-0.26	-0.30
10	35.68272	-4.10897	0.1013	Composite, SF	1290	17.85	0.60	-0.12
11	35.76865	-4.16036	0.2710	k	673	18.43	0.10	-0.26
12	35.82383	-4.13609	0.1491	Composite, Seyfert, e(a)	457	18.85	0.61	-0.18
13	160.12114	58.32009	0.3076	SF	832	18.73	0.32	-0.21
14	160.13600	58.27993	0.1321	SF	-	17.23	0.26	-0.29
15	160.29755	58.27360	0.2302	AGN, Seyfert, e(a)	841	19.46	0.50	-0.09
16	160.35872	58.28945	0.2307	AGN, Seyfert, e(c)	3558	17.89	0.65	-0.03
17	160.38048	57.91756	0.4268	e(a)	239	19.55	0.03	-0.01

Table 3.4—Continued

ID	R.A.	Dec.	Redshift	Class	F_{24} [μJy]	[3.6]	$\log(S_{8.0}/S_{4.5})$	$\log(S_{5.8}/S_{3.6})$
18	160.40965	57.89880	0.2864	Composite, SF, e(a)	343	19.68	0.21	-0.15
19	160.42108	57.93959	0.1524	SF, e(c)	399	18.98	0.63	-0.32
20	160.52074	57.95263	0.1990	SF	591	19.01	0.62	-0.29
21	160.58771	57.89868	0.3196	e(b)	-	18.94	-0.34	-0.34
22	160.65347	57.85717	0.0735	AGN, Seyfert, e(a)	457	18.94	0.53	-0.25
23	160.66849	57.84680	0.3341	k	827	18.30	0.15	-0.25
24	160.69498	57.86621	0.1819	Composite, Seyfert	394	19.82	0.59	-0.42

Note. — Same as Table 3.2 but for for the field galaxies.

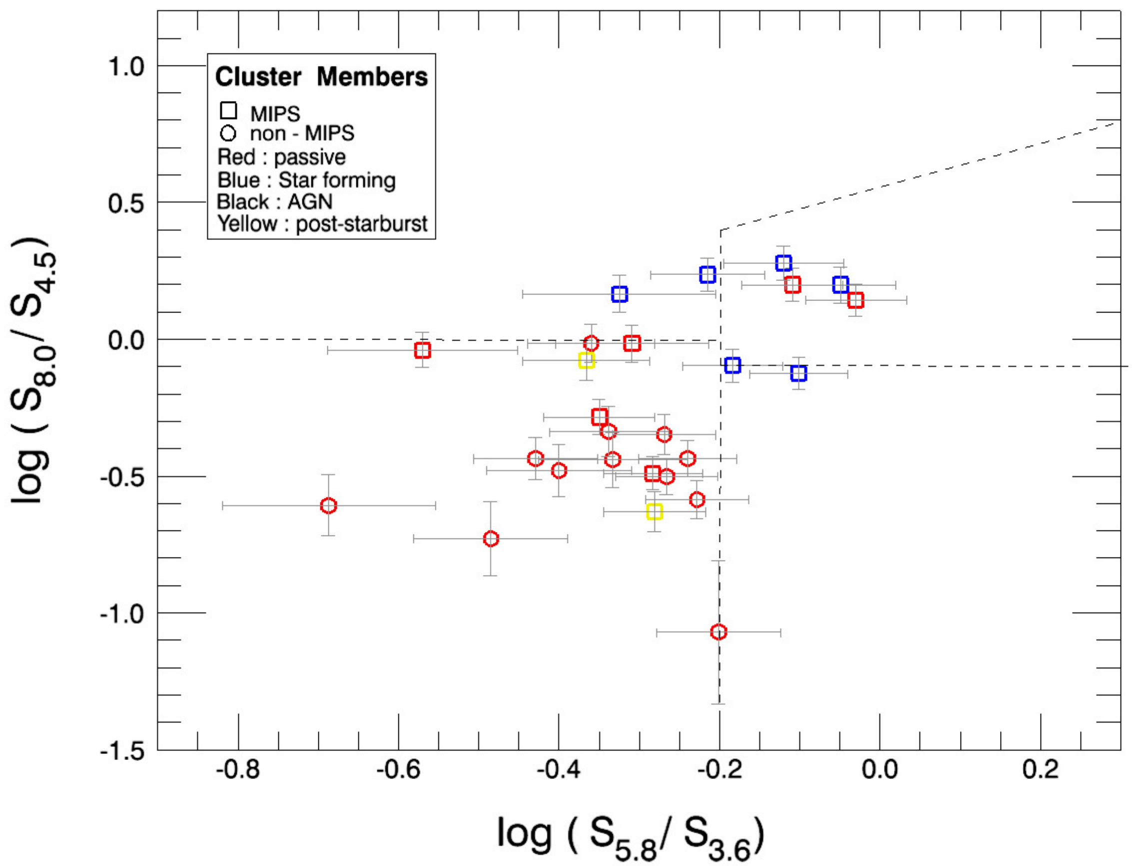

Figure 3.10 *Spitzer* IRAC Color-Color Diagram for cluster members.

color diagram by entering and leaving IRAC filters. Although continuum-dominated galaxies lie in upper-right section at any redshift, the presence of PAH emission lines of star forming galaxies in IRAC bands put them in this section and make star forming galaxies indistinguishable from continuum-dominated galaxies. The 24 μm-bright passive galaxies are seen in the same region as Figure 3.7. The 24 μm flux from these passive galaxies is puzzling and continues to be an open question for us.

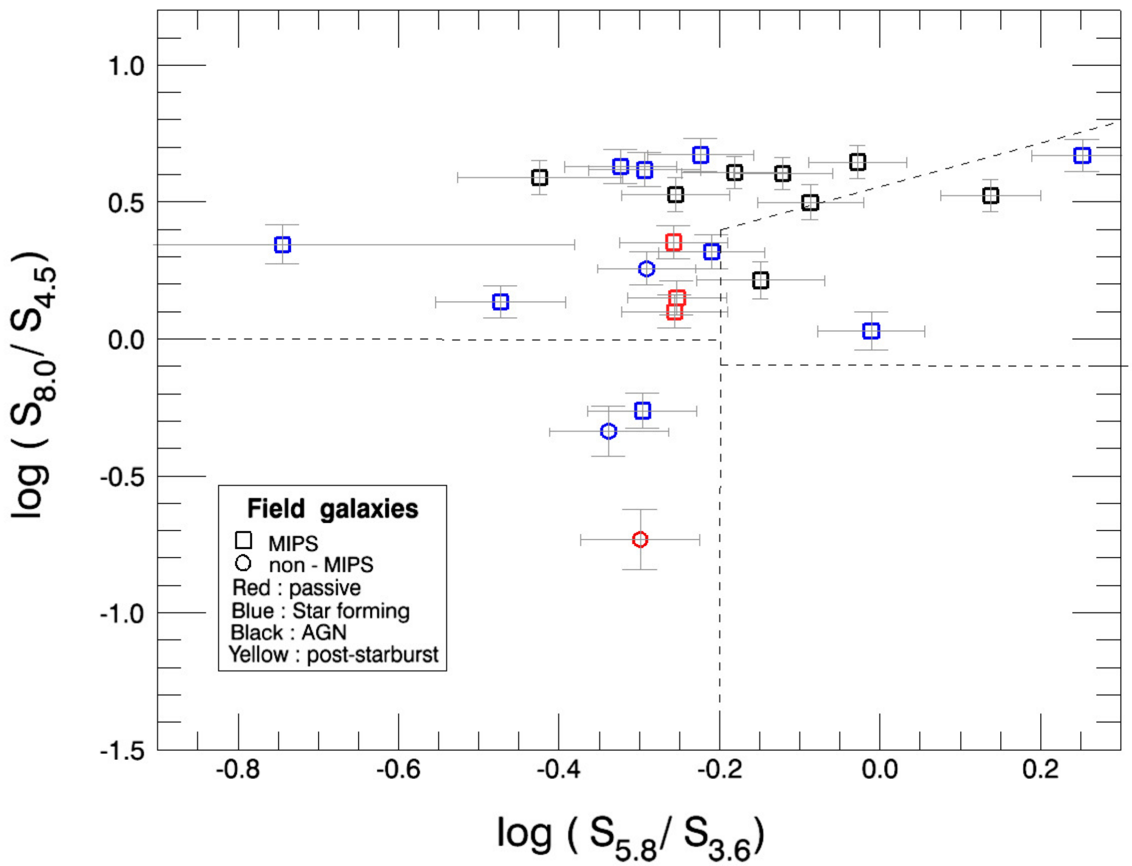

Figure 3.11 Same as figure 3.10 but for field galaxies.

3.5 Conclusion

Comparing the IRAC color-color plots for galaxies in clusters and in the field at $z < 0.5$, we briefly explain our conclusions below (Figure 3.12) :

1 - (Lower-left) : Almost all the 24 μm-faint galaxies lie in lower-left section of Figure 3.12 regardless of their spectral types. The majority of passive galaxies lie and clump in this region. The 24 μm-bright passive galaxies are on a sequence from this clump to upper-left position. Post-starbursts are rare at $z < 0.5$ but all our three detected post-starburst lie in this region. The IRAC color-color plot isolates all passive, 24 μm-faint, and post-starbursts in this region very well.

2 - (Upper-left) : Most of star forming galaxies, along with composites and Seyfert galaxies lie in this section. As we explained in Section 3.4, there is no way to distinguish between pure star forming galaxies and the rest of these galaxies in this section. At lower redshifts star forming galaxies make a sequence from the 24 μm-bright passive galaxies to normal star forming galaxies and then to starbursts and AGNs (Figure 3.12).

3 - (Upper-right) : Although we still observe some star forming galaxies in this section, all identified QSOs lie in this region. These continuum-dominated spectra have higher colors in these plots and make QSOs distinguishable from the rest of the galaxies. This region is ideal for isolating QSOs from the sample.

4 - (Lower-right) : We did not observe any galaxies at $z < 0.5$ in this region.

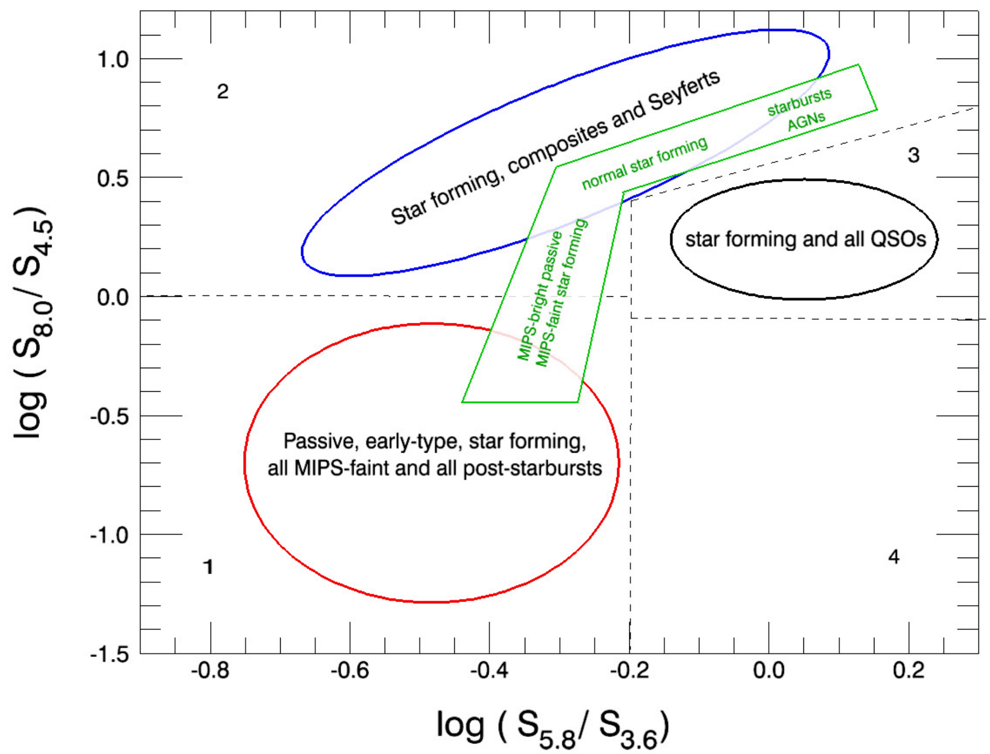

Figure 3.12 The positions of the MORPHS spectral types on IRAC color-color diagram at $z < 0.5$. The green region is the sequence of star forming galaxies at very low redshifts.

Bibliography

Ahn, C.P. et al., 2013, preprint (arXiv:1307.7735)

Dressler, A., Smail, I., Poggianti, B. M., et al. 1999, ApJS, 122, 51

Sajina, A., Lacy, M., Scott, D., 2005, ApJ, 621, 256

Shupe, D. L., Rowan-Robinson, M., Lonsdale, C. J., et al. 2008, AJ, 135, 1050